

Nanoparticles for Biomedical Applications

Nanoparticles have been extensively explored for various biomedical applications, ranging from drug delivery and diagnostic imaging to therapy and regenerative medicine. The diversity in their composition, size, shape, and surface properties allows for their tailored application in different biomedical fields. Here are some of the key types of nanoparticles used in biomedical applications:

Metal Nanoparticles:

Silver nanoparticles, Gold nanoparticles, Iron oxide nanoparticles:.

Quantum Dots:

Lipid-Based Nanoparticles:

Liposomes

Polymeric Nanoparticles:

Dendrimers:

Carbon-Based Nanoparticles:

Carbon nanotubes and graphene:

Nanodiamond

Carbon dot

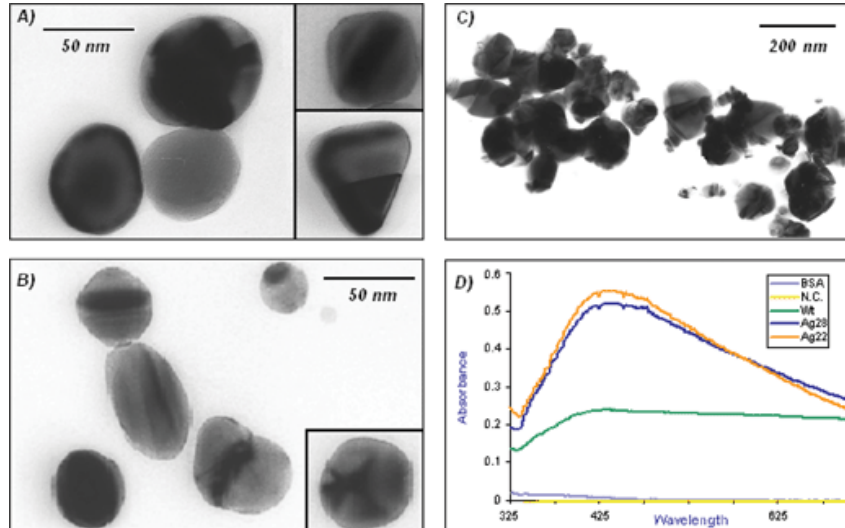
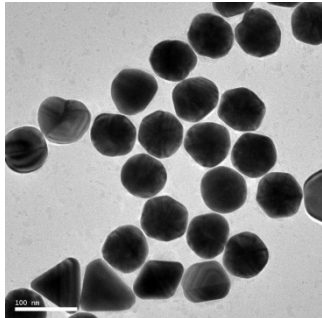
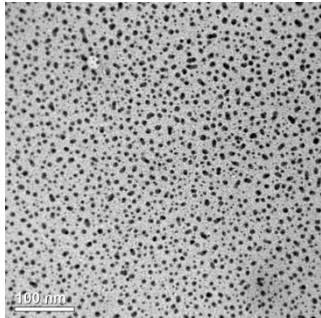
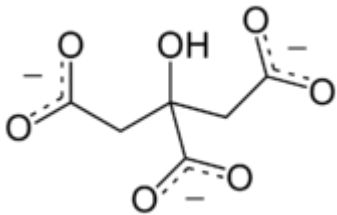
Silica Nanoparticles:

Porous Nanoparticles

Synthesis of Nanoparticles and Surface Modifications

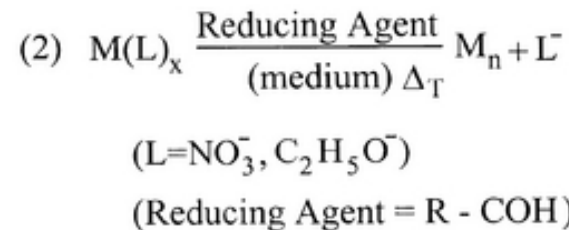
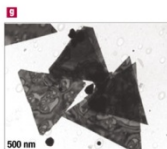
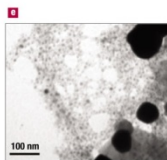
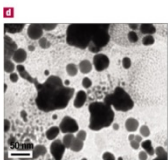
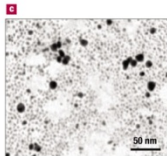
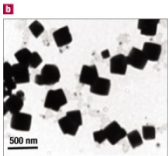
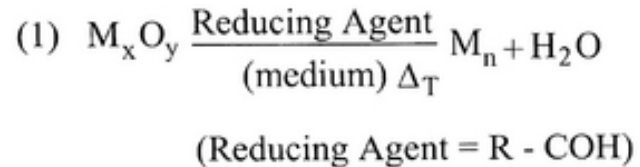
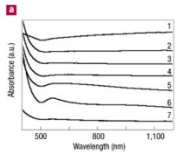
Synthesis of Silver Nanoparticles

1. A solution of AgNO_3 ($1.0 \times 10^{-3} \text{ M}$) in deionized water was heated until it began to boil.
2. **Sodium citrate** solution was added dropwise to the silver nitrate solution as soon as the boiling commenced. The color of the solution slowly turned into grayish yellow, indicating the reduction of the Ag^+ ions.
3. Heating was continued for an additional 15 min, and then the solution was cooled to room temperature before employing for further experimentation.

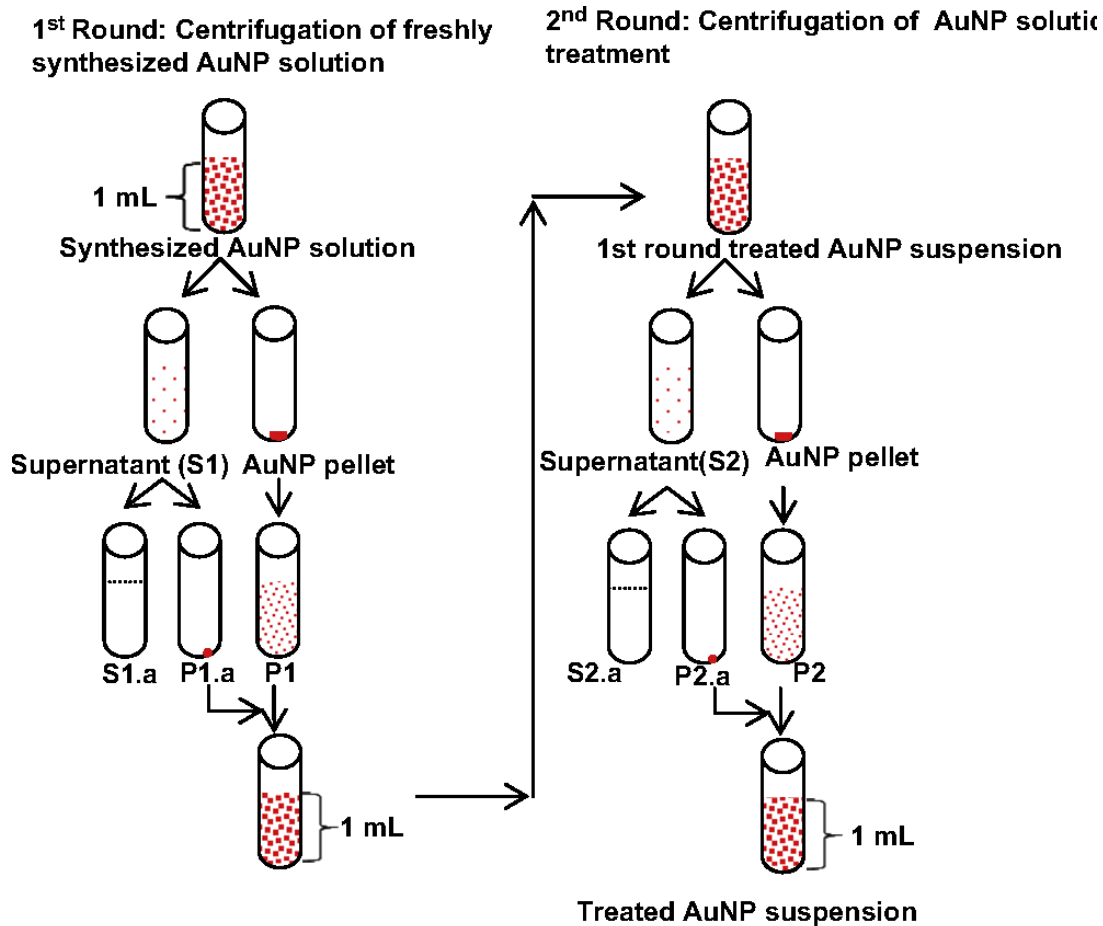


Synthesis of Gold Nanoparticles

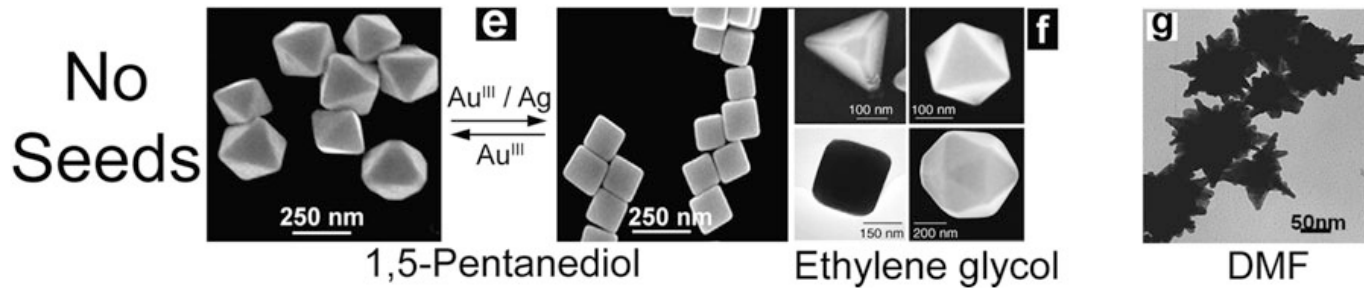
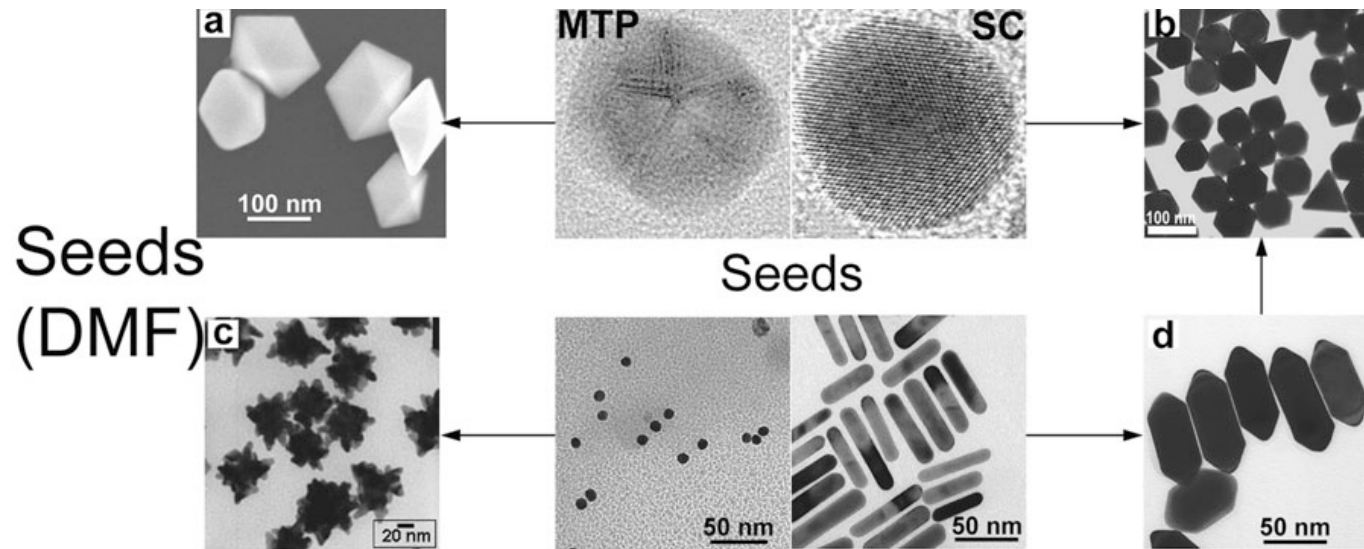
1. Add 20 mL of 1.0 mM **HAuCl₄** to a 50 mL round bottom flask on a stirring hot plate.
2. Add a magnetic stir bar and bring the solution to a boil.
3. To the boiling solution, add 2 mL of a 1% solution of **trisodium citrate dihydrate**
4. The gold sol gradually forms as the citrate reduces the gold(III). Stop heating when a deep red color is obtained.



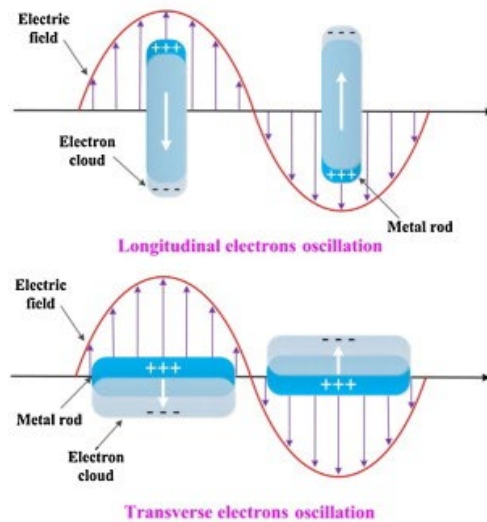
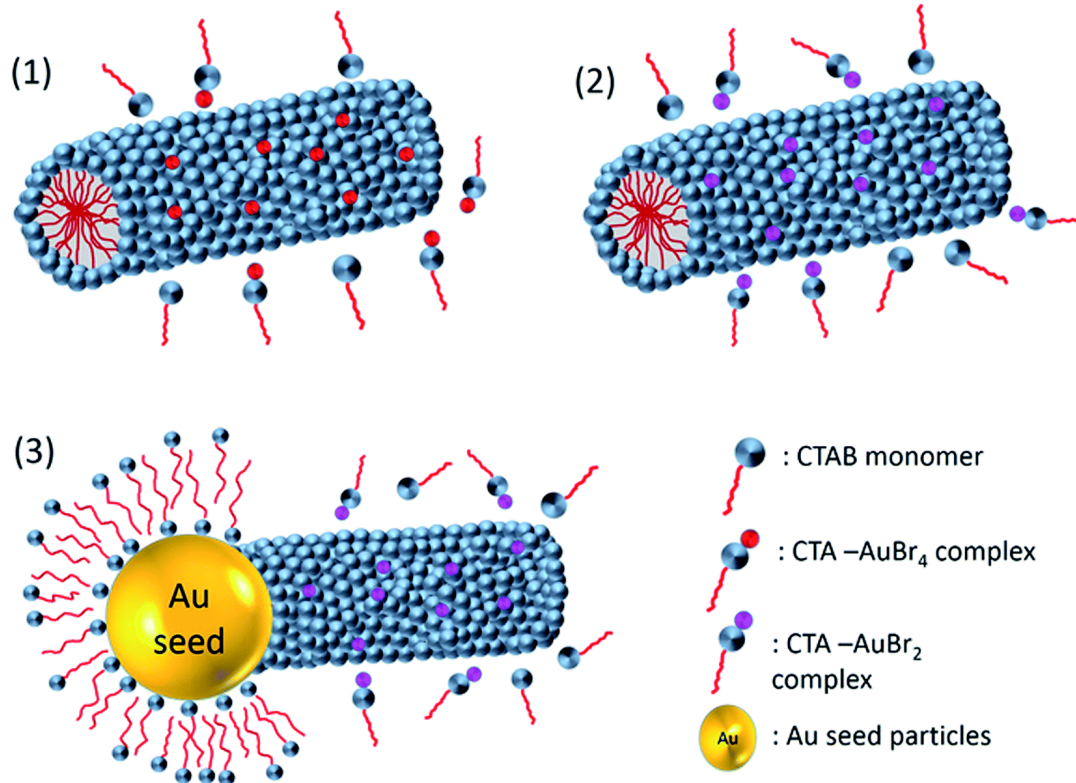
Purification of Au nanoparticles



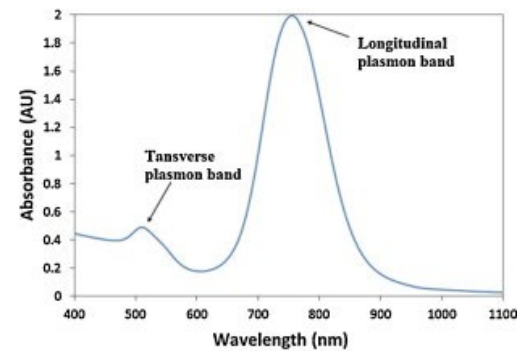
Shape Control



Micrographs of Au nanoparticles with various shapes synthesized through DMF/polyol reduction in the presence of various seeds.

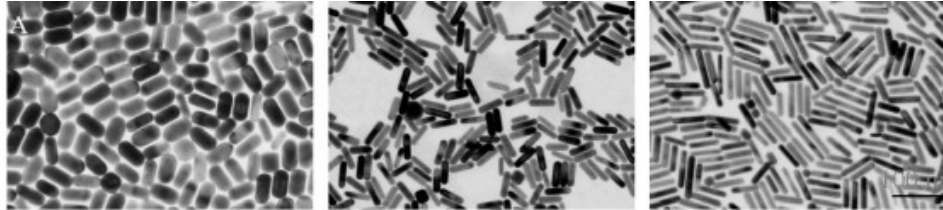


(a)

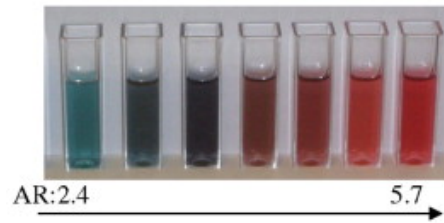


(b)

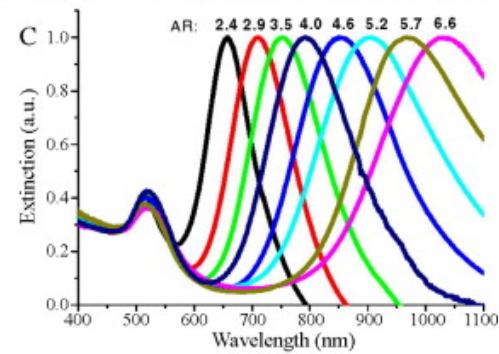
Nanorods



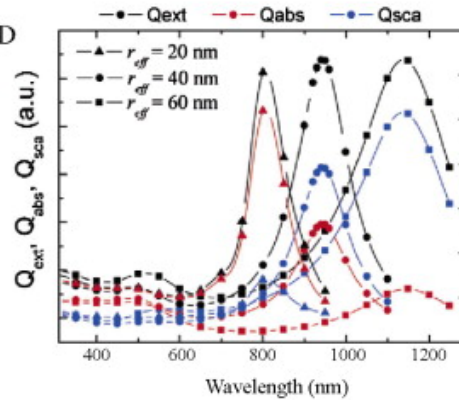
B



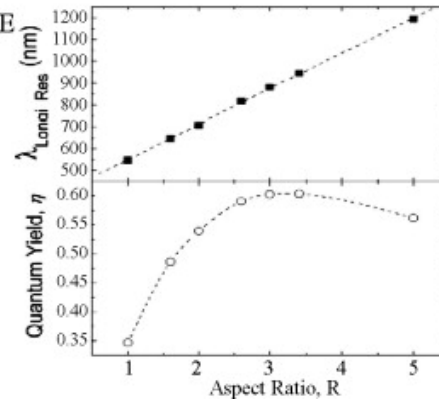
C



D

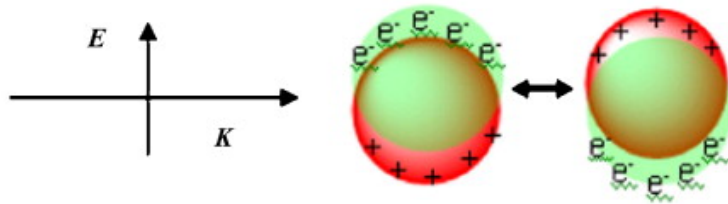


E

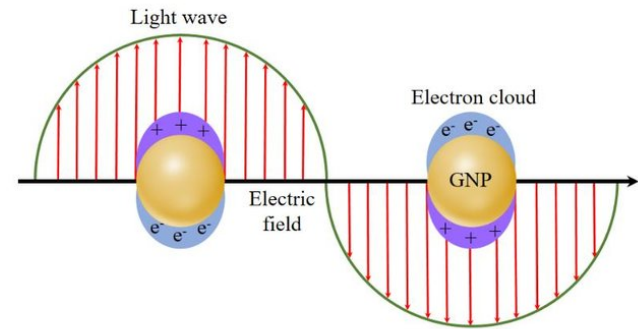
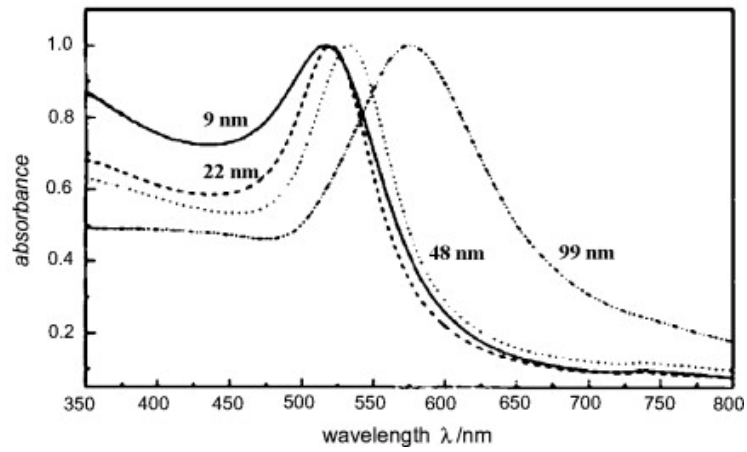


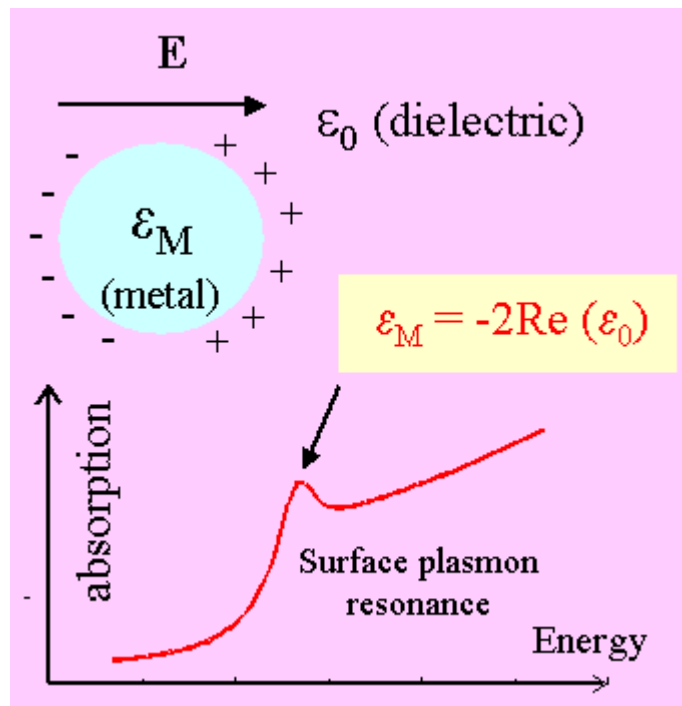
Localized Surface Plasmon

A

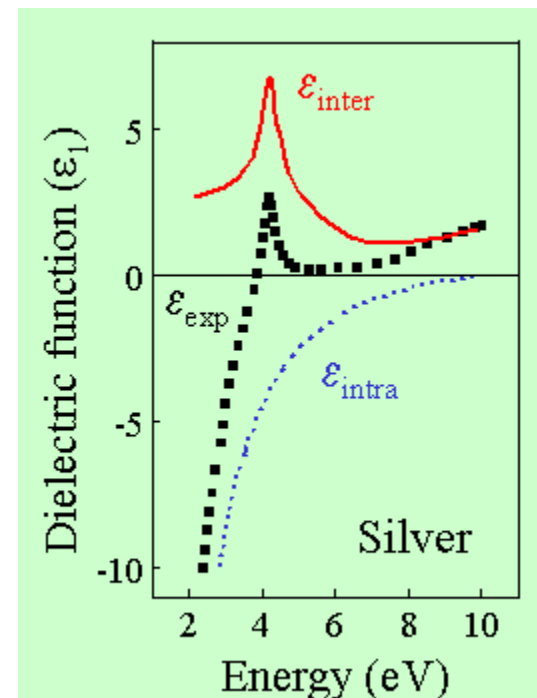


B



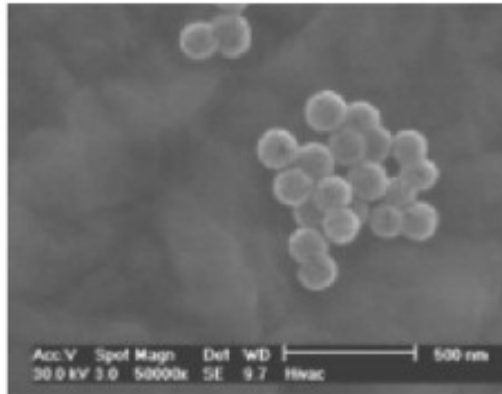


$$\epsilon_{eff} = \epsilon_0 + 3N\epsilon_0 \frac{\epsilon_M - \epsilon_0}{\epsilon_M + 2\epsilon_0}$$

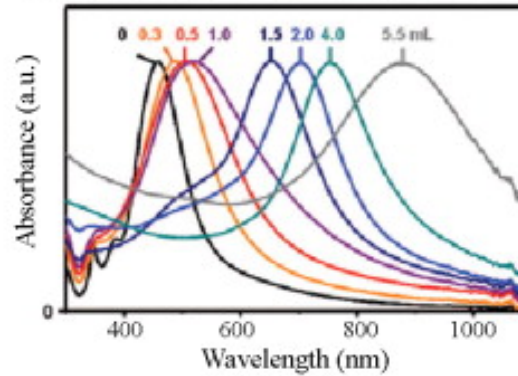
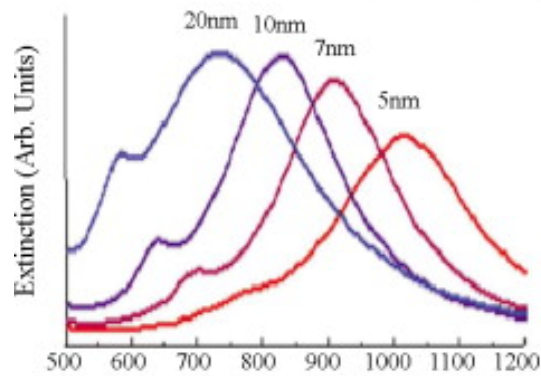
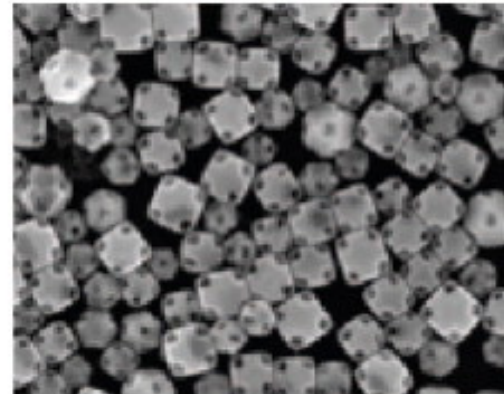


Shape Dependence

A. gold nanoshell



B. gold nanocage



Surface Plasmons and Localized Surface Plasmons

Surface Plasmons (SPs):

Definition: Surface plasmons are coherent delocalized electron oscillations that exist at the interface between a metal and a dielectric material, propagating along the interface. They are excited by electromagnetic waves under specific conditions, facilitating energy transfer across the interface.

Nature: SPs are propagating waves that can travel along the metal-dielectric interface over relatively long distances compared to the wavelength of light, depending on the materials and the interface quality.

Dependency: The existence and properties of SPs depend on the dielectric constants of the metal and the adjacent dielectric material, as well as the geometry of the interface.

Localized Surface Plasmons (LSPs):

Definition: Localized surface plasmons are confined electron oscillations in metallic nanoparticles or nanostructures that occur when the conduction electrons collectively oscillate relative to the fixed positive ions, in response to an external electromagnetic field.

Nature: LSPs are localized around the nanoparticle and do not propagate along an interface. Their resonance frequency depends on the particle's size, shape, and the dielectric environment.

Dependency: The resonance condition for LSPs is determined by the nanoparticle's geometry and the dielectric properties of both the particle and its surrounding medium. Unlike SPs, LSPs can be excited in isolated nanoparticles, not requiring a continuous interface.

Key Differences

Propagation: SPs propagate along the interface between a metal and a dielectric, while LSPs are confined to the vicinity of metallic nanoparticles or nanostructures.

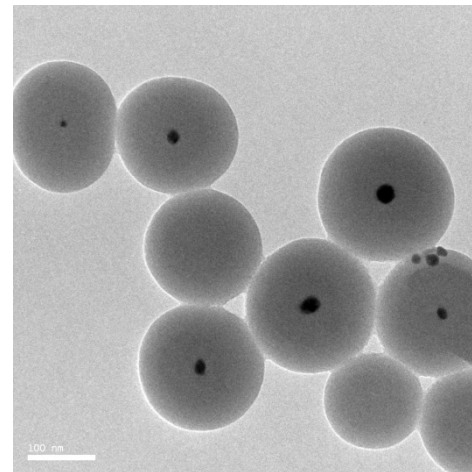
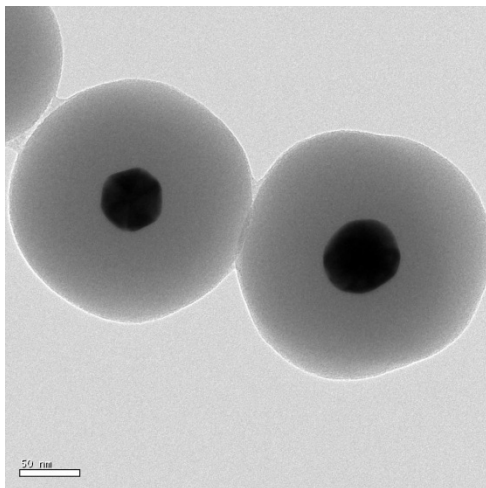
Geometry Dependence: The behavior of SPs is influenced by the interface's properties, whereas LSPs are strongly affected by the size, shape, and material of the nanoparticles, as well as the surrounding dielectric environment.

Localization: SPs are delocalized and can extend over large distances along the interface, whereas LSPs are inherently localized around the nanostructure.

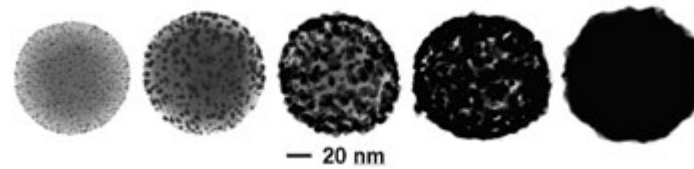
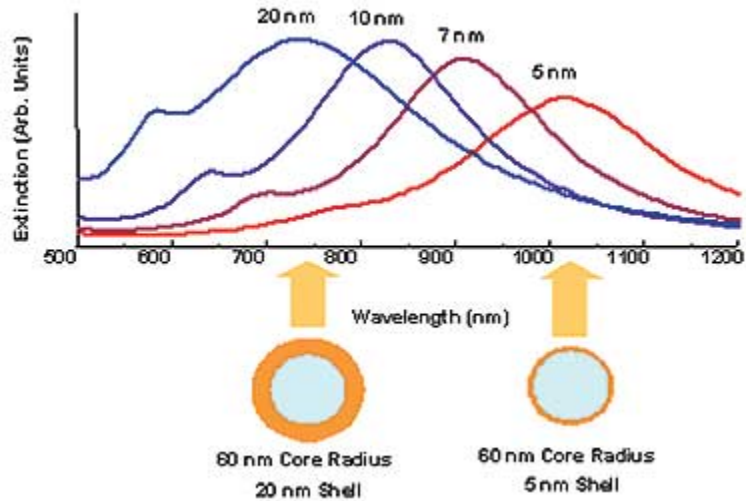
Excitation: LSPs can be excited in individual nanoparticles without the need for a continuous metal-dielectric interface, whereas SPs require a planar or curved interface for their propagation.

Construction of Core Shell Ag/Au@SiO₂ Nanoparticles

1. Under vigorous stirring, 1 ml of the silver/ gold colloids solution was mixed with 250 mL of isopropanol and 25 mL of deionized water.
2. Immediately after the addition of 4 mL of 30% ammonium hydroxide, different amounts of tetraethoxysilane (TEOS) were added to the reaction mixture.
3. To obtain different silica layer thicknesses, TEOS solutions with a concentration between 50% and 100% was added to the suspension. The reaction was stirred at room temperature for 30 minutes and then was allowed to age without agitation at 4 °C overnight.
4. Each suspension of silica-coated silver/gold nanoparticles was washed and centrifuged, followed by re-suspension in water. The thickness of the silica layers was determined from TEM images .



Core-Shell Nanoparticles



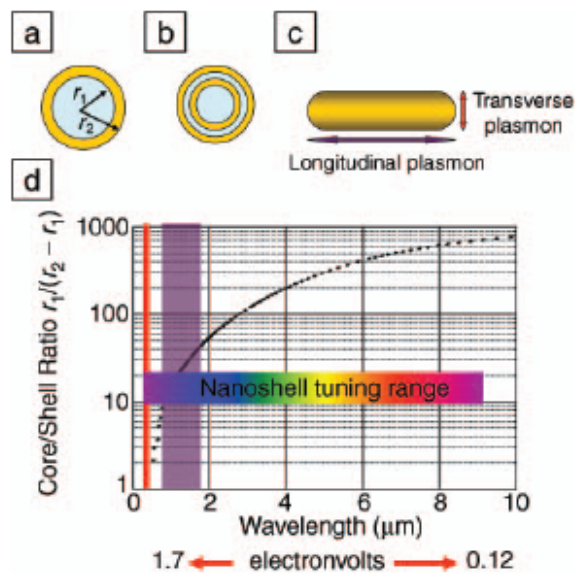


Figure 1. (a) Schematic illustration of a silica-core, gold-shell nanoshell, indicating inner (r_1) and outer (r_2) radii of the shell layers. (b) Depiction of a four-layer, concentric nanoshell. (c) Schematic illustration of a metallic nanorod. (d) Plot of nanoshell resonance as a function of core and shell dimensions, overlaid with reported spectral ranges of nanorod resonances (red, transverse plasmon; purple, longitudinal plasmon), and reported nanoshell and concentric nanoshell combined spectral range of plasmon response.

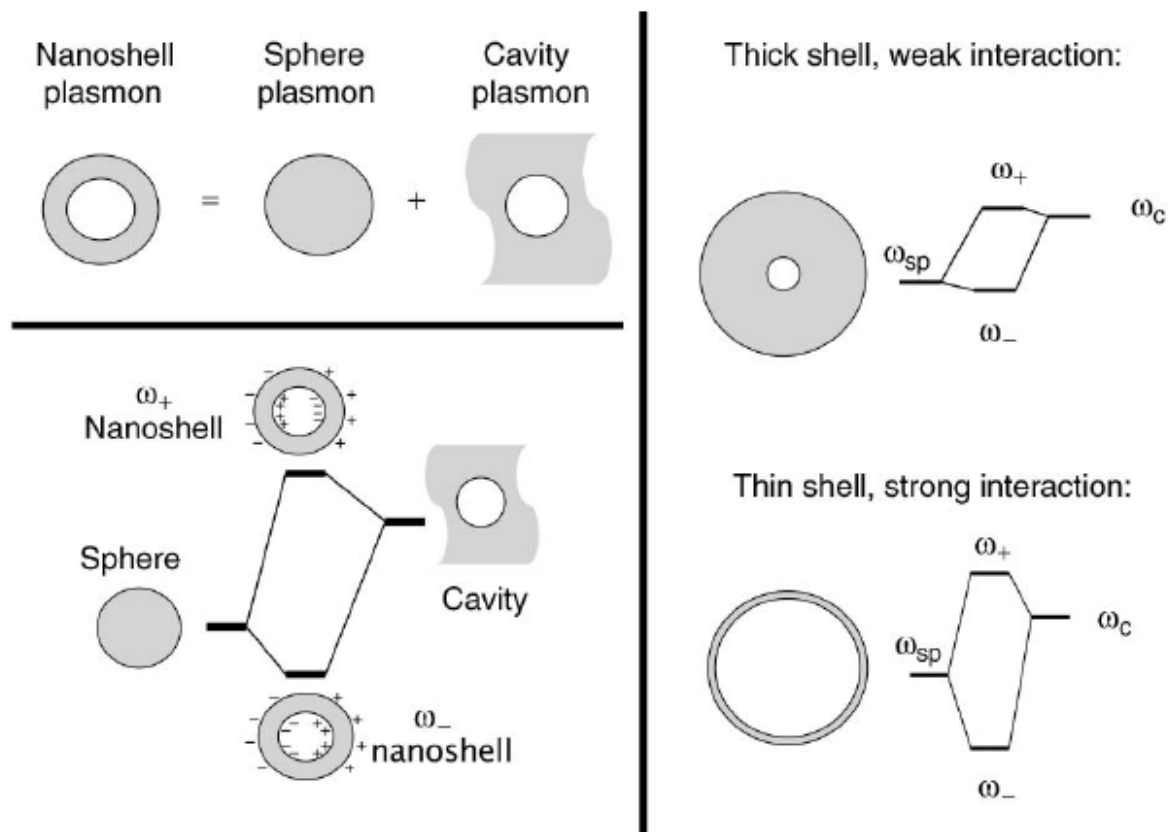


Figure 2. Plasmon hybridization and the sphere-cavity model for nanoshells: the interaction between a sphere (resonance frequency, ω_{sp}) and a cavity plasmon (resonance frequency, ω_c) is tuned by varying the thickness of the shell layer of the nanoparticle. Two hybrid plasmon resonances, the ω_- “bright,” or “bonding,” plasmon and the ω_+ “dark,” or “anti-bonding,” plasmon resonances are formed. The lower-energy plasmon couples most strongly to the optical field.

Preparation of $\text{Fe}_3\text{O}_4@Ag/Au$

1. *To the magnetic nanoparticle suspension obtained from commercial company, add 50 ml of a solution of Au (III) salt or Ag (I) salt at concentration of 0.01–1% mmol/L , shaking for 30 minutes, allowing Au (III) or Ag (I) ion to absorb on the surface of magnetic nanoparticle sufficiently,*
2. *Then adding 15–40 ml of reducing agent, such as hydroxylamine hydrochloride at concentration of 40 mmol/L, reacting for 5–40 minutes.*
3. *Further adding 1–10 ml of a solution of Au (III) salt or Ag (I) salt at concentration of 0.01–1%, shaking for 10 minutes, coating a reduced layer of gold or silver on the surface of the magnetic nanoparticle, forming super-paramagnetic composite particles having core/shell structure, separating magnetically, washing repeatedly with distilled water.*

Quantum Dots

Quantum dots are tiny semiconductor particles only a few nanometers in size, so small that their optical and electronic properties differ from those of larger particles due to quantum mechanics. Here's a breakdown of what makes quantum dots unique and their significant applications:

Definition and Properties

Size: Quantum dots typically range from 2 to 10 nanometers in diameter. At these small sizes, quantum dots contain only a few thousand atoms.

Quantum Confinement: Because of their size, electrons in quantum dots are confined in three spatial dimensions, leading to discrete energy levels. This confinement affects the absorption and emission of light, making quantum dots tunable by changing their size.

Tunability: The color of light emitted by a quantum dot can be adjusted by changing its size. Smaller dots emit shorter wavelengths (blue light), while larger dots emit longer wavelengths (red light).

Brightness and Stability: Quantum dots have high brightness and photostability, outperforming many traditional dyes and fluorescent proteins, which is particularly beneficial in imaging applications.

The Nobel Prize in Chemistry 2023

The Royal Swedish Academy of Sciences has decided to award the Nobel Prize in Chemistry 2023 to

Moungi G. Bawendi

Massachusetts Institute of Technology (MIT),
Cambridge, MA, USA

Louis E. Brus

Columbia University, New York, NY, USA

Aleksey Yekimov

Nanocrystals Technology Inc., New York,
NY, USA

“for the discovery and synthesis of quantum dots”

They planted an important seed for nanotechnology

The Nobel Prize in Chemistry 2023 rewards the discovery and development of *quantum dots*, nanoparticles so tiny that their size determines their properties. These smallest components of nanotechnology now spread their light from televisions and LED lamps, and can also guide surgeons when they remove tumour tissue, among many other things.

Everyone who studies chemistry learns that an element’s properties are governed by how many electrons it has. However, when matter shrinks to nano-dimensions quantum phenomena arise; these are governed by the size of the matter. The Nobel Laureates in Chemistry 2023 have succeeded in producing particles so small that their properties are determined by quantum phenomena. The particles, which are called quantum dots, are now of great importance in nanotechnology.

“Quantum dots have many fascinating and unusual properties. Importantly, they have different colours depending on their size,” says Johan Åqvist, Chair of the Nobel Committee for Chemistry.

Physicists had long known that in theory size-dependent quantum effects could arise in nanoparticles, but at that time it was almost impossible to sculpt in nano-dimensions. Therefore, few people believed that this knowledge would be put to practical use.

However, in the early 1980s, **Aleksey Yekimov** succeeded in creating size-dependent quantum effects in coloured glass. The colour came from nanoparticles of copper chloride and Yekimov demonstrated that the particle size affected the colour of the glass via quantum effects.

A few years later, **Louis Brus** was the first scientist in the world to prove size-dependent quantum effects in particles floating freely in a fluid.

In 1993, **Moungi Bawendi** revolutionised the chemical production of quantum dots, resulting in almost perfect particles. This high quality was necessary for them to be utilised in applications.

Quantum dots now illuminate computer monitors and television screens based on QLED technology. They also add nuance to the light of some LED lamps, and biochemists and doctors use them to map biological tissue.

Quantum dots are thus bringing the greatest benefit to humankind. Researchers believe that in the future they could contribute to flexible electronics, tiny sensors, thinner solar cells and encrypted quantum communication – so we have just started exploring the potential of these tiny particles.

Moungi G. Bawendi, born 1961 in Paris, France. PhD 1988 from University of Chicago, IL, USA. Professor at Massachusetts Institute of Technology (MIT), Cambridge, MA, USA.

Louis E. Brus, born 1943 in Cleveland, OH, USA. PhD 1969 from Columbia University, New York, NY, USA. Professor at Columbia University, New York, NY, USA.

Aleksey Yekimov, born 1945 in the former USSR. PhD 1974 from Ioffe Physical-Technical Institute, Saint Petersburg, Russia. Formerly Chief Scientist at Nanocrystals Technology Inc., New York, NY, USA.

Synthesis of Quantum Dots

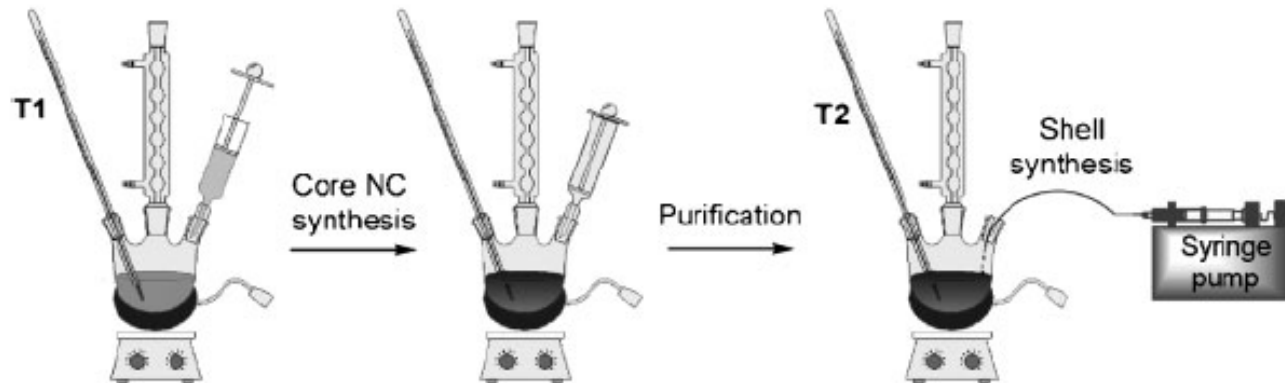
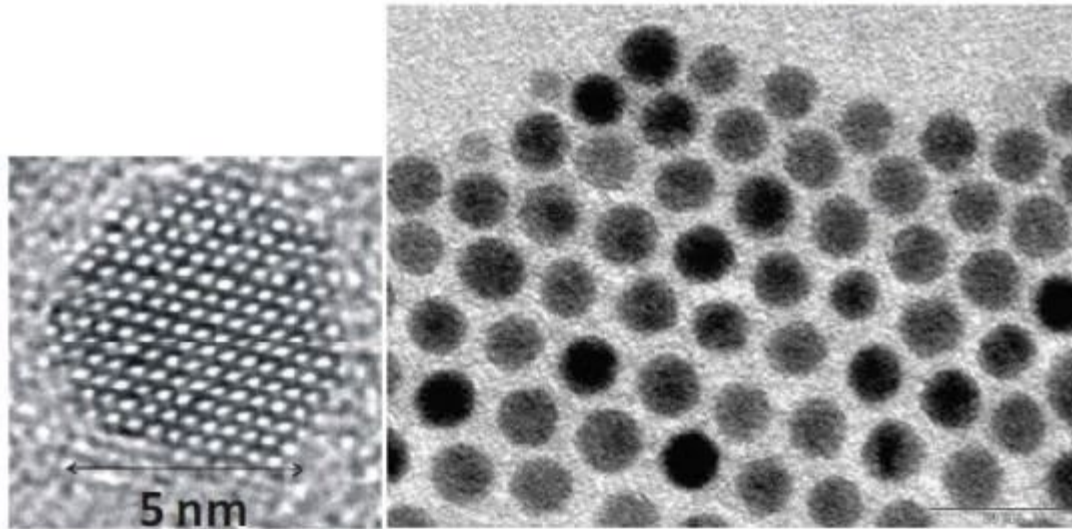


Figure 2. Two-step synthesis of core/shell nanocrystals.

Quantum Dots



Type I Quantum Dots:

Band Alignment: In Type I quantum dots, both the conduction band minimum and the valence band maximum of the shell material lie outside the energy levels of the core material. This means that both electrons and holes are confined within the core material.

Carrier Confinement: Since both charge carriers (electrons and holes) are confined in the same region (the core), they have a higher probability of recombining. This results in strong photoluminescence as the recombination of electrons and holes releases energy in the form of light.

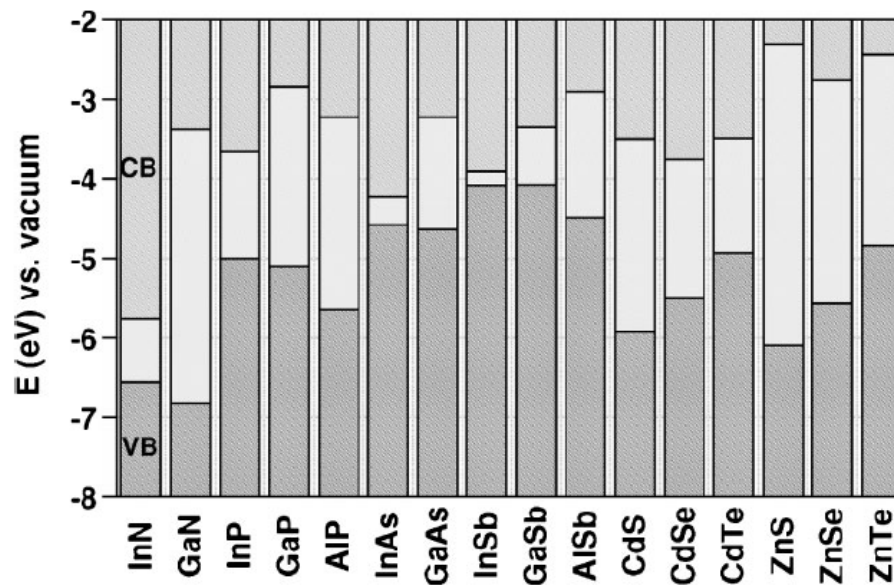
Applications: Due to their efficient confinement of charge carriers and strong luminescence, Type I quantum dots are widely used in applications that require high fluorescence efficiency, such as in bioimaging, light-emitting diodes (LEDs), and quantum dot displays.

Type II Quantum Dots:

Band Alignment: In Type II quantum dots, the conduction band minimum and the valence band maximum are staggered between the core and shell materials. This typically results in the confinement of electrons and holes in different regions; for example, electrons may be confined in the core while holes are localized in the shell, or vice versa.

Carrier Confinement: The spatial separation of charge carriers (electron and hole) reduces their recombination probability, which can lead to longer exciton lifetimes. While this separation can decrease the photoluminescence efficiency, it provides other useful properties, such as tunable emission from the visible to the infrared spectrum.

Applications: The extended carrier lifetimes and tunable emission properties make Type II quantum dots useful for applications in solar energy conversion, where they can help in creating more efficient photovoltaic cells, and in sensors, where their tunable absorption can be exploited for detecting various substances.



Scheme 1. Electronic energy levels of selected III-V and II-VI semiconductors using the valence-band offsets from Reference [12] (VB: valence band, CB: conduction band).

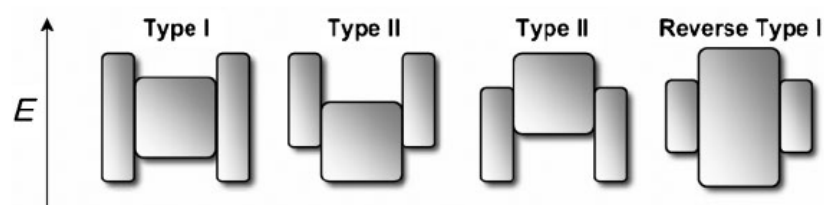
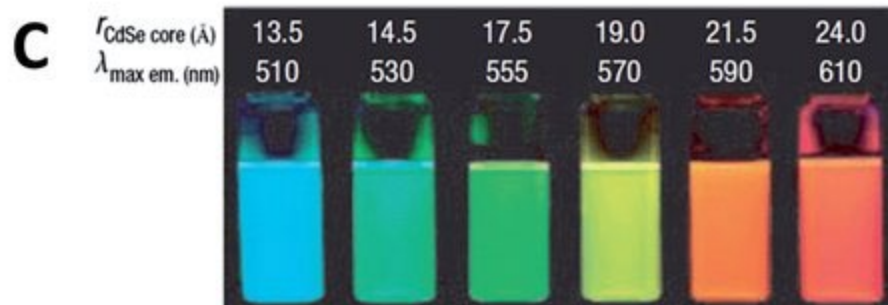
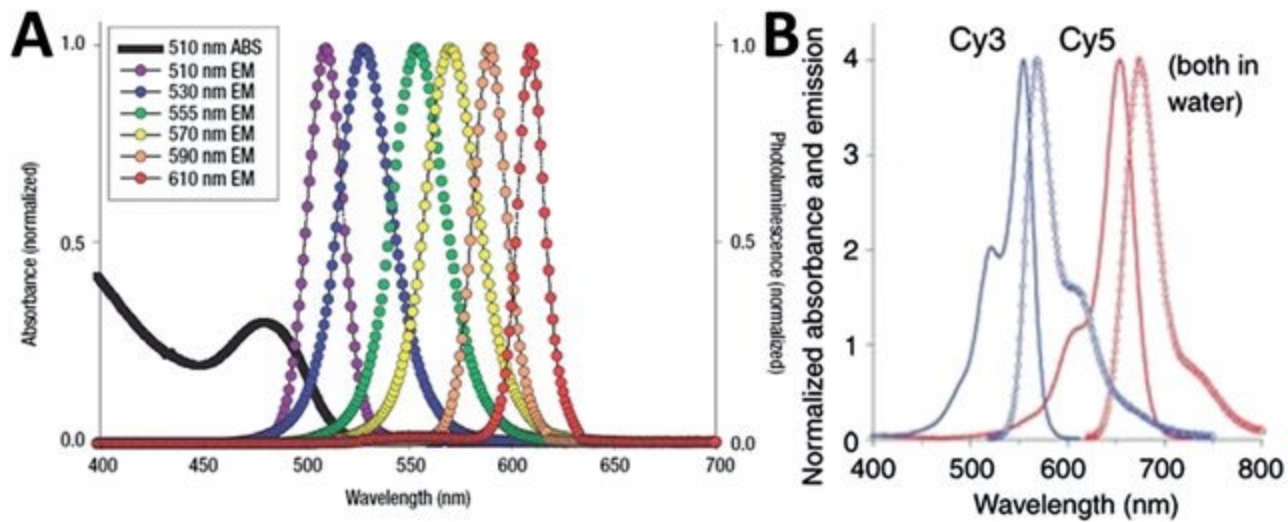


Figure 1. Schematic representation of the energy-level alignment in different core/shell systems realized with semiconductor NCs to date. The upper and lower edges of the rectangles correspond to the positions of the conduction- and valence-band edge of the core (center) and shell materials, respectively.

Optical Properties



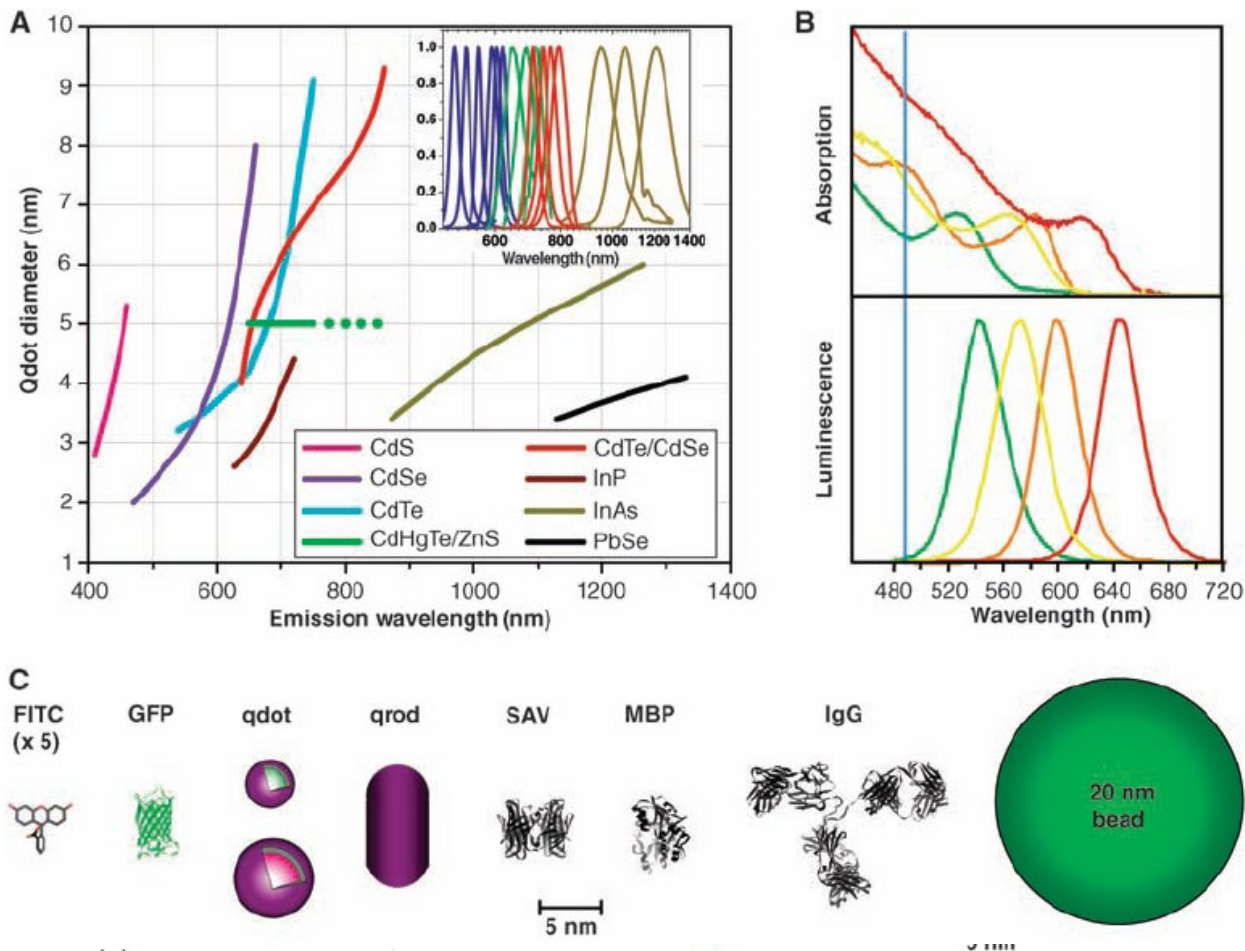


Fig. 1. (A) Emission maxima and sizes of quantum dots of different composition. Quantum dots can be synthesized from various types of semiconductor materials (II-VI: CdS, CdSe, CdTe...; III-V: InP, InAs...; IV-VI: PbSe...) characterized by different bulk band gap energies. The curves represent experimental data from the literature on the dependence of peak emission wavelength on qdot diameter. The range of emission wavelength is 400 to 1350 nm, with size varying from 2 to 9.5 nm (organic passivation/solubilization layer not included). All spectra are typically around 30 to 50 nm (full width at half maximum). Inset: Representative emission spectra for some materials. Data are from (12, 18, 27, 76–82). Data for CdHgTe/ZnS have been extrapolated to the maximum emission wavelength obtained in our group. (B) Absorption (upper curves) and emission (lower curves) spectra of four CdSe/ZnS qdot samples. The blue vertical line indicates the 488-nm line of an argon-ion laser, which can be used to efficiently excite all four types of qdots simultaneously. [Adapted from (28)] (C) Size comparison of qdots and comparable objects. FITC, fluorescein isothiocyanate; GFP, green fluorescent protein; qdot, green (4 nm, top) and red (6.5 nm, bottom) CdSe/ZnS qdot; qrod, rod-shaped qdot (size from Quantum Dot Corp.'s Web site). Three proteins—streptavidin (SAV), maltose binding protein (MBP), and immunoglobulin G (IgG)—have been used for further functionalization of qdots (see text) and add to the final size of the qdot, in conjunction with the solubilization chemistry (Fig. 2).

Advantages of QDs for Imaging

Broad Excitation and Narrow Emission Spectra: Quantum dots can be excited by a wide range of wavelengths but emit light at very specific wavelengths. This narrow emission spectrum allows for the simultaneous use of multiple quantum dot colors for multiplexed imaging, enabling the visualization of several targets within a single sample.

Size- and Composition-Tunable Fluorescence: The emission wavelength of quantum dots can be precisely tuned by changing their size or composition, allowing for the generation of a wide palette of colors from the same material simply by adjusting the quantum dot size. This tunability is advantageous for creating highly multiplexed imaging assays.

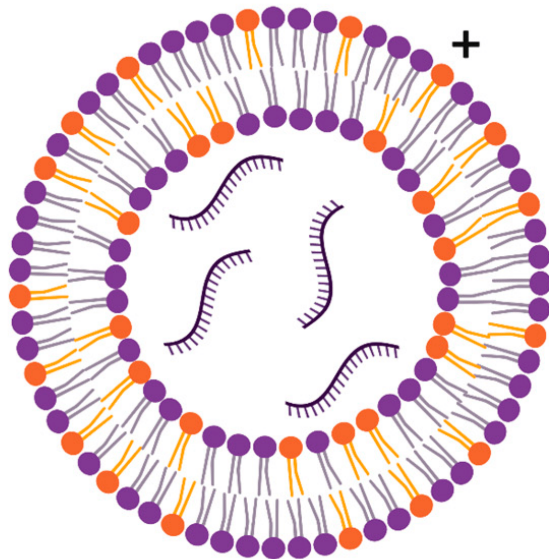
High Photostability: Quantum dots are much more resistant to photobleaching than traditional fluorescent dyes and proteins. This property allows for prolonged imaging sessions and repeated exposures, which are essential for long-term studies of dynamic processes in live cells or tissues.




High Quantum Yield: Quantum dots generally have high quantum yields, meaning they are very efficient at converting absorbed light into emitted light. This results in bright signals that can improve the sensitivity and detection limits of bioimaging applications.

Versatility in Functionalization and Bioconjugation: Quantum dots can be functionalized with various biological molecules, such as antibodies, peptides, or nucleic acids, enabling targeted imaging of specific molecules or structures within cells and tissues. This specificity is crucial for studying complex biological processes and for diagnostic purposes.

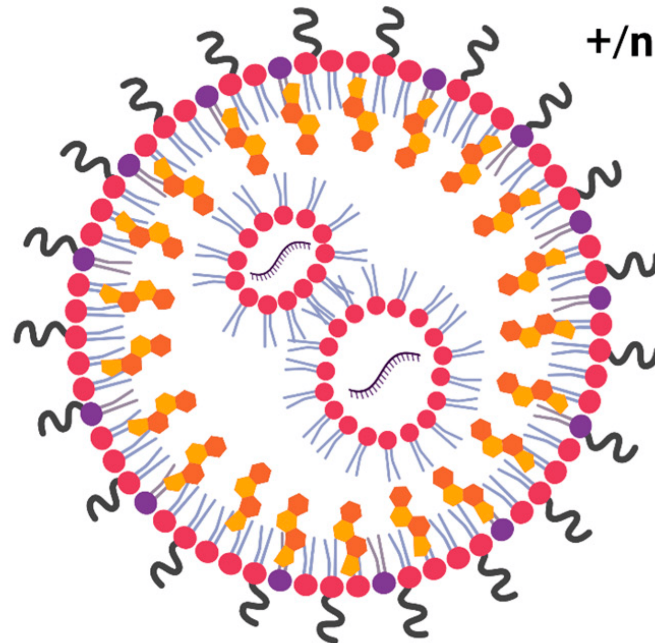
Lipid Nanoparticles






a.



-  cationic lipid
-  helper lipid
-  RNA

b.



-  ionizable cationic lipid
-  helper lipid
-  cholesterol
-  PEG
-  RNA

Selection of Lipid Materials: The first step involves selecting appropriate lipid materials. The typical components of LNPs for vaccine delivery include:

Ionizable cationic lipids: Facilitate endosomal escape of the RNA into the cytoplasm.

Phospholipids: Provide structural integrity.

Cholesterol: Stabilizes the lipid bilayer.

Polyethylene glycol (PEG)-lipids: Confer stealth properties to avoid rapid clearance from the body.

Nucleic Acid Encapsulation: The mRNA or other nucleic acid is mixed with the lipid components. The encapsulation is usually achieved through one of the following processes:

Ethanol Dilution Method: Lipids dissolved in ethanol are rapidly mixed with an aqueous solution containing the nucleic acid. This process results in the spontaneous assembly of LNPs encapsulating the mRNA.

Microfluidics: This method involves the controlled mixing of lipid and nucleic acid streams under laminar flow conditions in a microfluidic device. Microfluidics allows for precise control over the nanoparticle size and encapsulation efficiency.

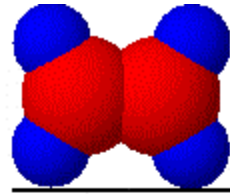
LNP Formation and Size Adjustment: The size of LNPs is crucial for their effectiveness and is typically adjusted to be around 80-100 nanometers.

Sterilization and Quality Control: The LNPs must be sterile for use in vaccines. Sterilization can be achieved by filtration through a sterile filter with a suitable pore size (e.g., 0.22 micrometers).

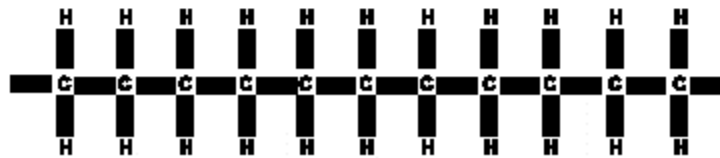
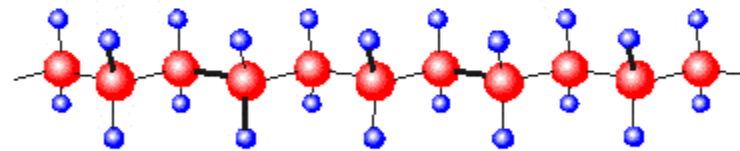
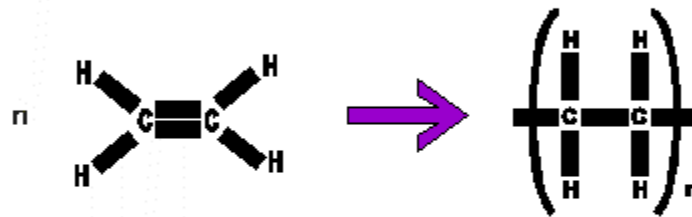
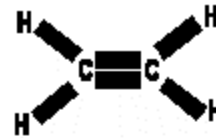
Formulation: The final LNP formulation is typically prepared in a buffer suitable for injection. The formulation process must ensure that the LNPs are stable and maintain their integrity until they are administered.

Storage: The stability of LNPs is temperature-dependent. They are usually stored at low temperatures (e.g., -80°C) to maintain their structural integrity and functional properties until they are ready to be used.

Polymer



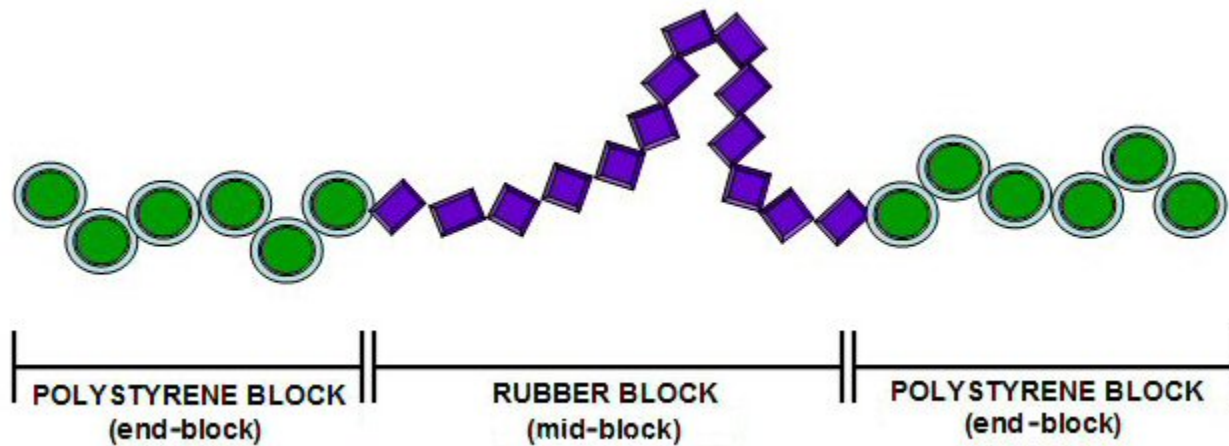
a monomer ethene



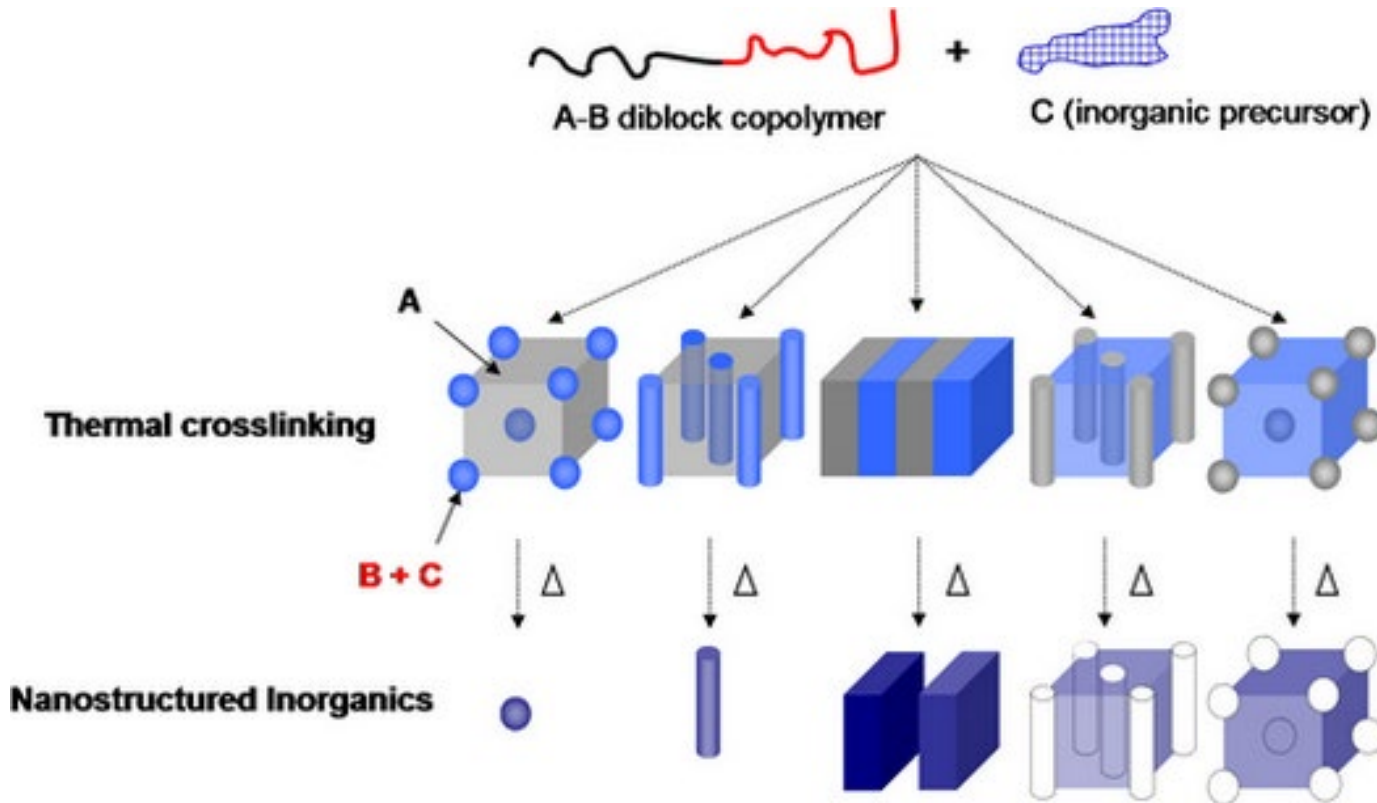
a polymer

poly(ethene)

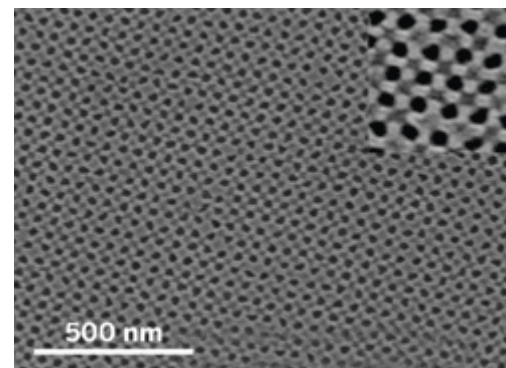
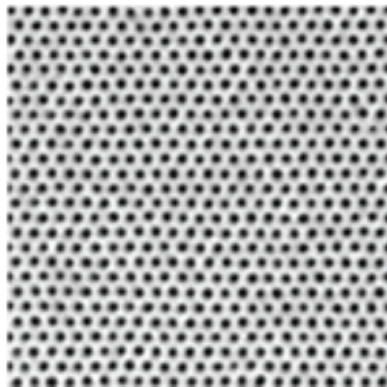
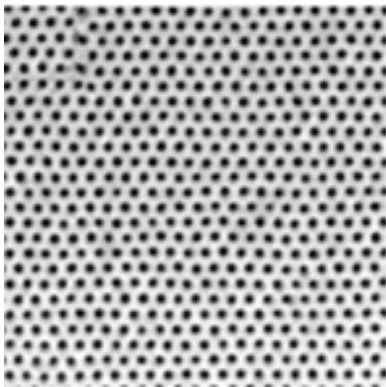
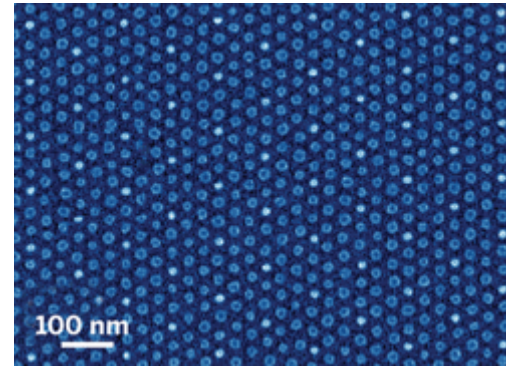
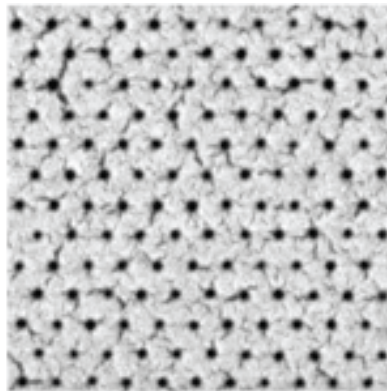
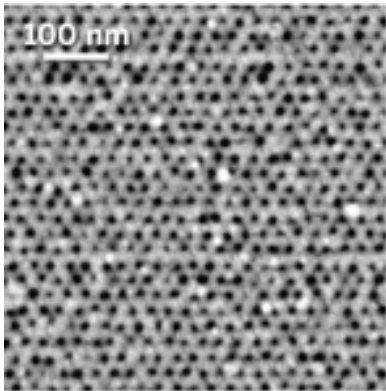
Block copolymer



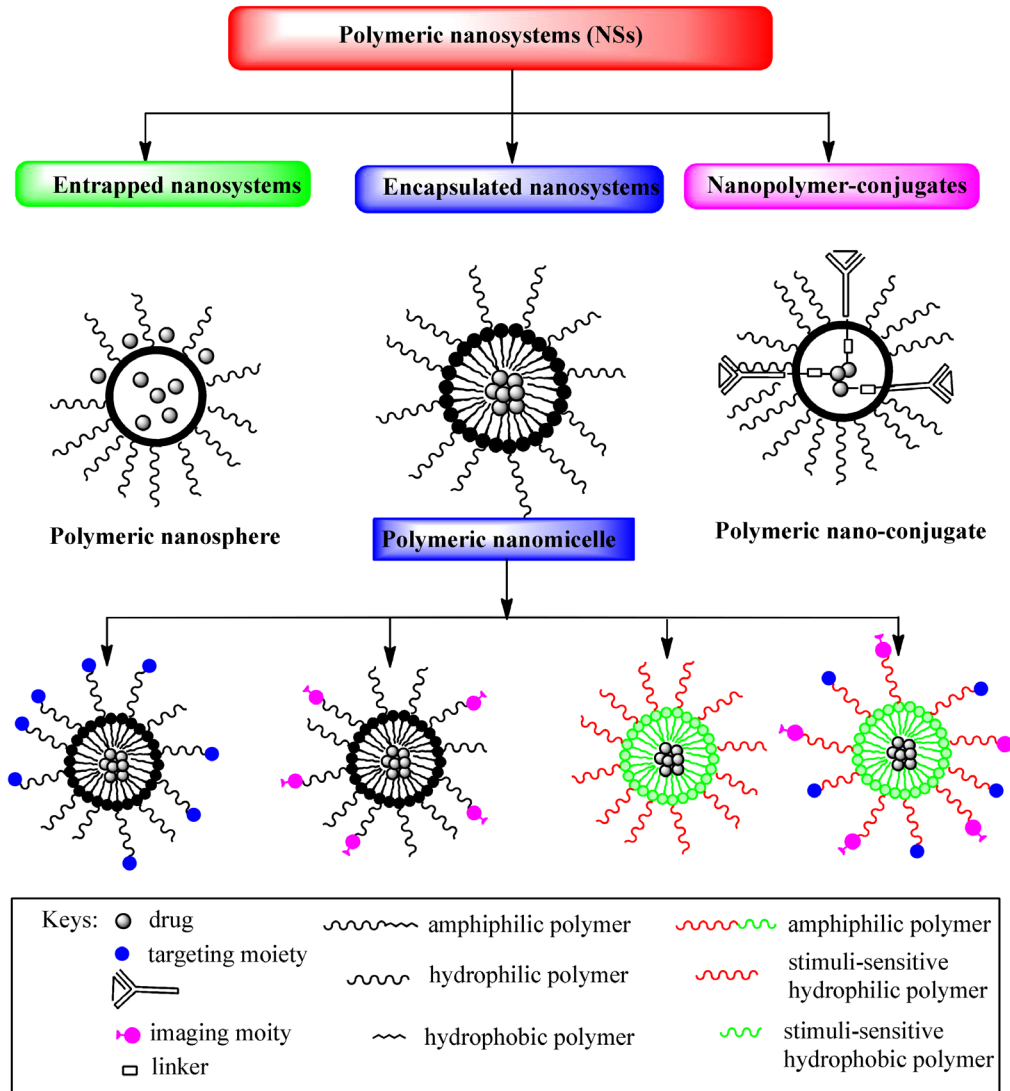
Phase Segregation



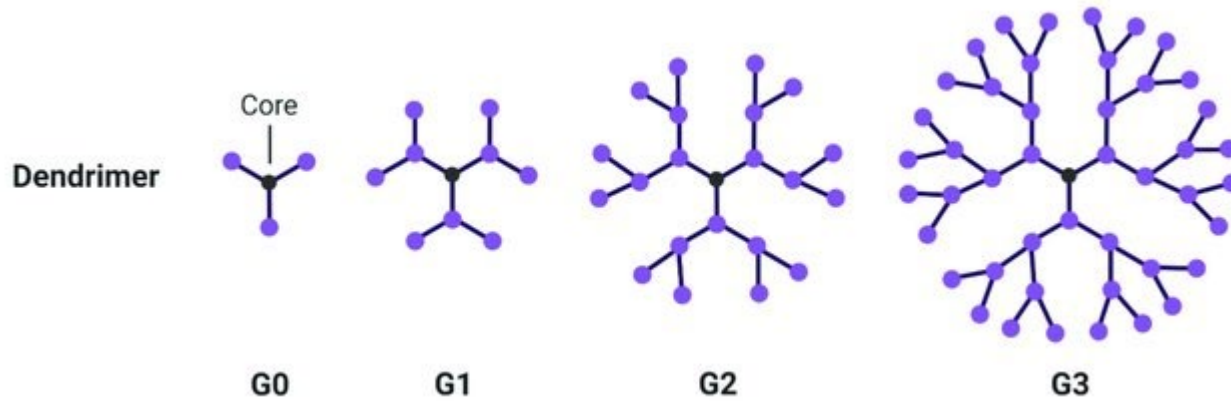
Self-Assembled Block-copolymer



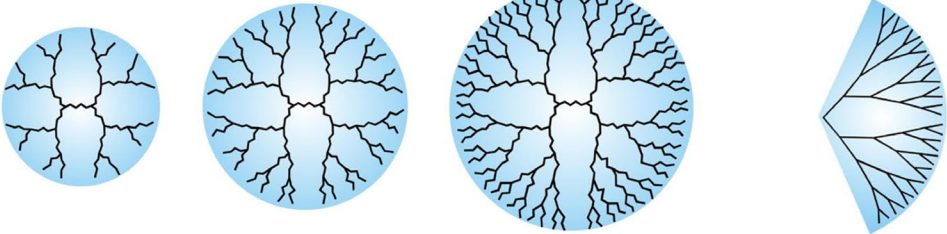
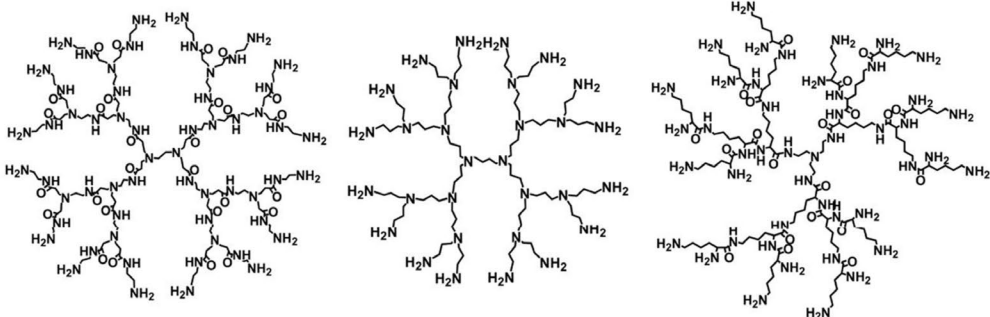
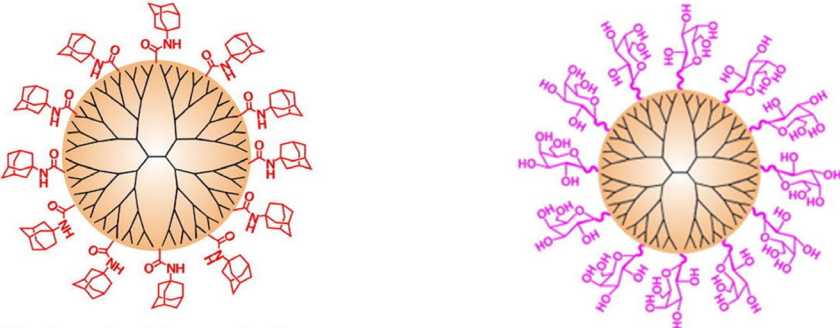
Polymer Nanoparticles



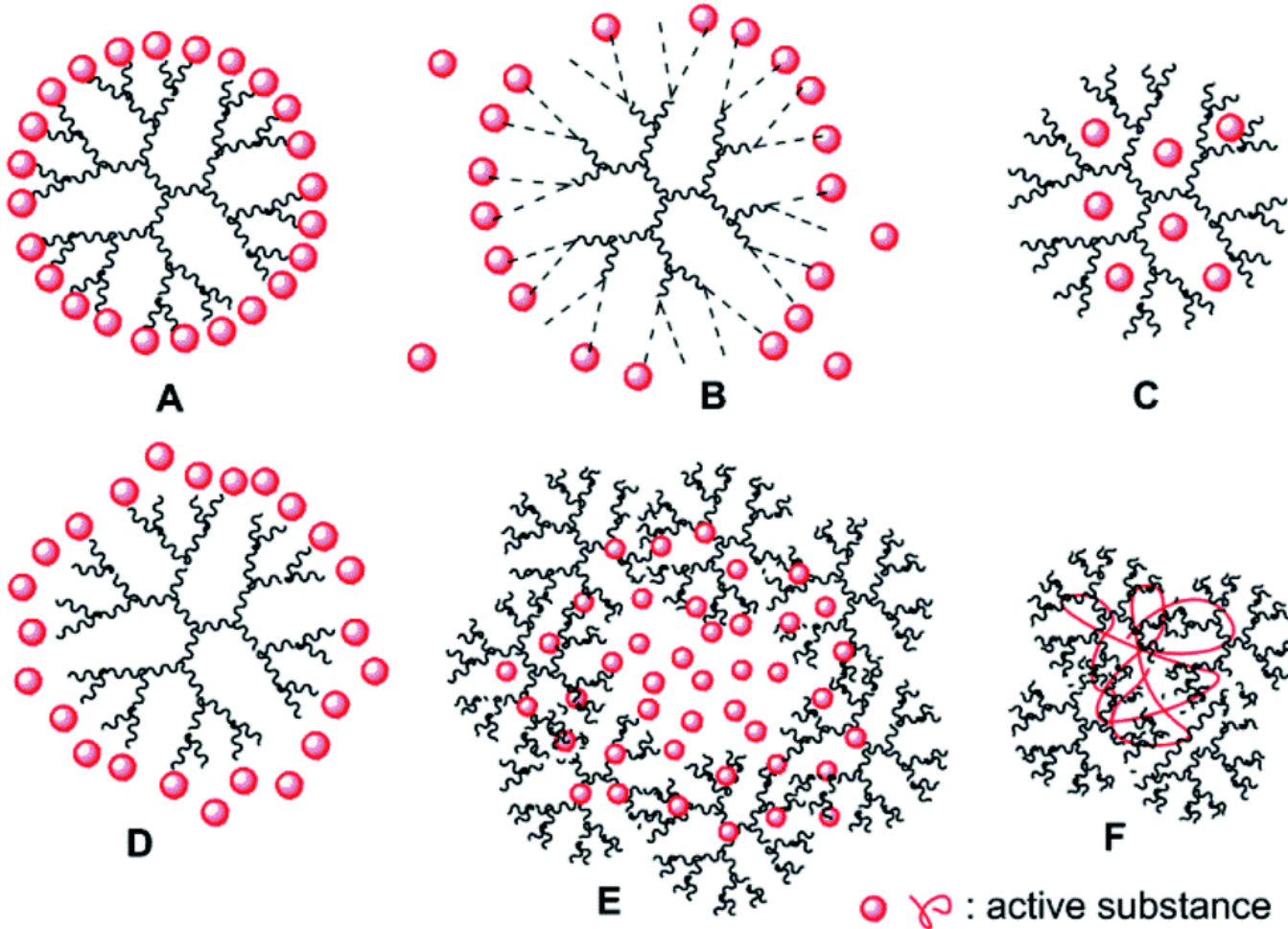
Dendrimer



Dendrimer

<p>Dendrimer generation</p>	 <p>G3 G4 G5 Dendron G5</p>
<p>Nature of the branches</p>	 <p>PAMAM PPI PLL</p>
<p>End-group functionalities</p>	 <p>Hydrophobic moieties Biological moieties</p>

Dendrimer



Carbon Nanomaterials

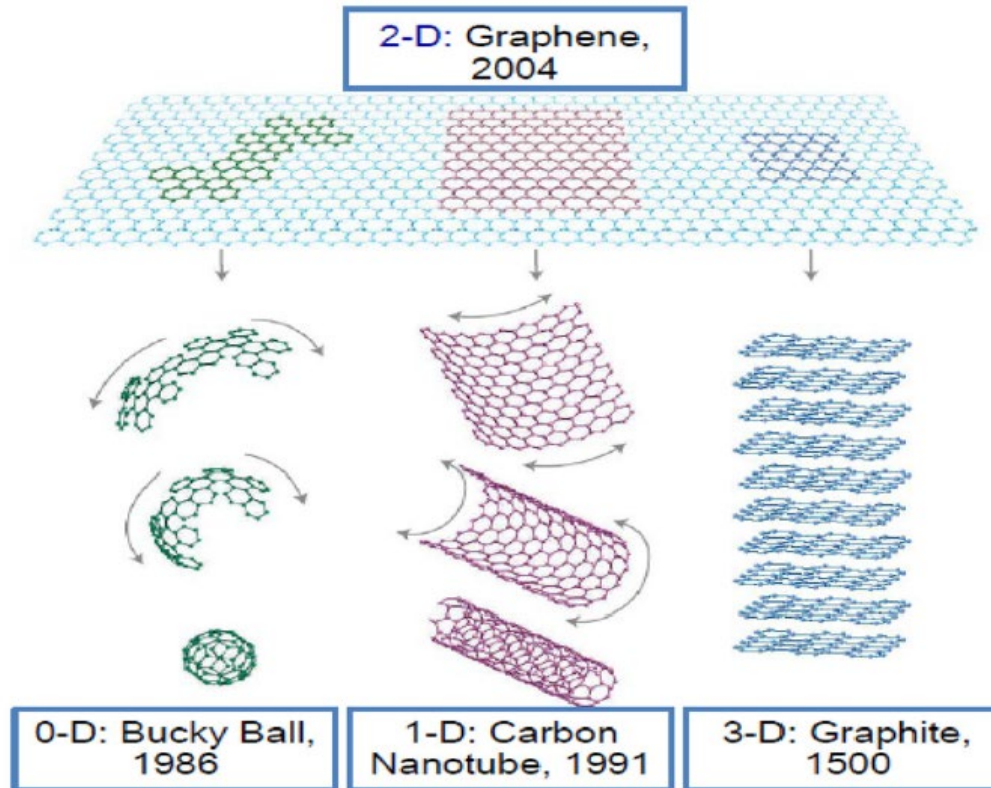


Fig. 1 Mother of all graphene forms. Graphene is a 2D building material for carbon material of all other dimensionalities. It can be wrapped up into 0D buckyballs, rolled into 1D nanotubes or stacked into 3D graphite [23]

CNT

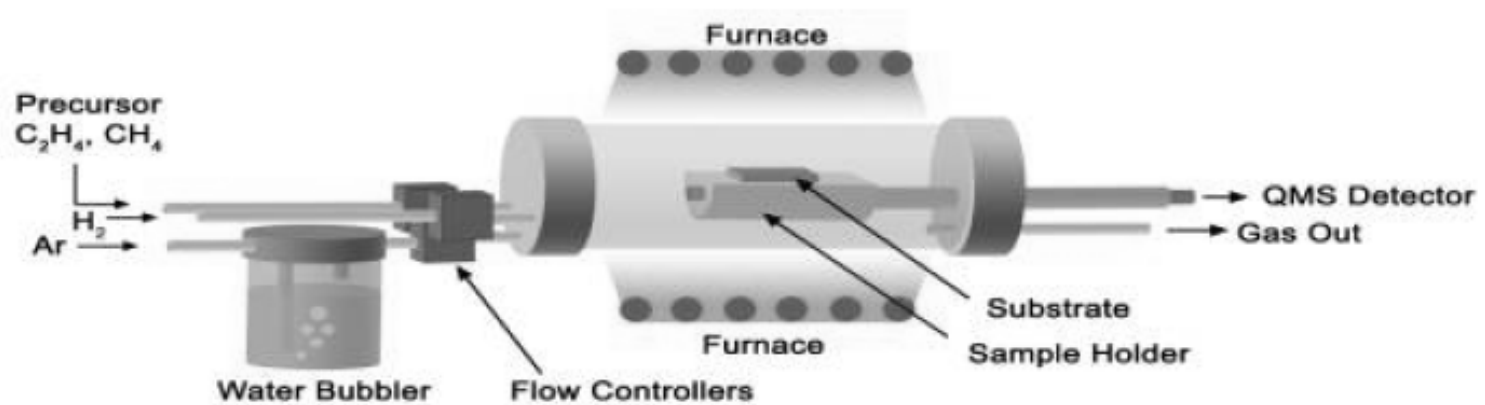
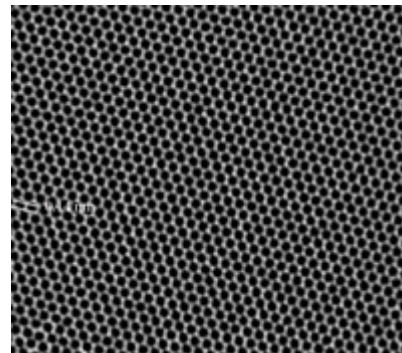
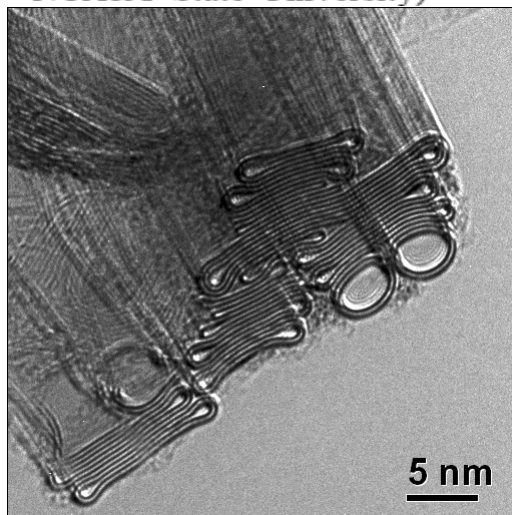


Fig. 1. Schematic of a CVD reactor for carbon nanotube growth. (Sketch by S. Yarmolenko from NCA&T State University)



Graphene

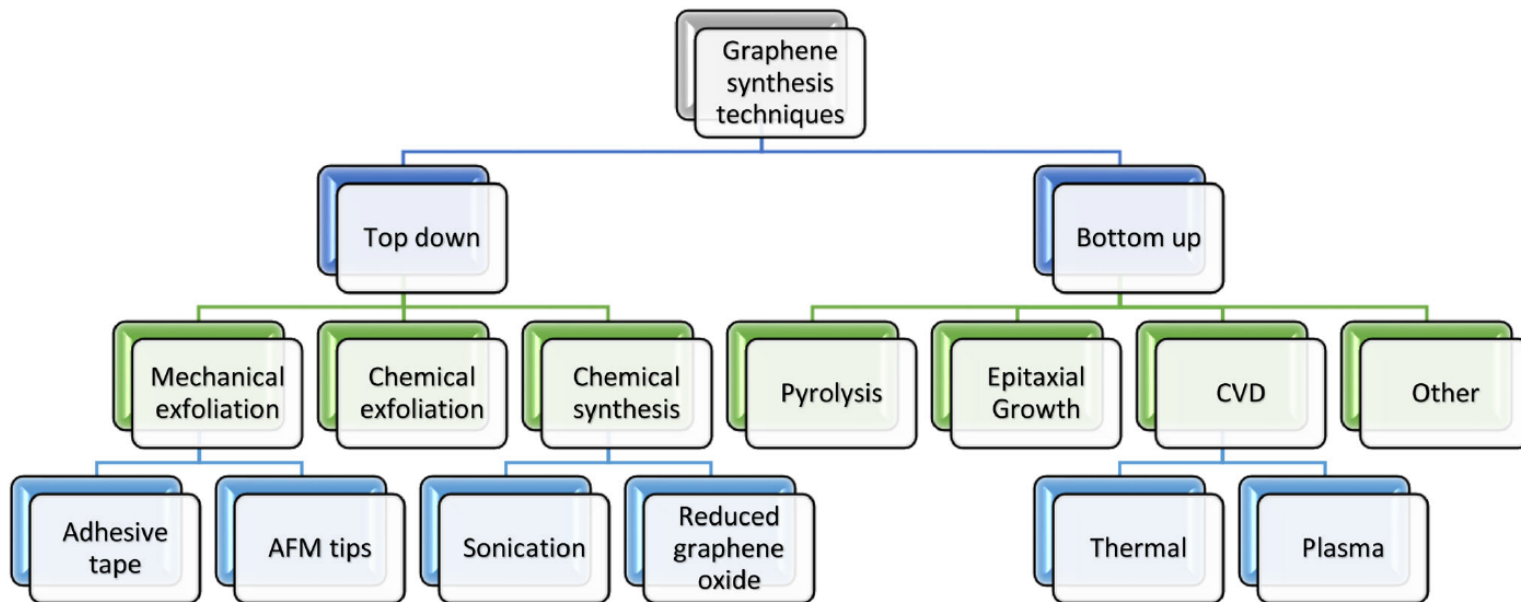
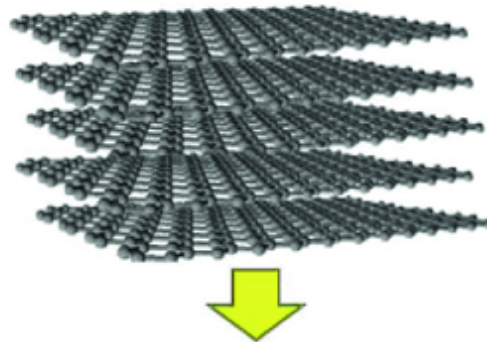
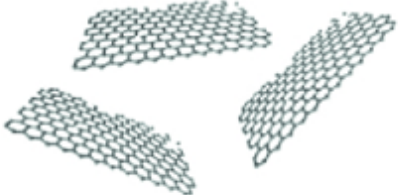


Fig. 2 A process flow chart of Graphene synthesis

Top-down

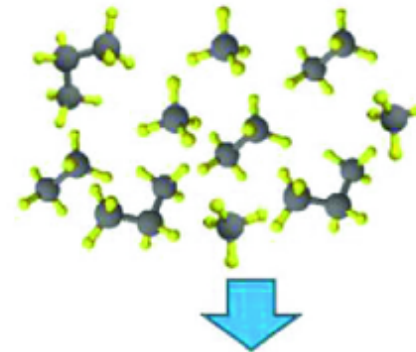
Source: Graphite

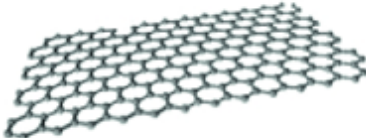


Mechanical exfoliation	Liquid phase and exfoliation	
Scotch tape, AFM tip.	Exfoliation of GIC	Reduction of GO
 <p>Graphene Size: nm~ μm</p>		
Low cost High quality	Low cost High Productivity Low defect	Low cost High Productivity Easy dispersion

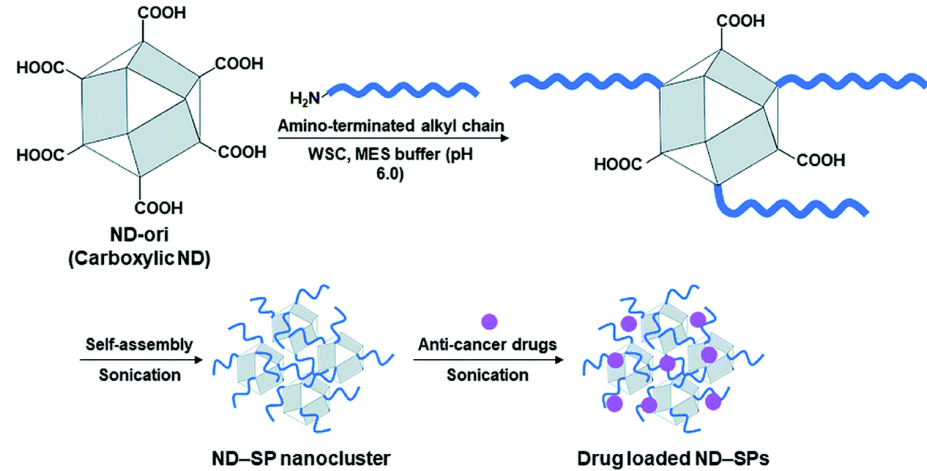
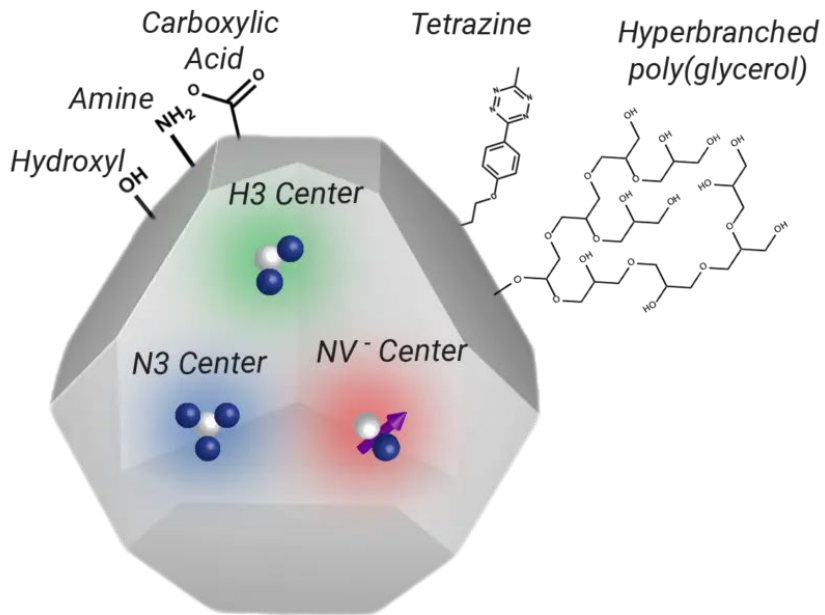
Bottom-up

Source: CH₄, C₂H₆, C₃H₈ gas/ SiC



Epitaxial growth	CVD
Annealing of SiC wafer	Dissolving CH ₄ gas to Ni or Cu/ fast cooling
 <p>Graphene Size: wafer size</p>	
High transparency High conductivity Flexibility	

Nanodiamond



Mechanism of Fluorescence in Nanodiamonds:

Formation of NV Centers: NV centers are created either naturally during diamond formation or artificially through processes such as ion implantation, electron irradiation, or annealing. These processes introduce nitrogen atoms and vacancies into the diamond lattice, which can then form NV centers upon appropriate annealing conditions.

Excitation: When NV centers in nanodiamonds are excited by light of a certain wavelength (usually in the green spectrum), they absorb energy and transition from their ground state to an excited state.

Photon Emission: The excited NV centers return to their ground state by emitting photons. This emission occurs at characteristic wavelengths in the red to near-infrared spectrum, leading to the observed fluorescence. The wavelength and intensity of the fluorescence can be influenced by the charge state of the NV center and the presence of other defects or impurities in the diamond lattice.

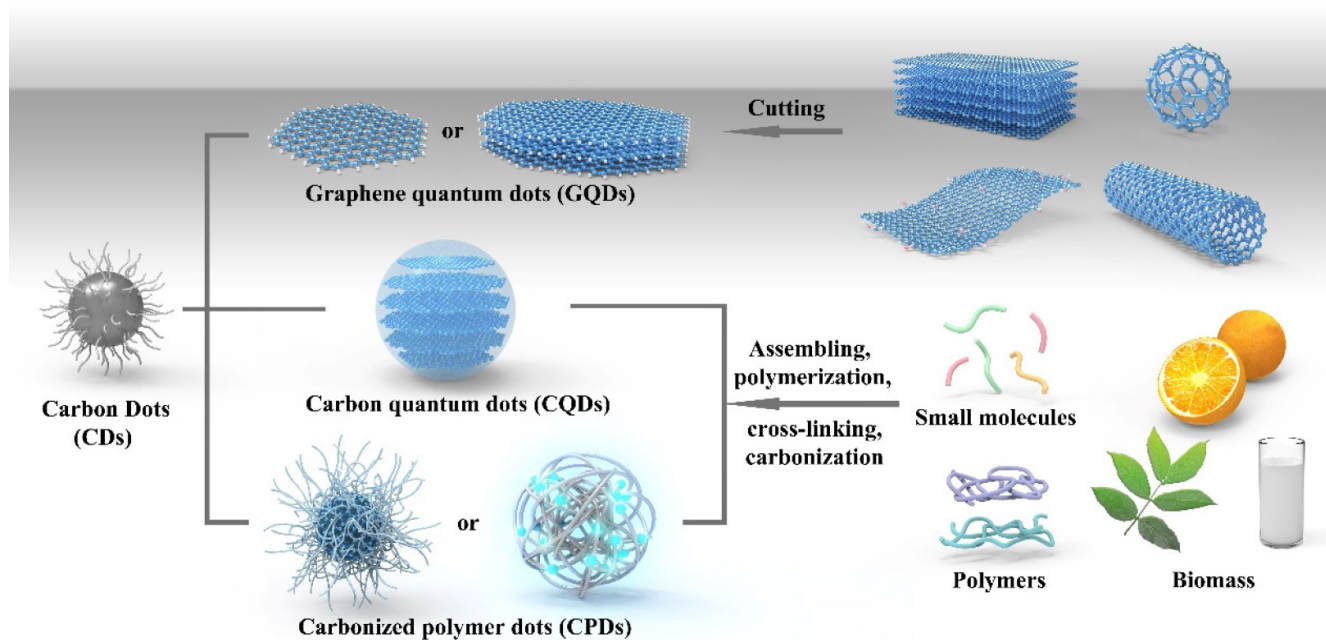
Unique Properties:

Stable Fluorescence: Unlike many organic fluorophores and some other fluorescent materials, NV centers in nanodiamonds are extremely photostable. They do not bleach or blink under standard imaging conditions, making them excellent candidates for long-term imaging and tracking applications in biological systems.

Biocompatibility: Nanodiamonds are generally considered biocompatible, which, combined with their stable fluorescence, makes them suitable for a variety of biomedical applications, including drug delivery tracking, cellular imaging, and biosensing.

Tunable Fluorescence: By controlling the size of the nanodiamonds and the concentration and type of defects (including NV centers), it is possible to tailor their optical properties to some extent.

Carbon Dots



Classification of CDs: including graphene quantum dots (GQDs), carbon quantum dots (CQDs), and carbonized polymer dots (CPDs), and their main preparation approaches.

Carbon quantum dots (CQDs) are nanometer-sized carbon-based materials that exhibit quantum mechanical properties, including fluorescence.

Characteristics of Carbon Quantum Dots

Size: Carbon quantum dots are typically less than 10 nanometers in diameter.

Composition: They are composed primarily of carbon elements, with some containing heteroatoms like nitrogen, oxygen, or sulfur to modify their electronic and optical properties.

Structure: The structure of CQDs can vary but often includes **graphene-like sp²-hybridized carbon sheets and sp³-hybridized carbon domains**.

Properties

Fluorescence: CQDs exhibit strong fluorescence, which is tunable based on **their size, surface functional groups, and doping elements**. This fluorescence is due to **quantum confinement and edge effects**, where the electronic properties are influenced by the size and structure of the quantum dots.

Photostability: They have high photostability, resisting photobleaching under prolonged illumination.

Biocompatibility: Carbon quantum dots are generally considered to be biocompatible and less toxic than traditional semiconductor quantum dots, making them suitable for biological and medical applications.

Water Solubility: Many CQDs are hydrophilic and easily solubilized in water, facilitating their use in biological environments.

Reasons for Fluorescence

The fluorescence of carbon quantum dots originates from several mechanisms, including **quantum confinement effects**, **surface states**, and **molecular fluorescence**. The exact mechanism can depend on the synthesis method, surface functionalization, and the presence of doping elements. Quantum confinement plays a significant role in smaller CQDs, where the movement of electrons is restricted to such a degree that it alters the electronic and optical properties of the material. Surface states, related to the functional groups attached to the surface of CQDs, also significantly influence their optical properties. Additionally, the presence of specific dopants can introduce localized energy states in the band gap, further affecting fluorescence.

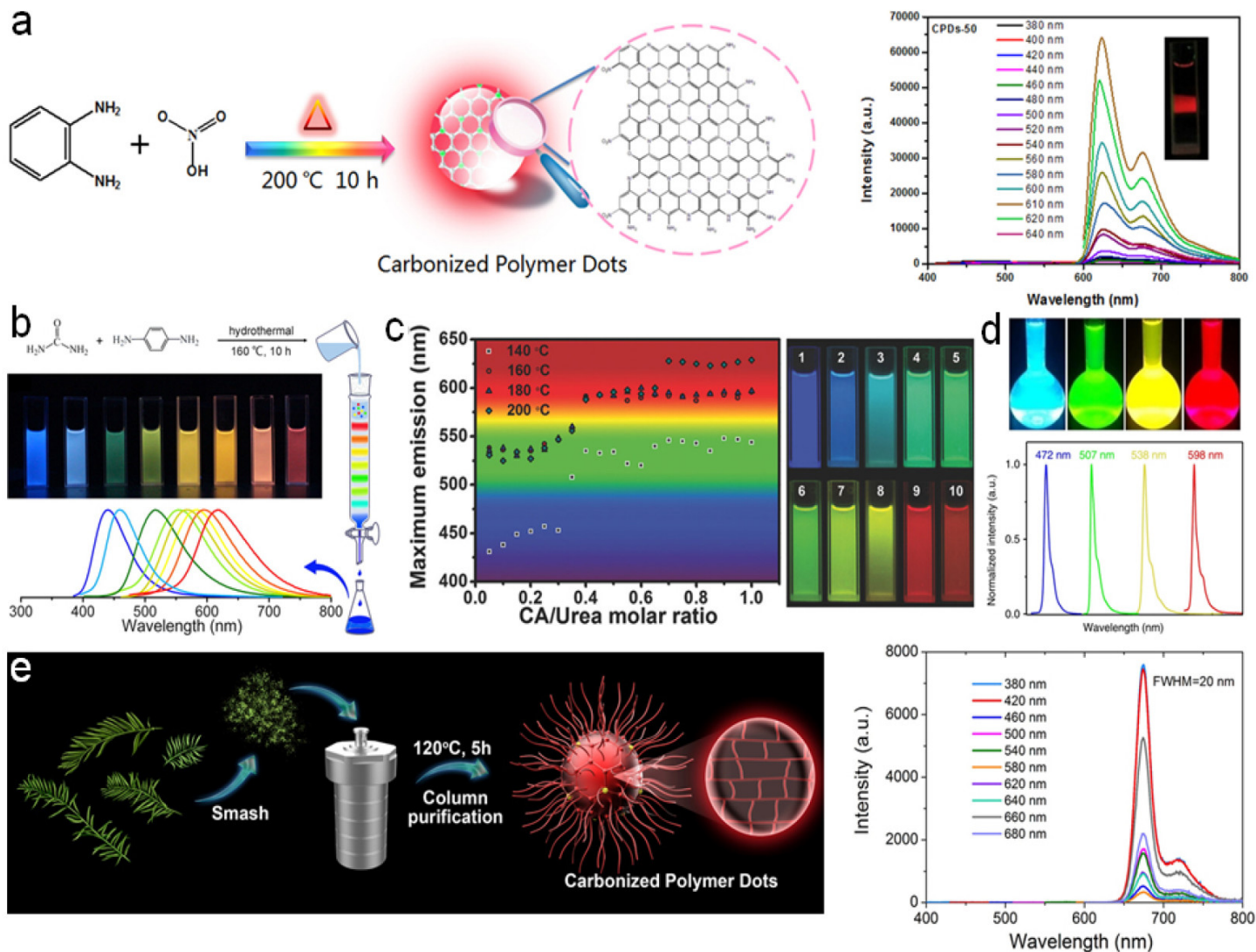
Applications

Bioimaging: Their biocompatibility and tunable fluorescence make them excellent candidates for fluorescent labeling and imaging in biological systems.

Sensing: CQDs can be engineered to detect various chemicals and biomolecules, making them useful in environmental monitoring and diagnostics.

Photocatalysis: Their ability to absorb and transfer energy efficiently makes them useful in photocatalytic applications, such as degradation of pollutants and water splitting.

Optoelectronics: CQDs are explored for use in light-emitting diodes (LEDs), solar cells, and other optoelectronic devices due to their electronic and optical properties. The research and development of carbon quantum dots continue to evolve, revealing new insights into their properties and expanding their range of applications.



Syntheses and optical properties of CDs. Synthesis and PL spectra of (a) red emissive CPDs and (b) multicolor CPDs. Optical properties of (c) multicolor CPDs and (d) CQDs. (e) Synthesis and PL spectra of deep red emissive CPDs.

Porous Materials

- AAO

- MCM-41

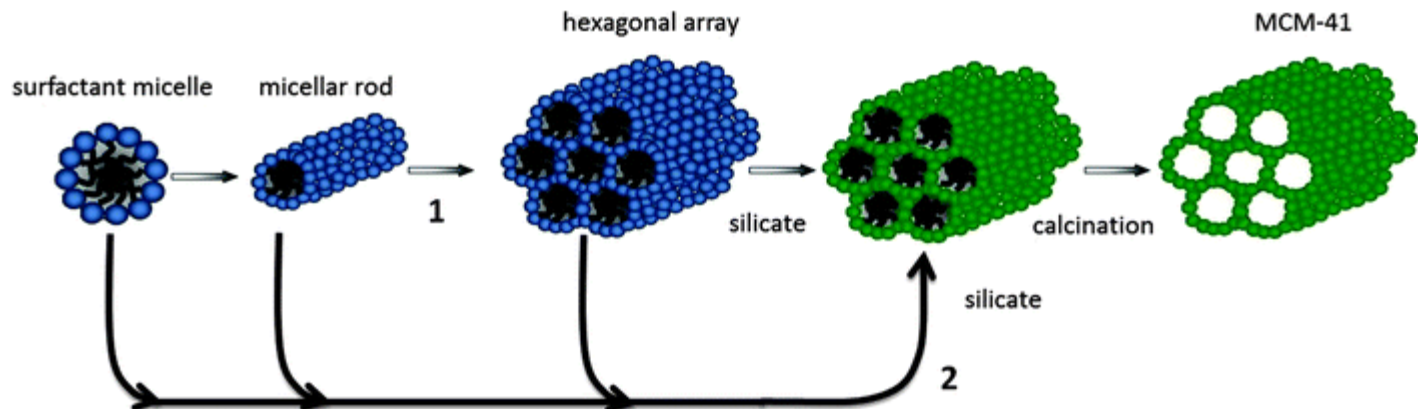
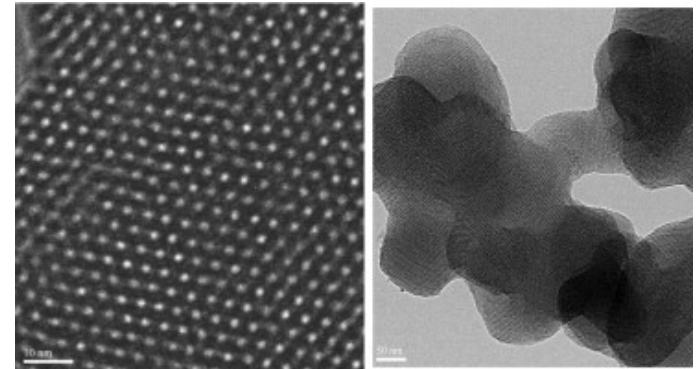
Mobil Crystalline Materials, or MCM-41

Santa Barbara Amorphous type material, or SBA-15

- Micro: $< 2\text{nm}$

- Meso:

- Macro: $> 50\text{nm}$



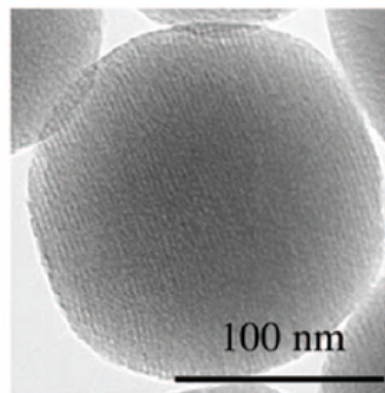
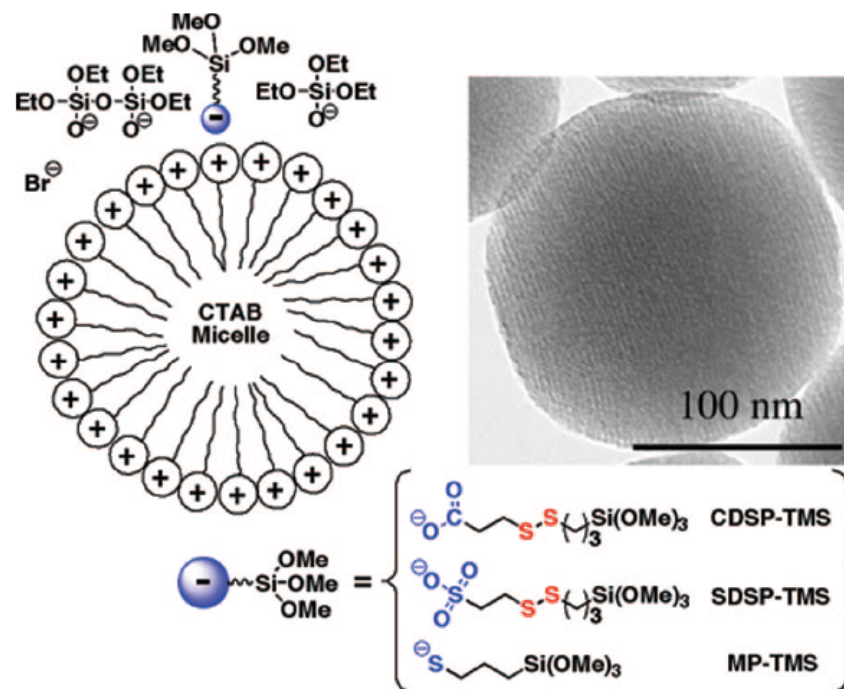


FIGURE 3. Schematic representation of the use of anionic organoalkoxysilanes for controlling the functionalization of the MSN materials. The MCM-41-type mesoporous channels are illustrated by the parallel stripes shown in the transmission electron microscopy (TEM) micrograph of the MSN-SH material. Reproduced with permission from ref 15. Copyright 2005, Royal Society of Chemistry.

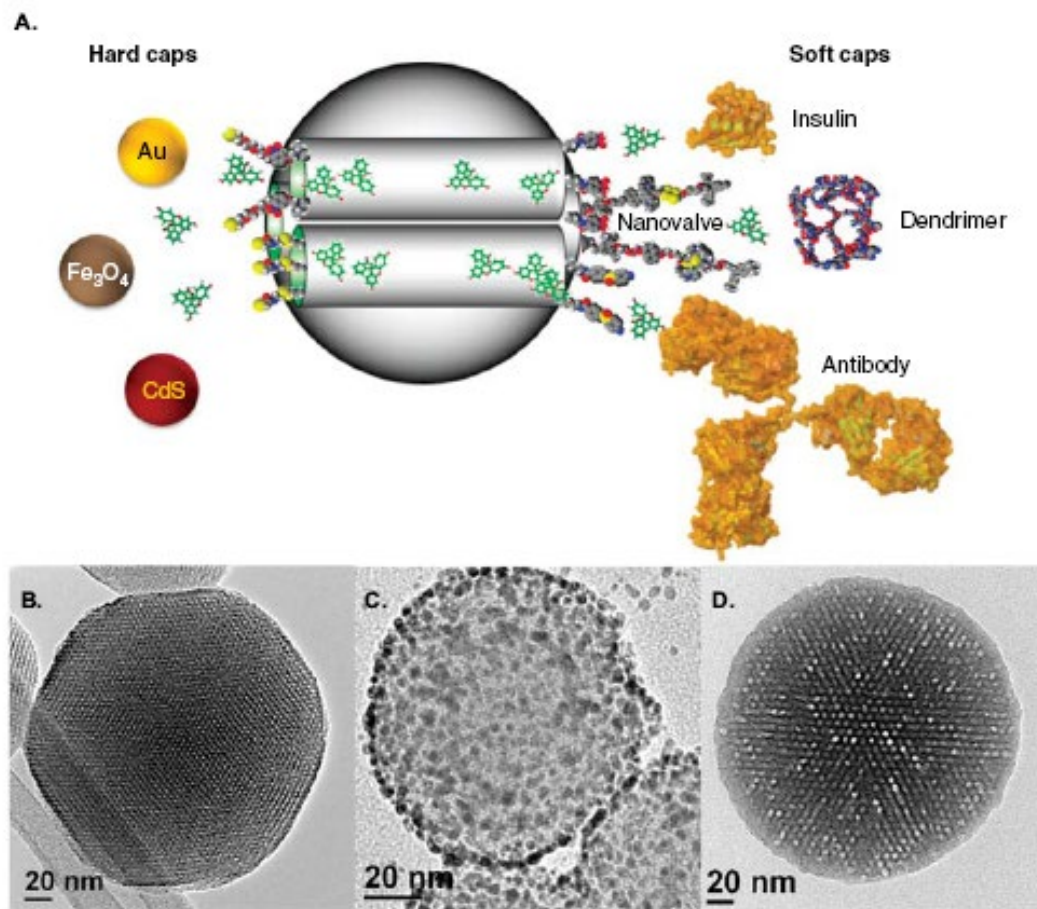


Figure 1. A. Schematic representation of a MSN loaded with drugs and capped with hard caps and soft caps highlighted in this review. Transmission electron microscopy images of (B) a MSN along the axis of the mesopores, (C) capped with hard (Au NP) and (D) with soft (polymer) caps.

MSN: Mesoporous silica nanoparticle.

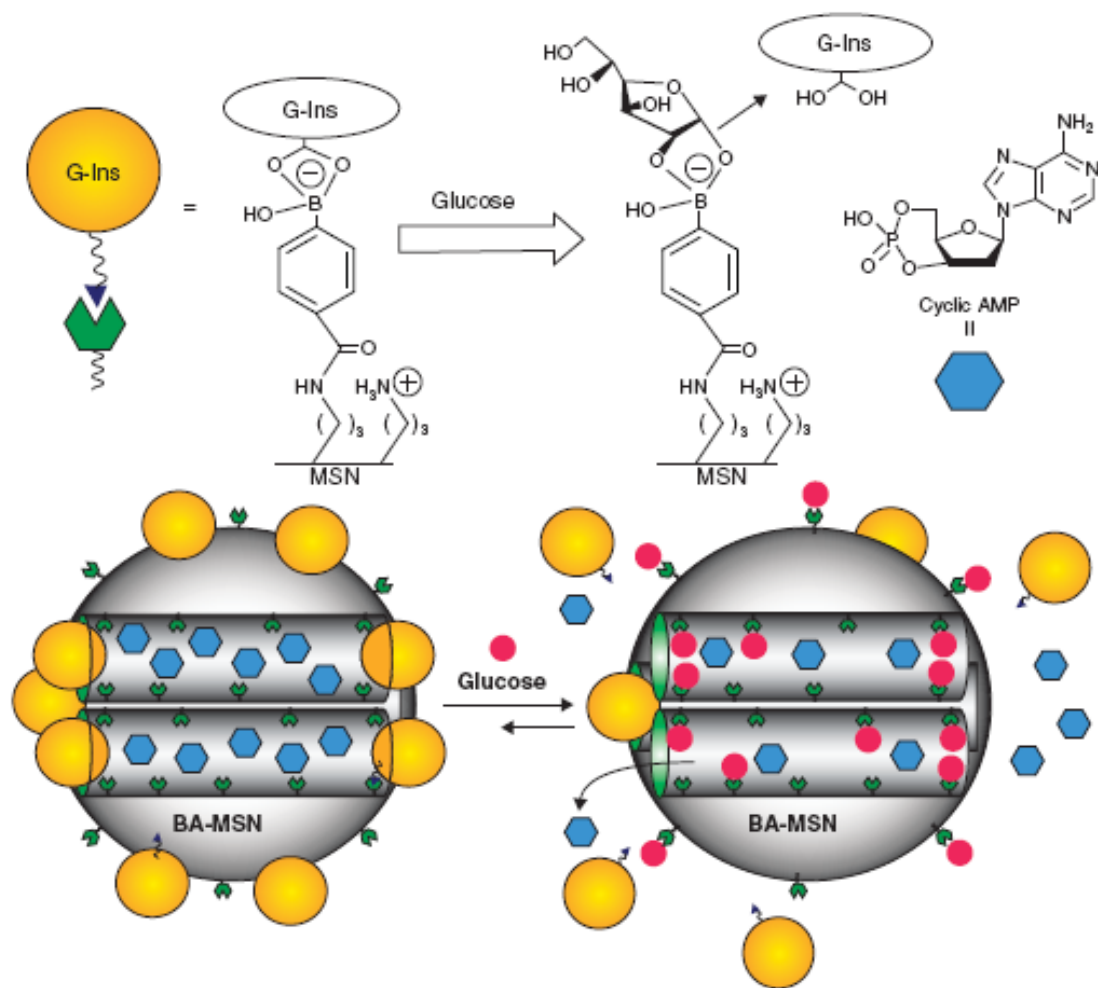
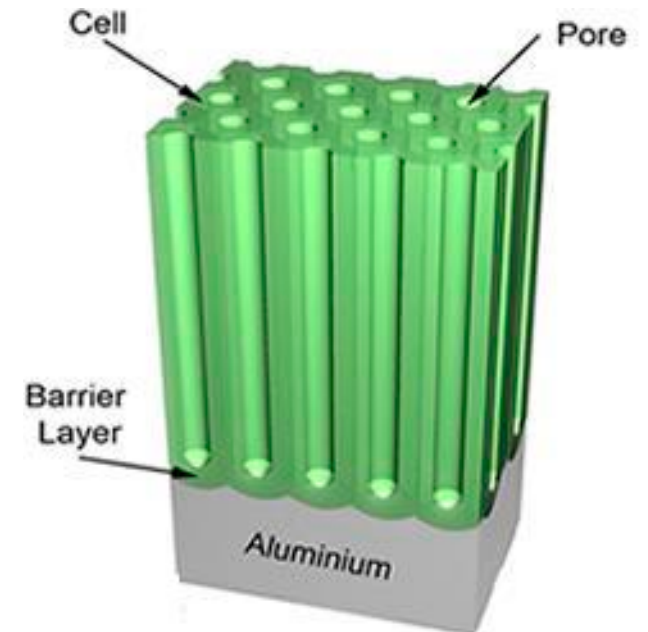
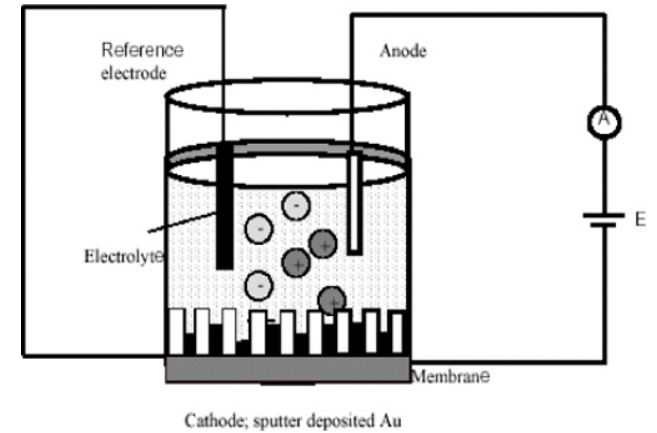
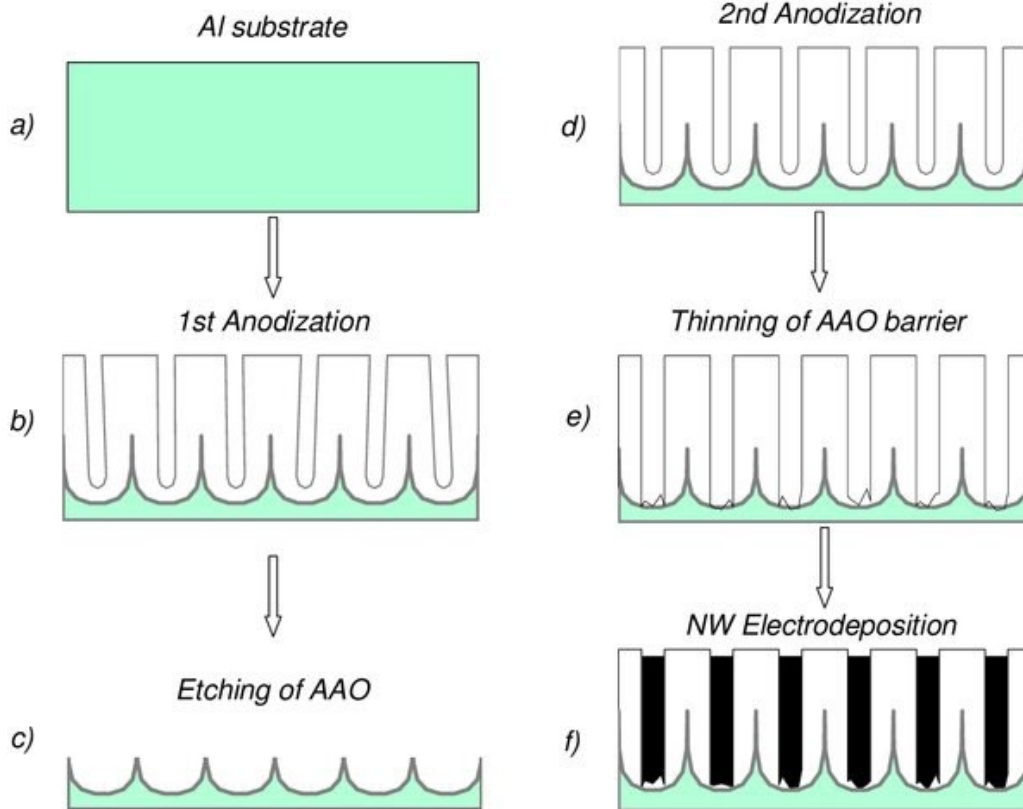


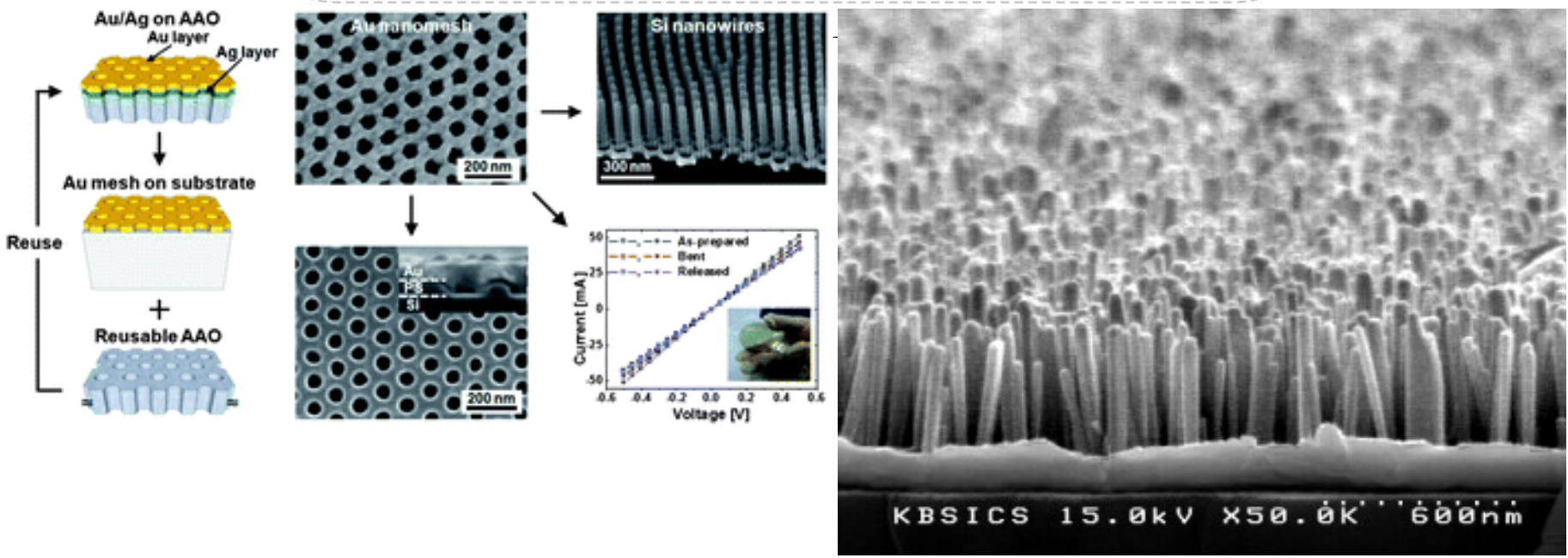
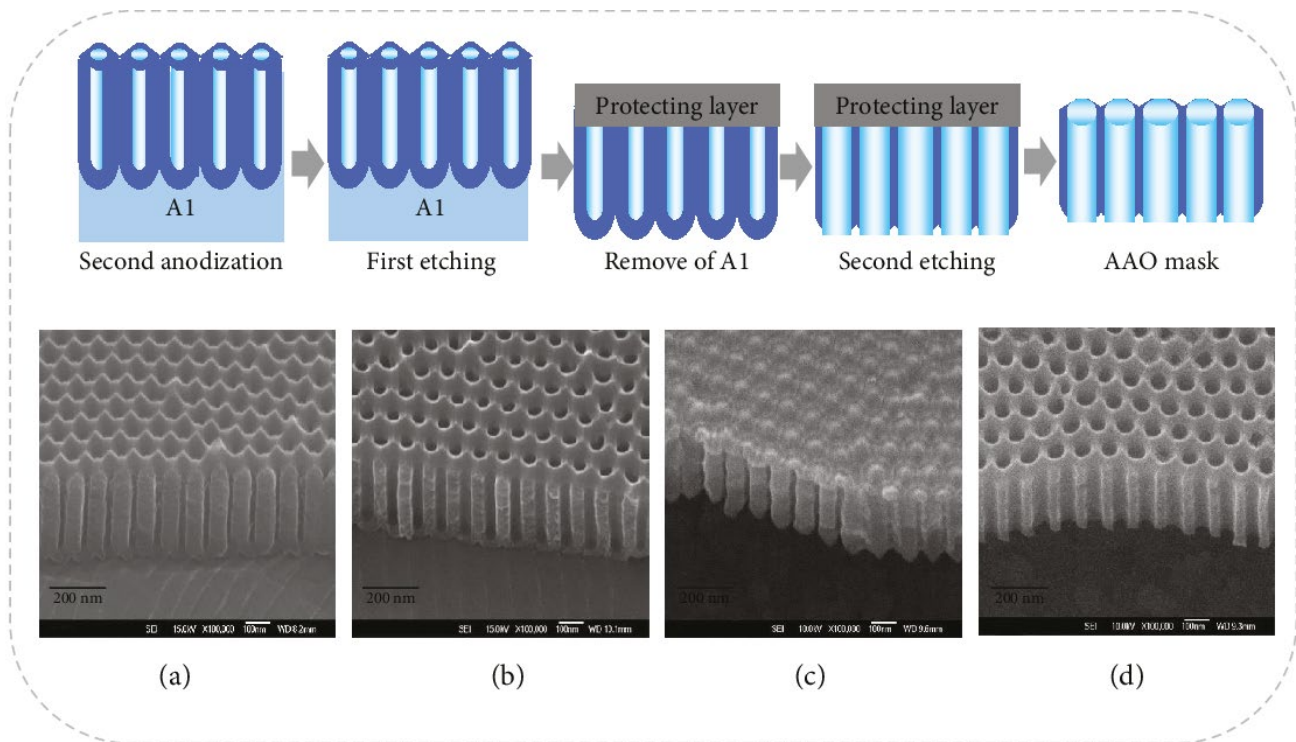
Figure 5. Schematic representation of the glucose-responsive MSN-based double delivery system for controlled release of bioactive G-Ins and cyclic AMP. The controlled release mechanism was achieved by means of the displacement reaction between blood glucose and G-Ins based on reversible boronic acid-diols complexation. High glucose concentration triggers the G-Ins uncapping and the release of cyclic AMP sequentially to diminish the higher than normal level of blood glucose.

Reproduced with permission from [19].

G-Ins: G-insulin; MSN: Mesoporous silica nanoparticle.

AAO

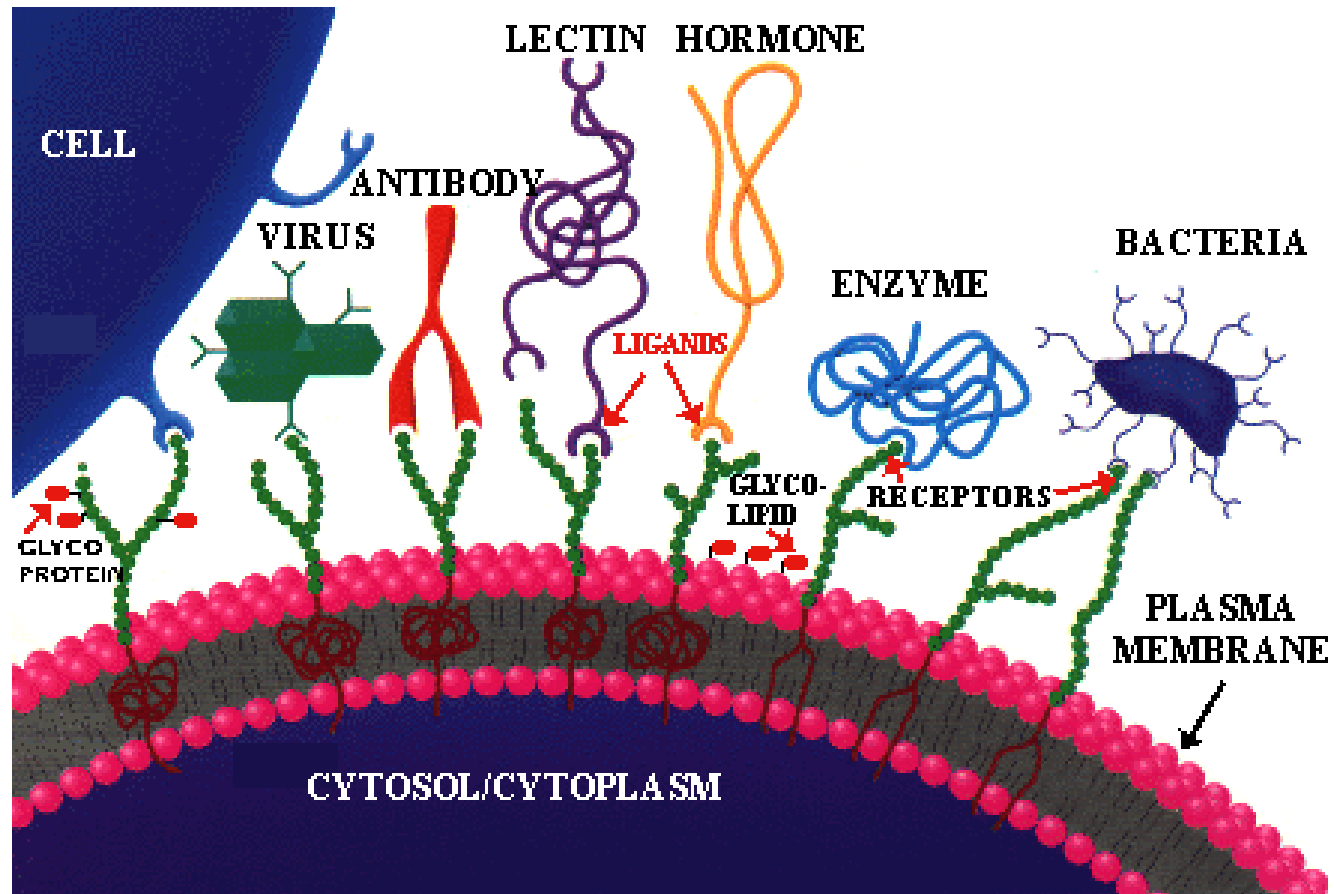




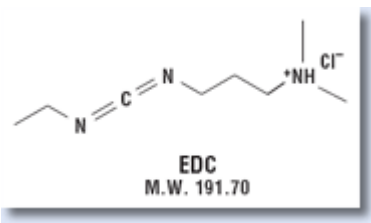
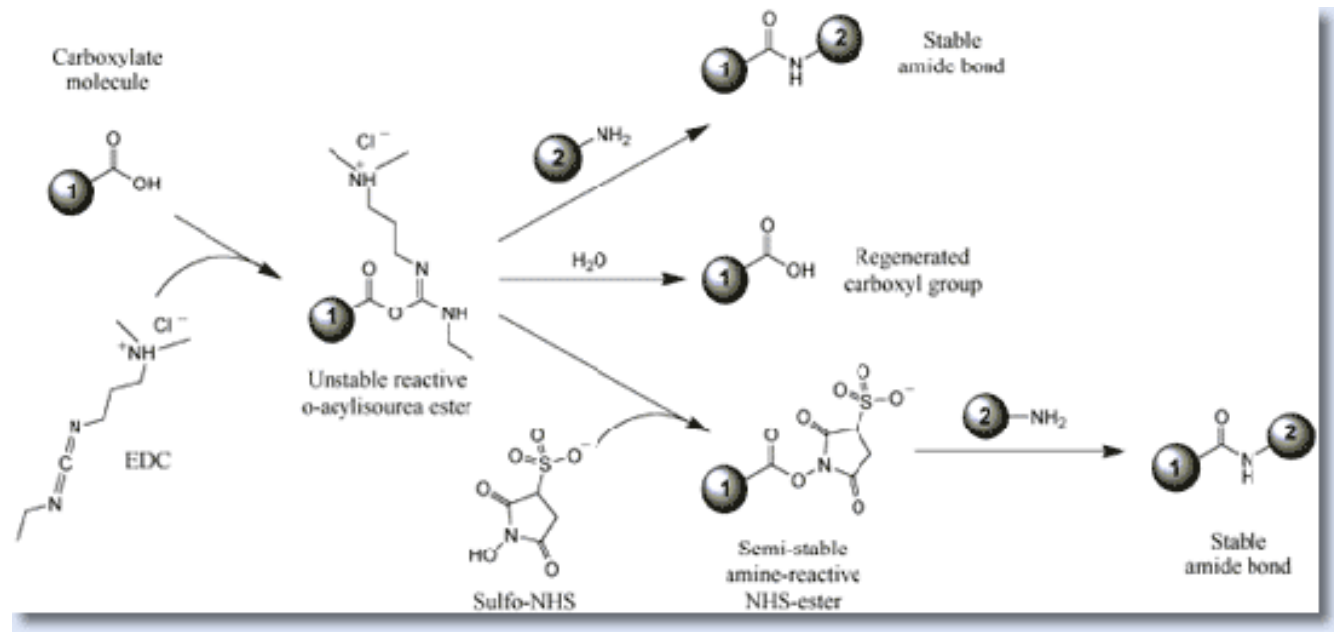
Surface Functionalization

- Recognition
 - Molecular Recognition
 - Protein
 - DNA
 - Saccharide
- Reporting/Detection
 - Dye
 - Quantum dots
 - SPR
 - SERS/LSPR
- Separation
 - Gel/Chromatography
 - Magnetic
- Surfaces
 - Gold and silver
 - Silicon oxide (glass)
 - Quantum dots
 - Polymer

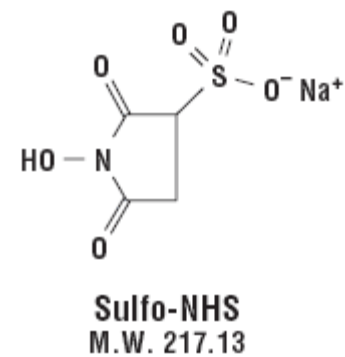
Molecular Recognition



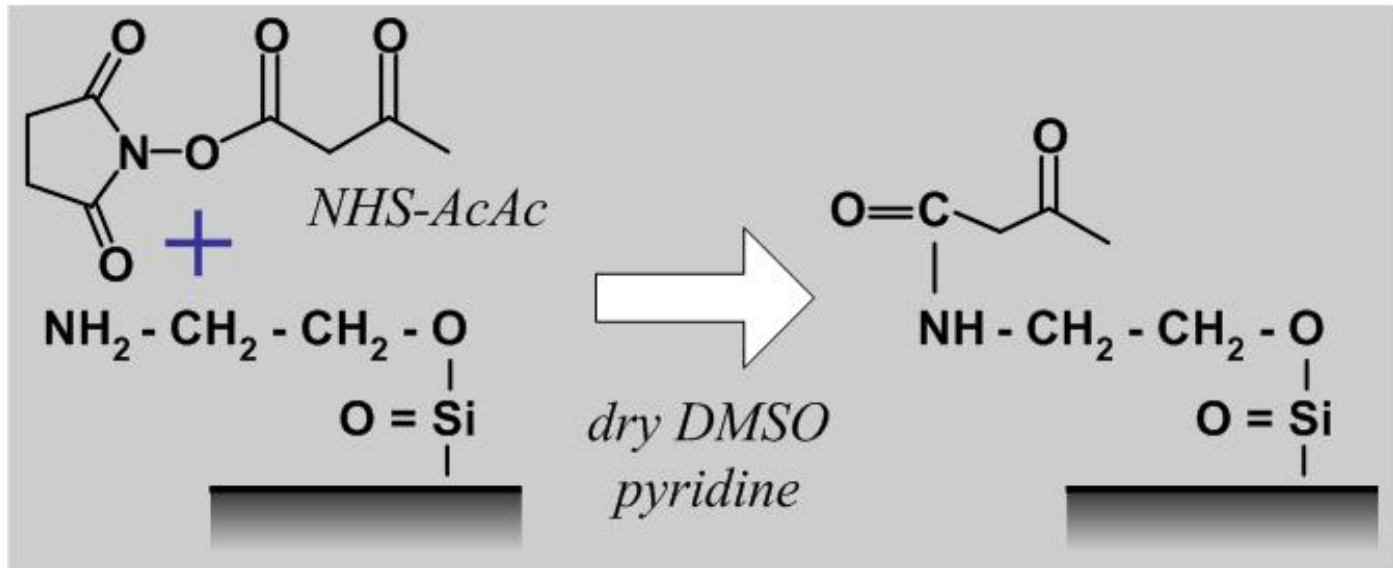
Carboxyl Presenting Surfaces



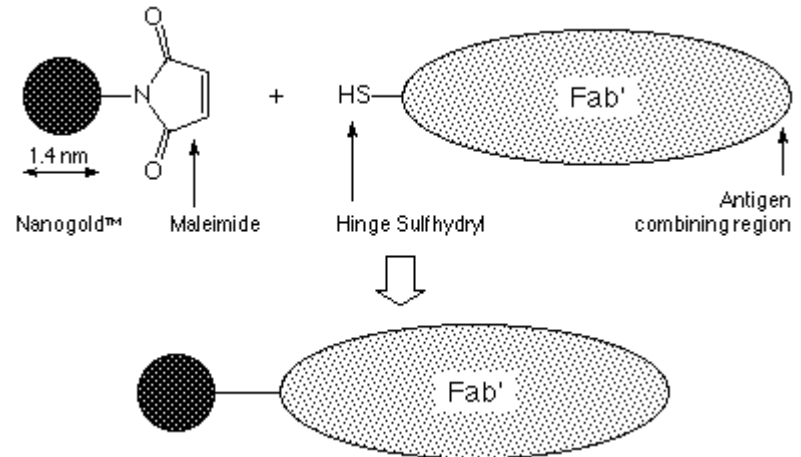
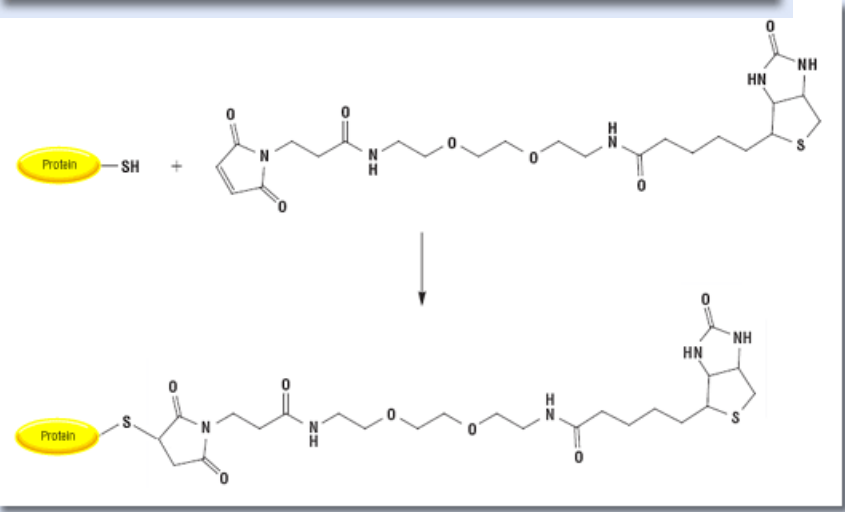
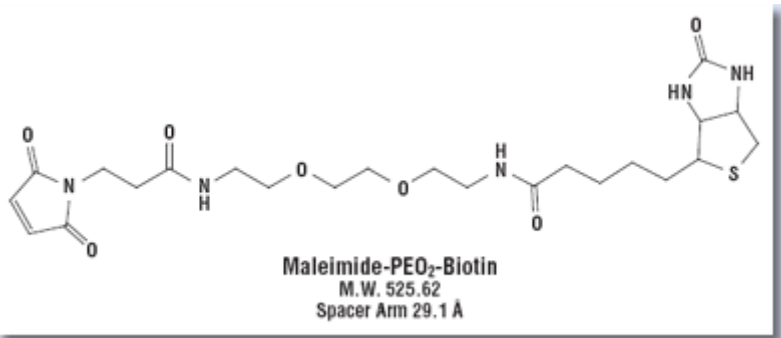
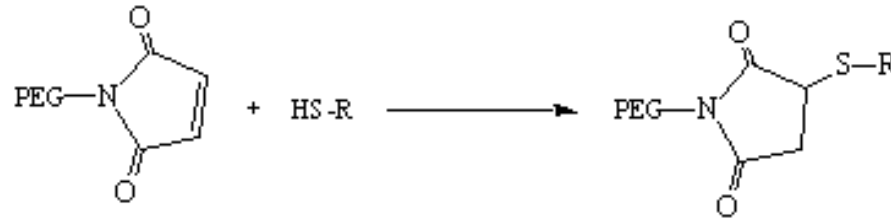
EDC (1-Ethyl-3-[3-dimethylaminopropyl]carbodiimide Hydrochloride)



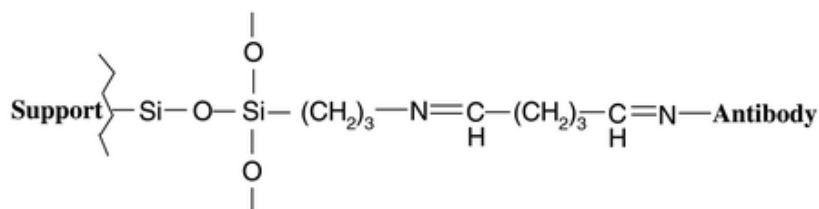
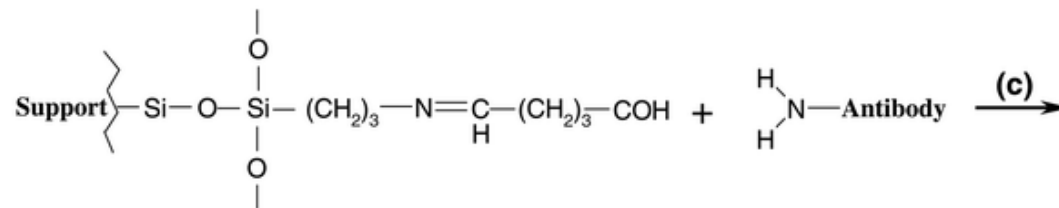
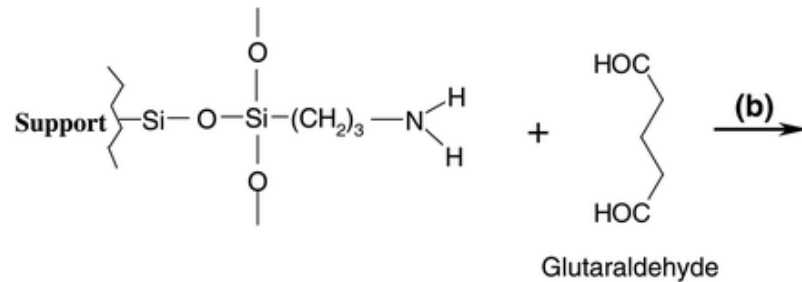
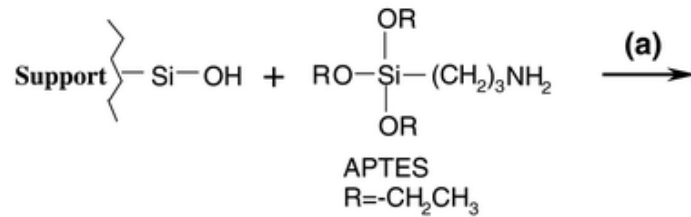
Amine Presenting Surface



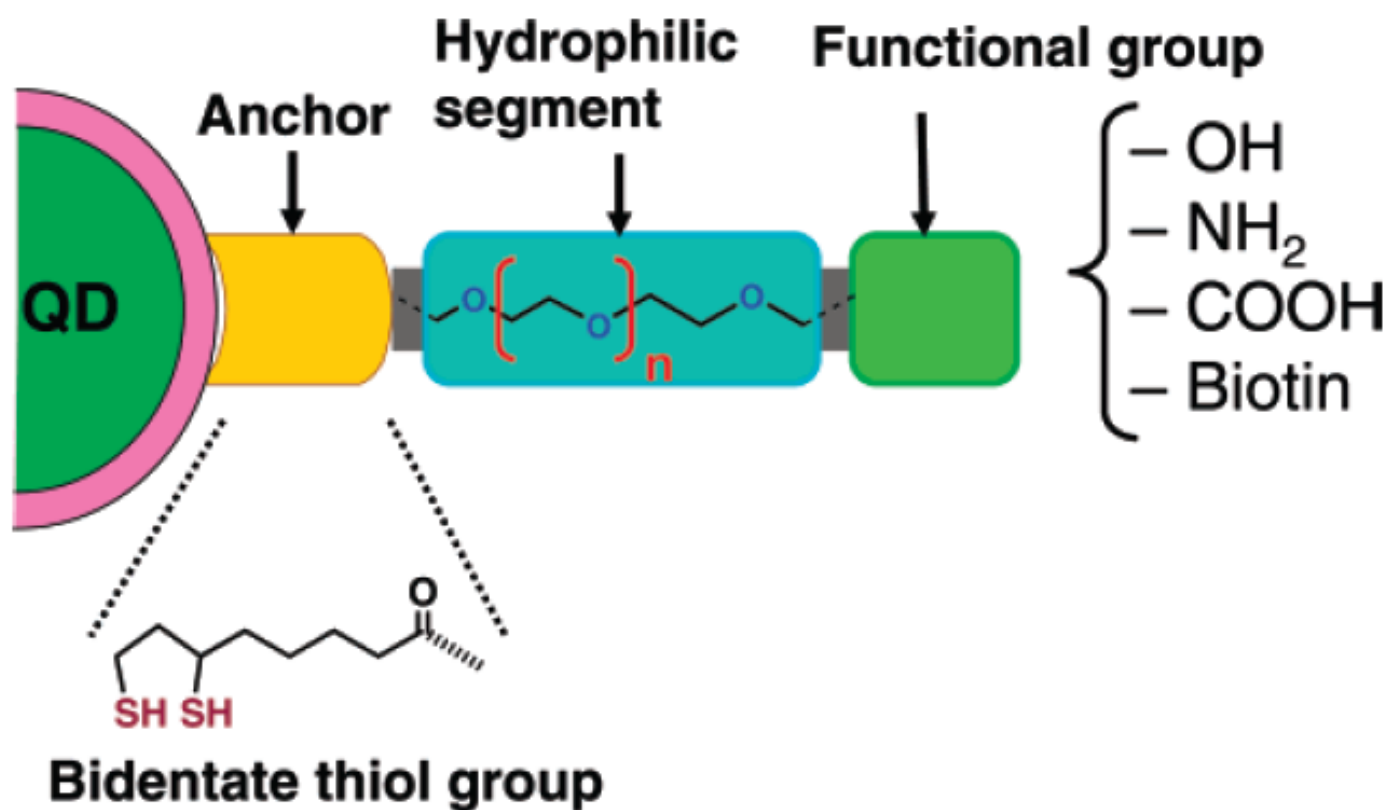
Sulfhydryl Labeling



Silica Modification



Scheme 1. Modular Design of Hydrophilic Ligands with Terminal Functional Groups Used in This Study



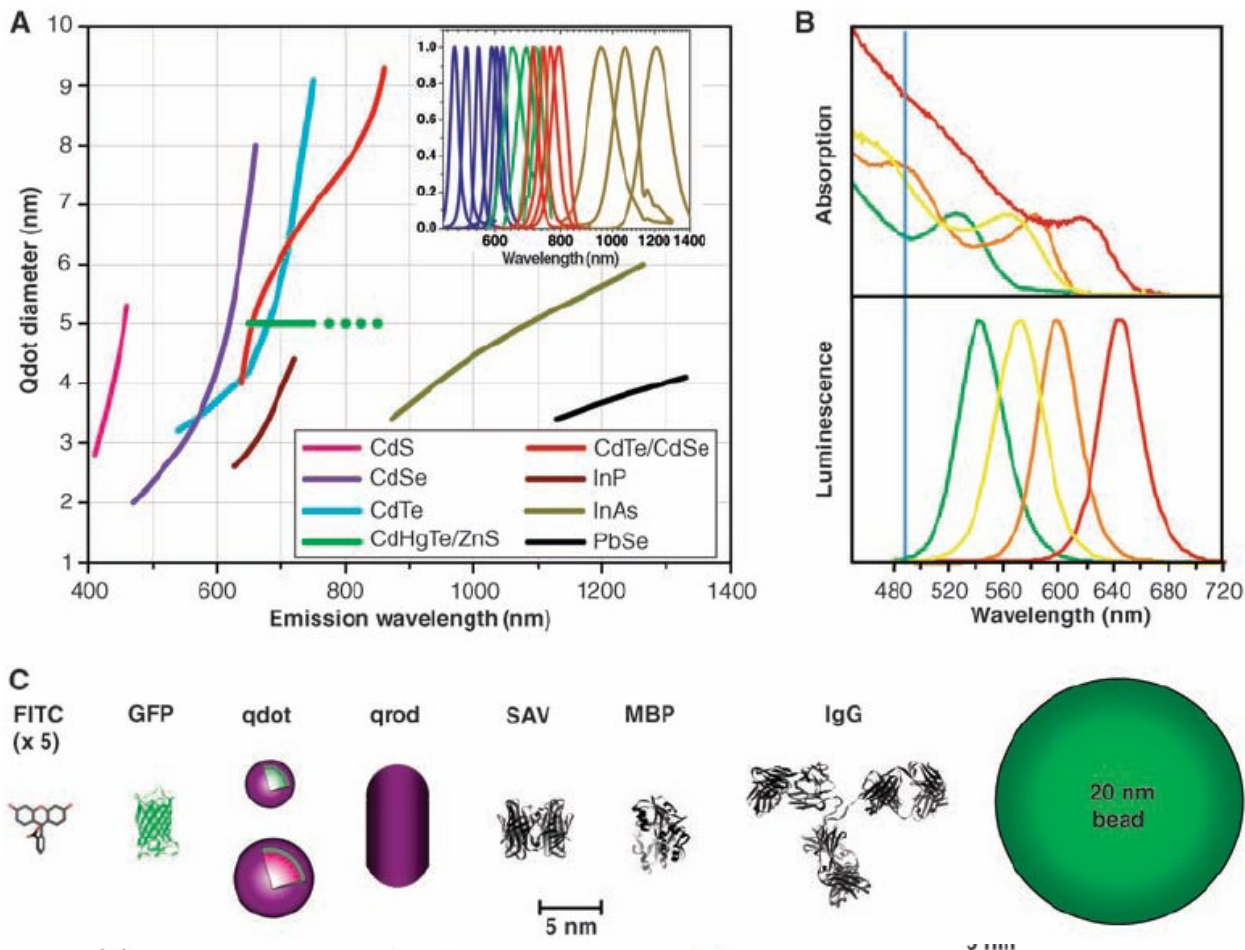
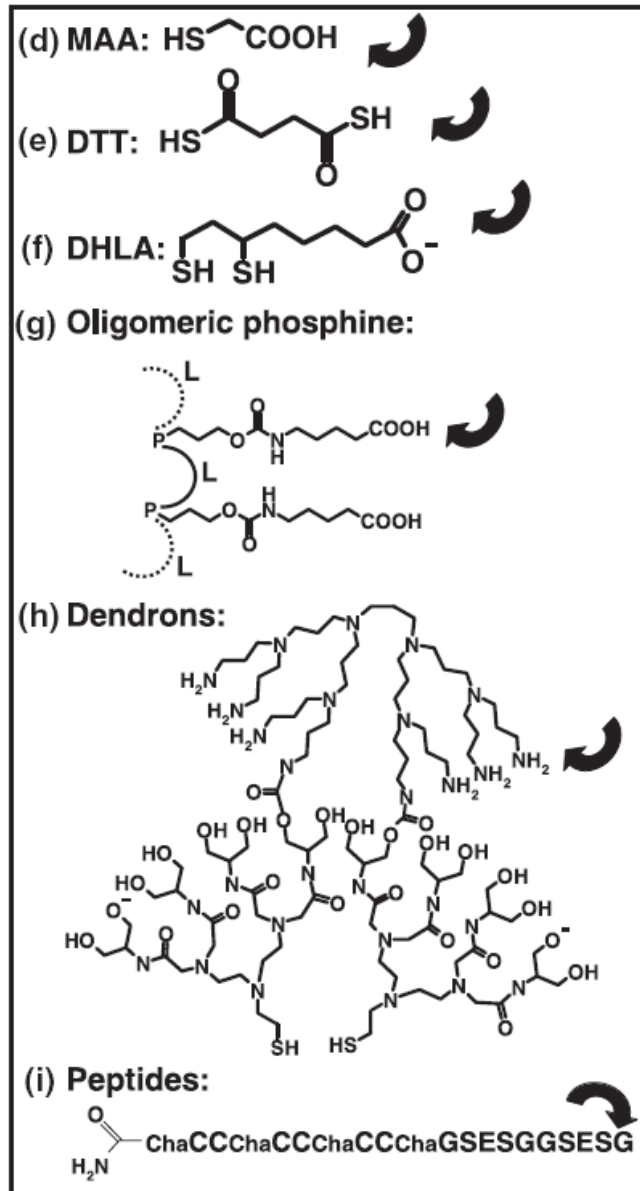
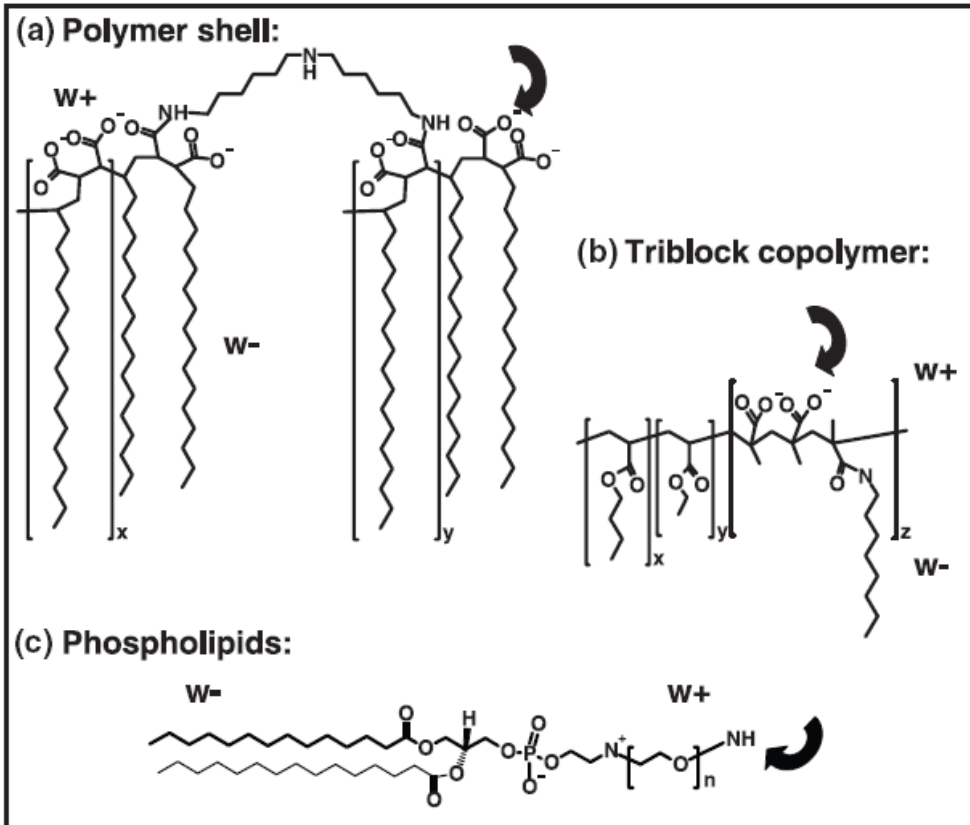
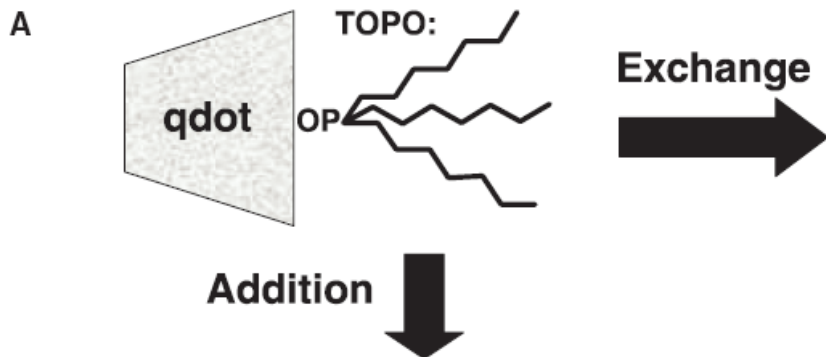
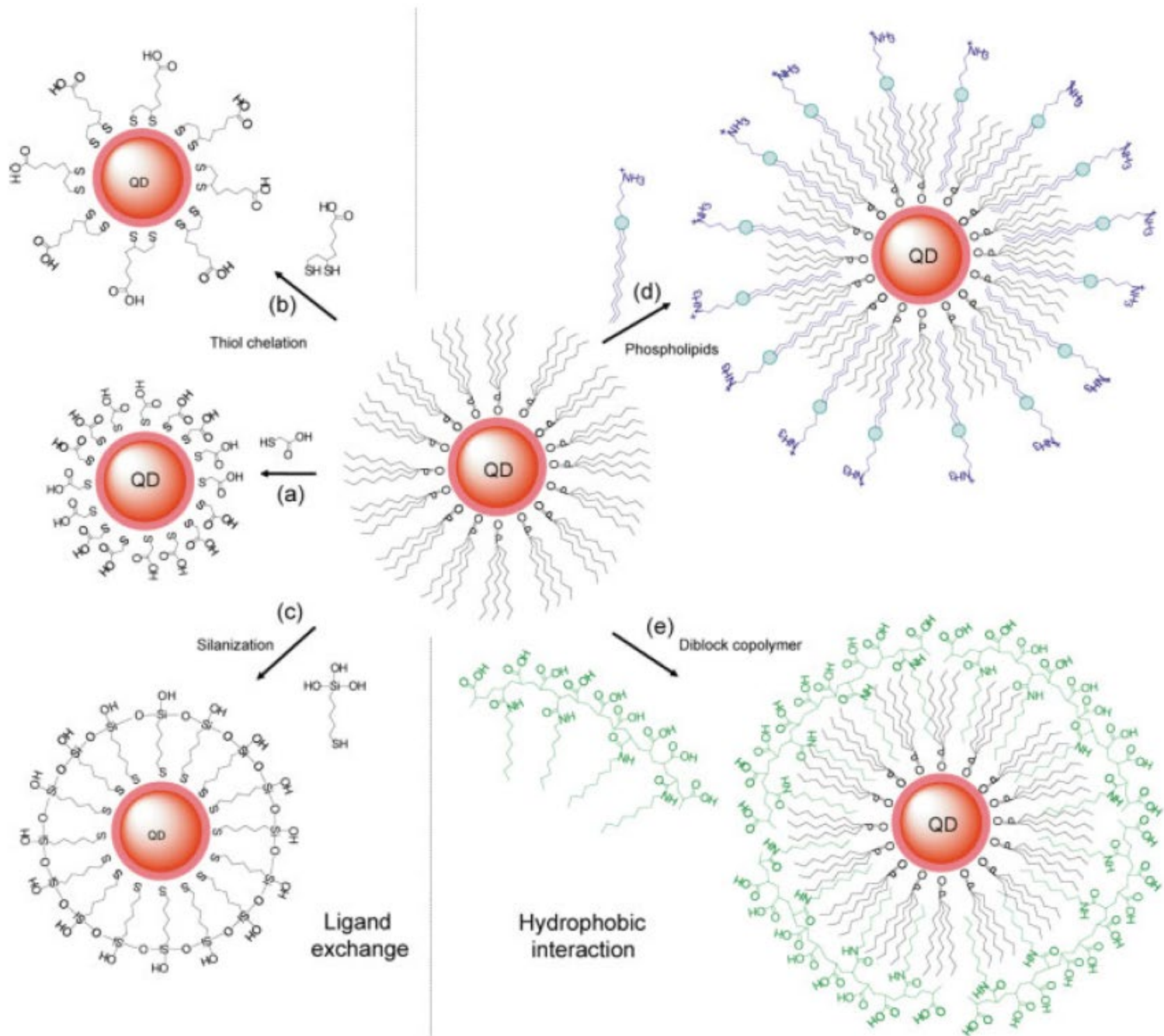


Fig. 1. (A) Emission maxima and sizes of quantum dots of different composition. Quantum dots can be synthesized from various types of semiconductor materials (II-VI: CdS, CdSe, CdTe...; III-V: InP, InAs...; IV-VI: PbSe...) characterized by different bulk band gap energies. The curves represent experimental data from the literature on the dependence of peak emission wavelength on qdot diameter. The range of emission wavelength is 400 to 1350 nm, with size varying from 2 to 9.5 nm (organic passivation/solubilization layer not included). All spectra are typically around 30 to 50 nm (full width at half maximum). Inset: Representative emission spectra for some materials. Data are from (12, 18, 27, 76–82). Data for CdHgTe/ZnS have been extrapolated to the maximum emission wavelength obtained in our group. (B) Absorption (upper curves) and emission (lower curves) spectra of four CdSe/ZnS qdot samples. The blue vertical line indicates the 488-nm line of an argon-ion laser, which can be used to efficiently excite all four types of qdots simultaneously. [Adapted from (28)] (C) Size comparison of qdots and comparable objects. FITC, fluorescein isothiocyanate; GFP, green fluorescent protein; qdot, green (4 nm, top) and red (6.5 nm, bottom) CdSe/ZnS qdot; qrod, rod-shaped qdot (size from Quantum Dot Corp.'s Web site). Three proteins—streptavidin (SAV), maltose binding protein (MBP), and immunoglobulin G (IgG)—have been used for further functionalization of qdots (see text) and add to the final size of the qdot, in conjunction with the solubilization chemistry (Fig. 2).





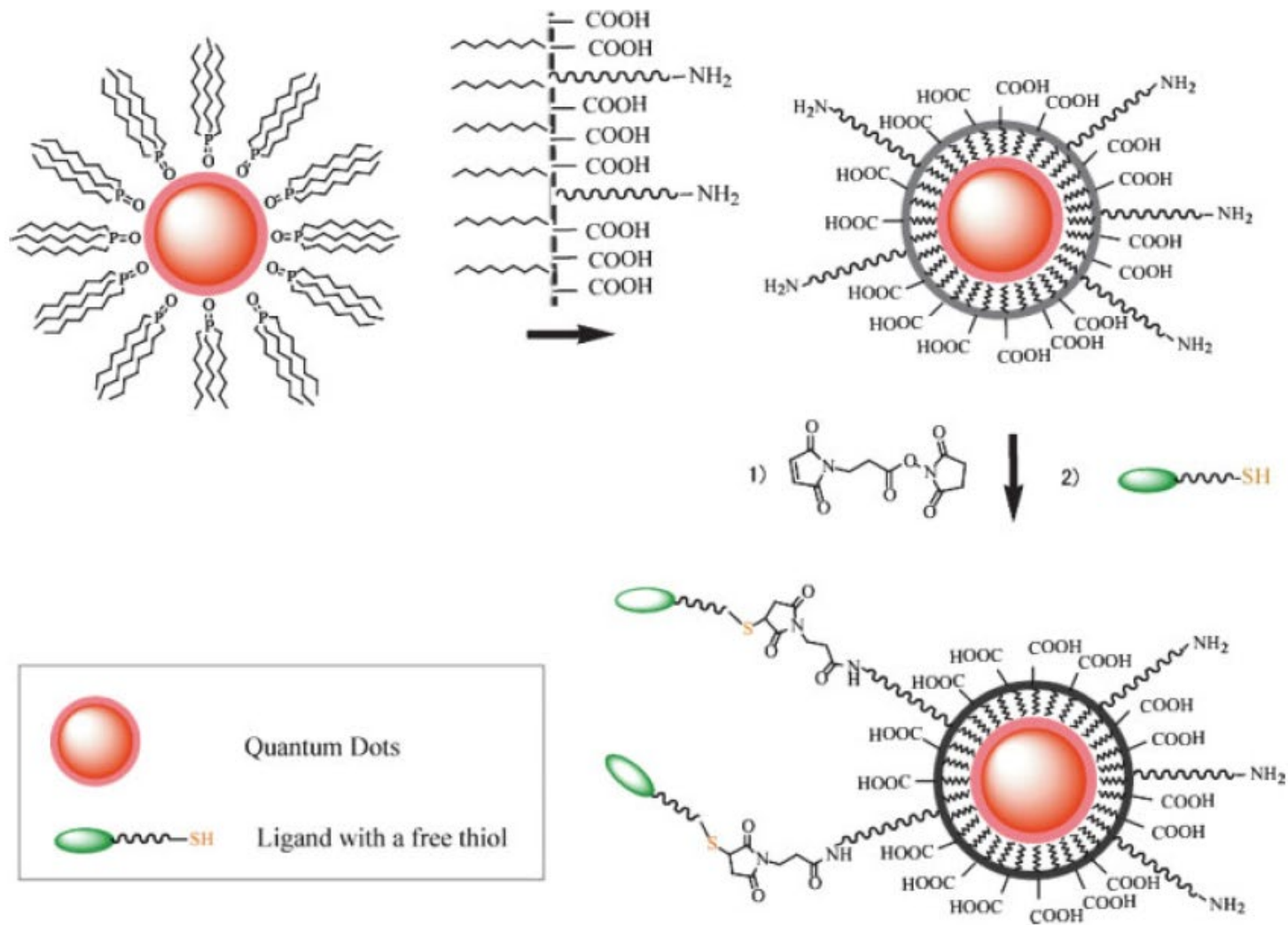


FIGURE 3 Maleimide functionalized QDs for conjugating thiol-containing ligands. TOPO stabilized QDs are coated with a primary amine functionalized tri-block amphiphilic copolymer for producing water-soluble QDs, which facilitate further conjugation to ligands with free thiols through bi-functional cross-linkers.

Nanomaterials for Biodiagnostic

- Nucleic Acid
 - Genetic information for identification
 - Diseases, bacterium, virus, pathogen
 - PCR with molecular fluorophore, State of the Art
 - Expansive, Non-portable, Non-multiplexing
- Proteins
 - Cancers and diseases, unusual high concentration of marker
 - ELISA (\sim pM) with molecular fluorophore
 - No PCR version

Colorimetric Detection of DNA

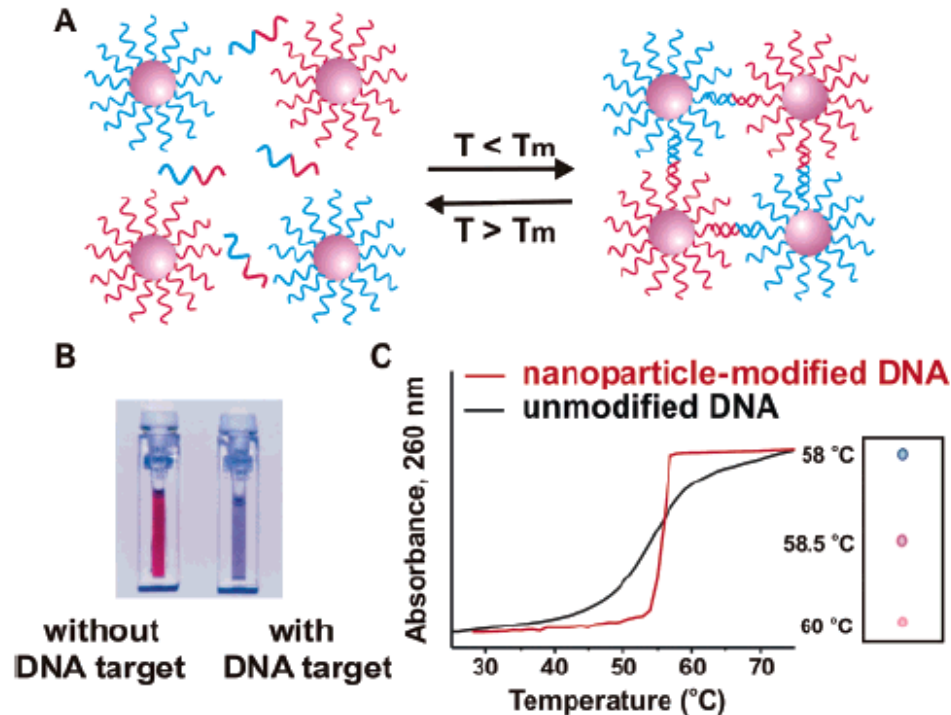


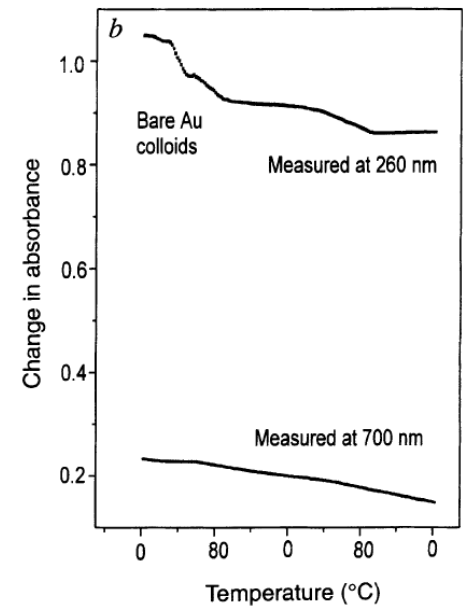
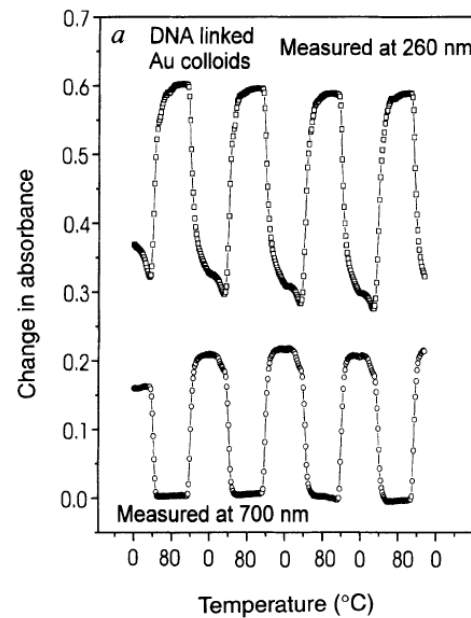
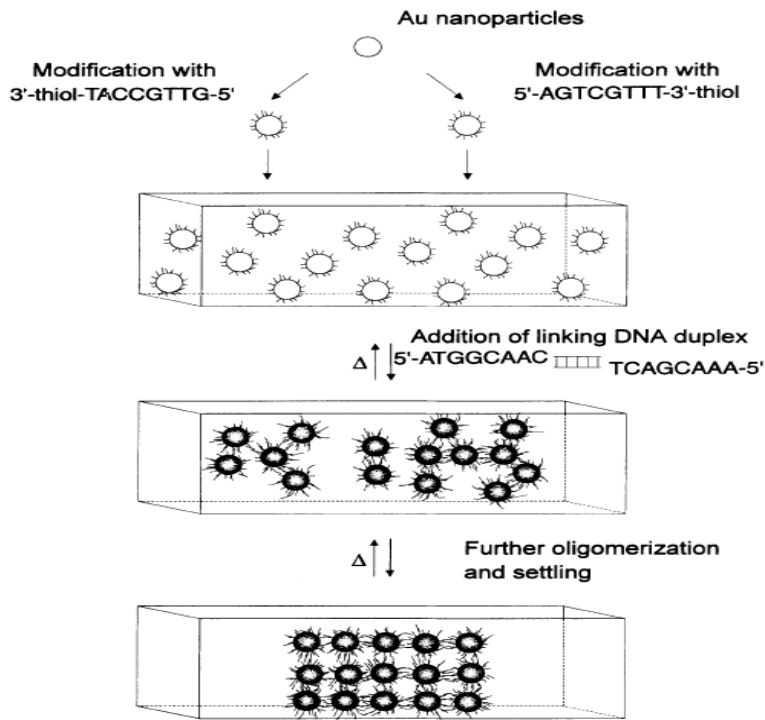
Figure 2. In the presence of complementary target DNA, oligonucleotide-functionalized gold nanoparticles will aggregate (A), resulting in a change of solution color from red to blue (B). The aggregation process can be monitored using UV-vis spectroscopy or simply by spotting the solution on a silica support (C). (Reprinted with permission from *Science* (<http://www.aaas.org>), ref 29. Copyright 1997 American Association for the Advancement of Science.)

A DNA-based method for rationally assembling nanoparticles into macroscopic materials

Chad A. Mirkin, Robert L. Letsinger, Robert C. Mucic & James J. Storhoff



FIG. 2 Cuvettes with the Au colloids and the four DNA strands responsible for the assembly process. Left cuvette, at 80 °C with DNA-modified colloids in the unhybridized state; centre, after cooling to room temperature but before the precipitate settles; and right, after the polymeric precipitate settles to the bottom of the cuvette. Heating either of these cool solutions results in the reformation of the DNA-modified colloids in the unhybridized state (shown in the left cuvette).



Selective Colorimetric Detection of Polynucleotides Based on the Distance-Dependent Optical Properties of Gold Nanoparticles

Robert Elghanian, James J. Storhoff, Robert C. Mucic, Robert L. Letsinger,* Chad A. Mirkin*

SCIENCE • VOL. 277 • 22 AUGUST 1997

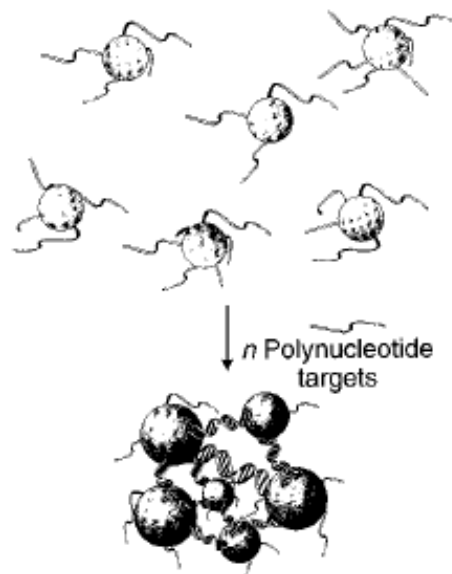


Fig. 1. Schematic representation of the concept for generating aggregates signaling hybridization of nanoparticle-oligonucleotide conjugates with oligonucleotide target molecules. The nanoparticles and the oligonucleotide interconnects are not drawn to scale, and the number of oligomers per particle is believed to be much larger than depicted.

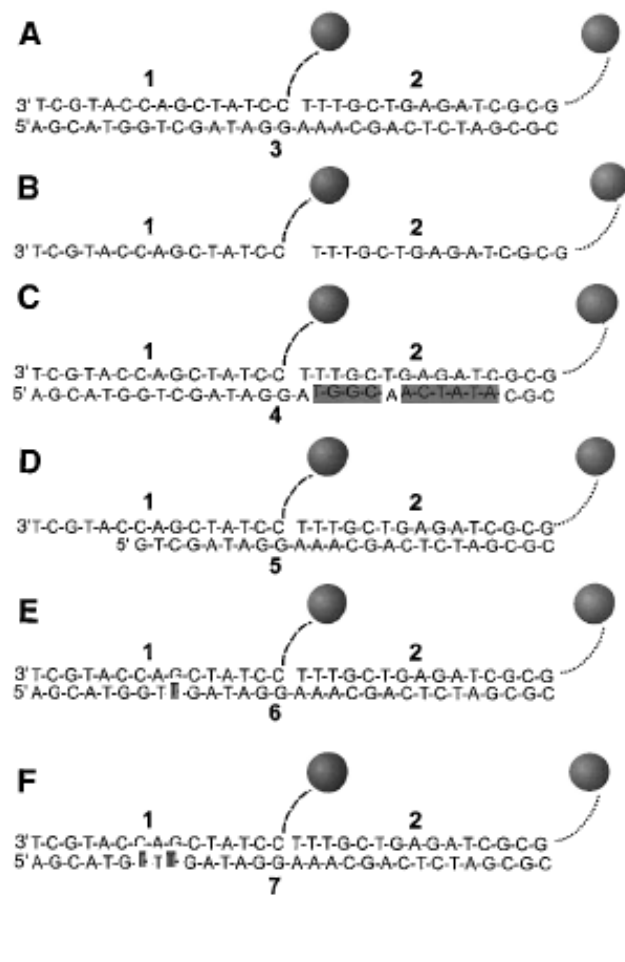


Fig. 2. Mercaptoalkyloligonucleotide-modified 13-nm Au particles and polynucleotide targets used for examining the selectivity of the nanoparticle-based colorimetric polynucleotide detection system. (A) Complementary target; (B) probes without the target; (C) a half-complementary target; (D) a 6-bp deletion; (E) a 1-bp mismatch; and (F) a 2-bp mismatch. For the sake of clarity, only two particles are shown; in reality a polymeric aggregate with many particles is formed. Dashed lines represent flexible spacer portions of the mercaptoalkyloligonucleotide strands bound to the nanoparticles; note that these spacers, because of their noncomplementary nature, do not participate in hybridization. The full sequences for the two probes, 1 and 2, which bind to targets 3 through 7, are

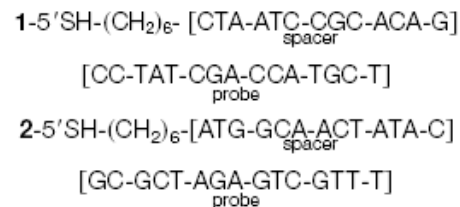
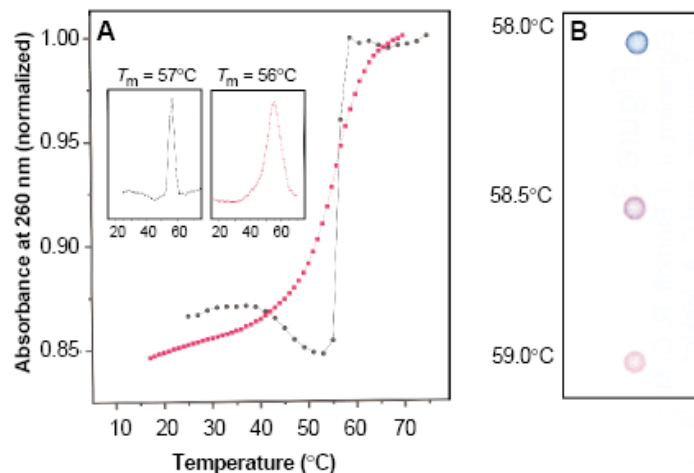


Fig. 3. (A) Comparison of the thermal dissociation curves for complexes of mercaptoalkyloligonucleotide-modified Au nanoparticles (black circles) and mercaptoalkyloligonucleotides without Au nanoparticles (red squares) with the complementary target, **3**, in hybridization buffer (0.1 M NaCl, 10 mM phosphate buffer, pH 7.0). For the first set (black circles), a mixture of 150 μl of each colloid conjugate and 3 μl of the target oligonucleotide in hybridization buffer (0.1 M



NaCl, 10 mM phosphate, pH 7.0) was frozen at the temperature of dry ice, kept for 5 min, thawed over a period of 15 min, and diluted to 1.0 ml with buffer (final target concentration, 0.02 μM). The absorbance was measured at 1-min intervals with a temperature increase of 1°C per minute. The increase in absorption at 260 nm (A_{260}) was ~ 0.3 absorption units (AU). In the absence of the oligonucleotide targets, the absorbance of the nanoparticles did not increase with increasing temperature. For the second set, the mercaptoalkyloligonucleotides and complementary target (each 0.33 μM) were equilibrated at room temperature in 1 ml of buffer, and the changes in absorbance with temperature were monitored as before. The increase in A_{260} was 0.08 AU. **(Insets)** Derivative curves for each set (15). **(B)** Spot test showing T_c (thermal transition associated with the color change) for the Au nanoparticle probes hybridized with complementary target. A solution prepared from 150 μl of each probe and 3 μl of the target (0.06 μM final target concentration) was frozen for 5 min, allowed to thaw for 10 min, transferred to a 1-ml cuvette, and warmed at 58°C for 5 min in the thermally regulated cuvette chamber of the spectrophotometer. Samples (3 μl) were transferred to a C_{18} reverse phase plate with an Eppendorf pipette as the temperature of the solution was increased incrementally 0.5°C at 5-min intervals.

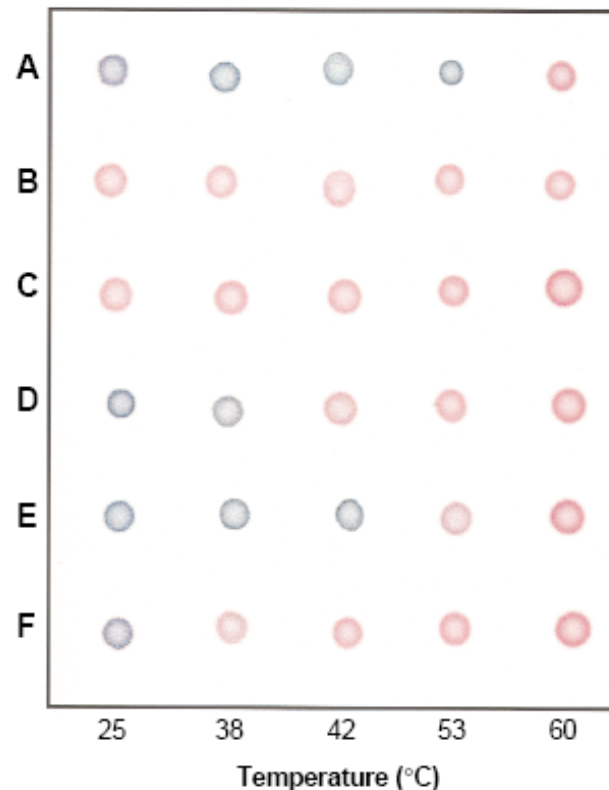
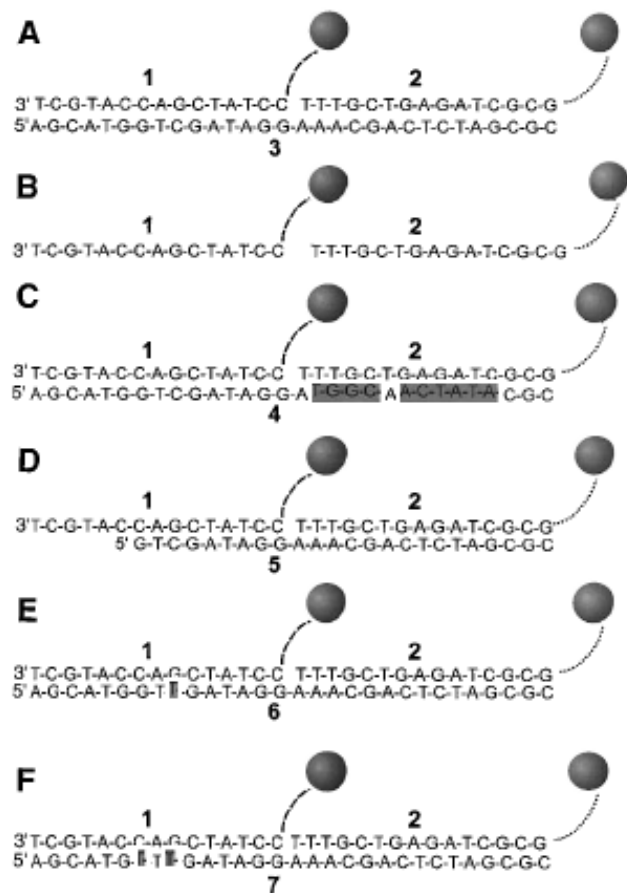


Fig. 4. Selective polynucleotide detection for the target probes shown in Fig. 2: **(A)** complementary target; **(B)** no target; **(C)** complementary to one probe; **(D)** a 6-bp deletion; **(E)** a 1-bp mismatch; and **(F)** a 2-bp mismatch. Nanoparticle aggregates were prepared in a 600- μ l thin-walled Eppendorf tube by addition of 1 μ l of a 6.6 μ M oligonucleotide target to a mixture containing 50 μ l of each probe (0.06 μ M final target concentration). The mixture was frozen (5 min) in a bath of dry ice and isopropyl alcohol and allowed to warm to room temperature. Samples were then transferred to a temperature-controlled water bath, and 3- μ l aliquots were removed at the indicated temperatures and spotted on a C_{18} reverse phase plate.

Colloidal Au-Enhanced Surface Plasmon Resonance for Ultrasensitive Detection of DNA Hybridization

Lin He, Michael D. Musick, Sheila R. Nicewarner, Frank G. Salinas, Stephen J. Benkovic, Michael J. Natan, and Christine D. Keating*

Scheme 1. SPR Surface Assembly

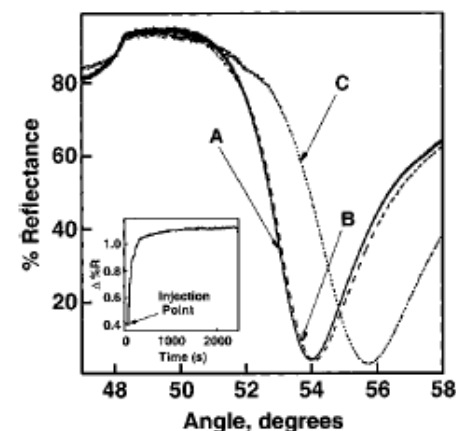
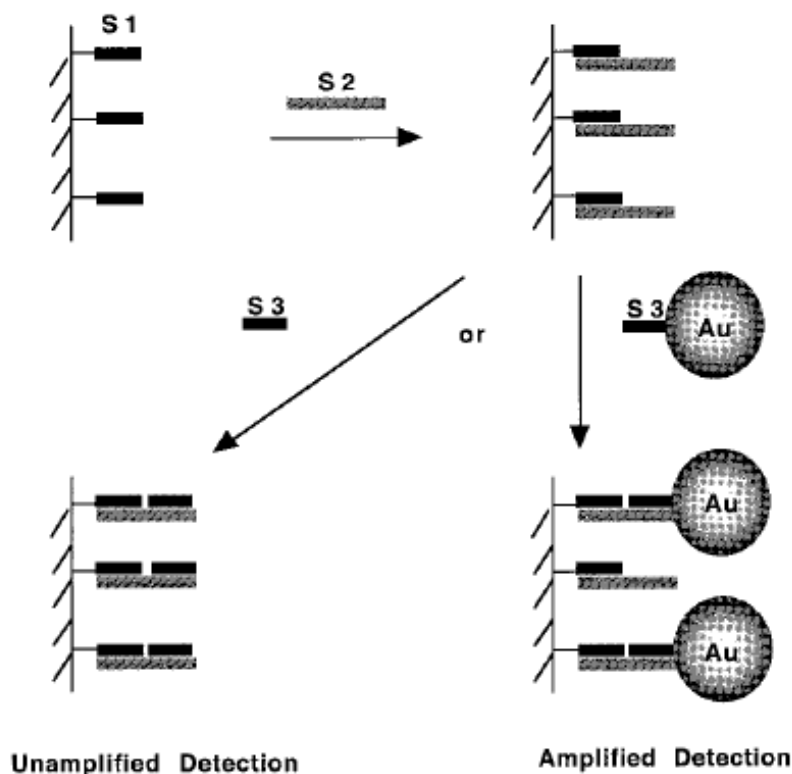


Figure 1. SPR curves of surfaces prepared in sequential steps as illustrated in Scheme 1: a MHA-coated Au film modified with a 12-mer oligonucleotide S1(A), after hybridization with its complementary 24-mer target S2 (B), and followed by introduction of S3: Au conjugate (C) to the surface. Inset: surface plasmon reflectance changes at 53.2° for the oligonucleotide-coated Au film measured during a 60-min exposure to S3: Au conjugates.

Scheme 2. SPR Surface Assembly in the Digestion Experiment

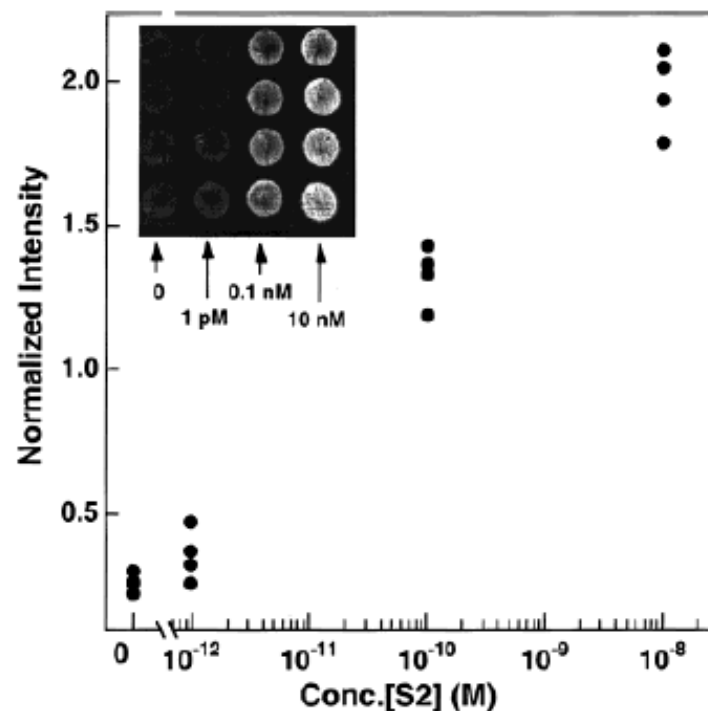
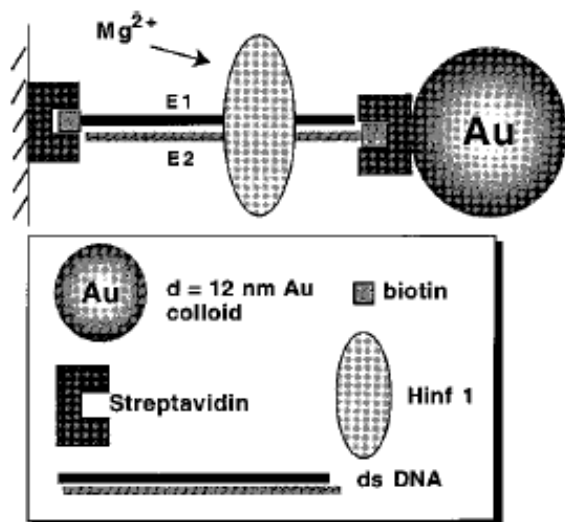


Figure 5. Plot of normalized intensity of SPR reflectance as a function of logarithmic concentration of the analyte 24-mer oligo (S2). Each spot represents one data point at the corresponding concentration. CCD parameters: exposure time = 0.3 s, 16 bit resolution, spot size = 4.5 mm in diameter. Inset: a 2-D SPR image of a Au surface derivatized with 20 μL of buffer blank, 1 pM, 0.1 nM, and 10 nM S2 oligos (from left to right, respectively).

Self-Assembled Nanoparticle Probes for Recognition and Detection of Biomolecules

Dustin J. Maxwell, Jason R. Taylor, and Shuming Nie^{*,†}

9606 ■ J. AM. CHEM. SOC. 2002, 124, 9606–9612

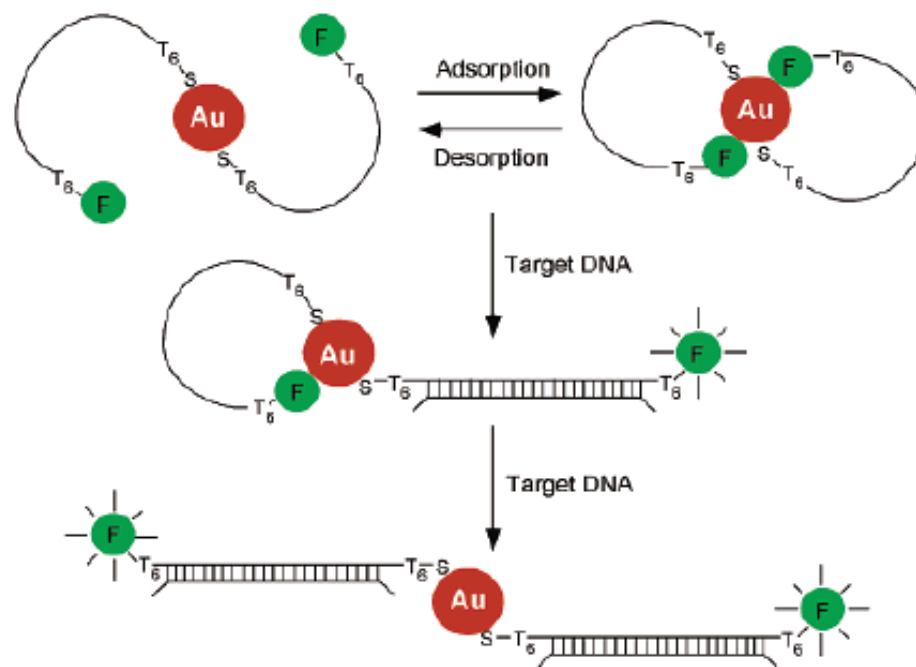


Figure 1. Nanoparticle-based probes and their operating principles. Two oligonucleotide molecules (oligos) are shown to self-assemble into a constrained conformation on each gold particle (2.5 nm diameter). A T₆ spacer (six thymines) is inserted at both the 3'- and 5'-ends to reduce steric hindrance. Single-stranded DNA is represented by a single line and double-stranded DNA by a cross-linked double line. In the assembled (closed) state, the fluorophore is quenched by the nanoparticle. Upon target binding, the constrained conformation opens, the fluorophore leaves the surface because of the structural rigidity of the hybridized DNA (double-stranded), and fluorescence is restored. In the open state, the fluorophore is separated from the particle surface by about 10 nm. See text for detailed explanation. Au, gold particle; F, fluorophore; S, sulfur atom.

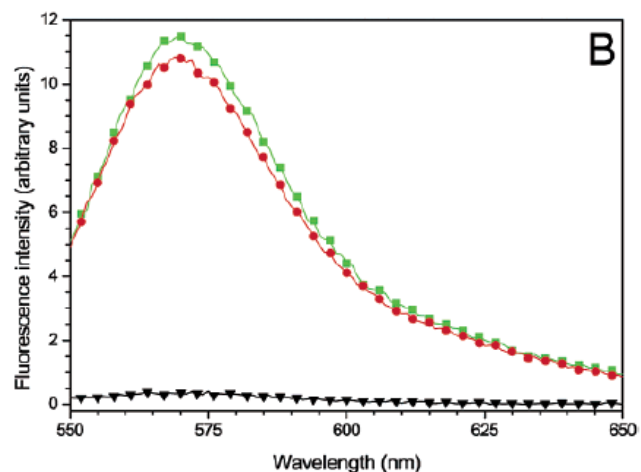
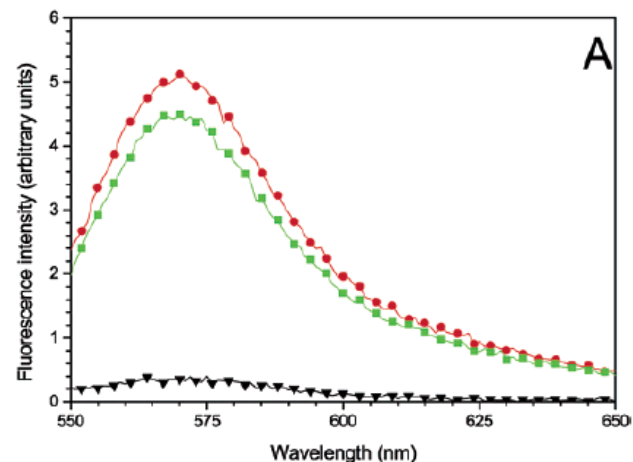


Figure 5. Fluorescence responses and the lack of sequence recognition abilities observed for nonthiolated nanoparticle probes. (A) Fluorescence spectra of nonthiolated probes generated by a complementary target (red curve), a noncomplementary target (green curve), and no target (black curve). These probes are considered nonfunctional because they do not recognize specific DNA sequences. (B) Fluorescence signals obtained from the supernatant solution when the probes were treated with a complementary target (red curve) or a noncomplementary target (green curve). The result revealed that the oligos were released into solution by nonspecific adsorption of the target on the particle surface. With a thiol group, this release was not observed (little or no signal in solution, black curve in B). The nonfunctional probes were prepared in the same way as the functional probes, except that the 3'-end thiol group was deleted. The intensity differences for the red and green curves were within experimental errors and had no particular significance.

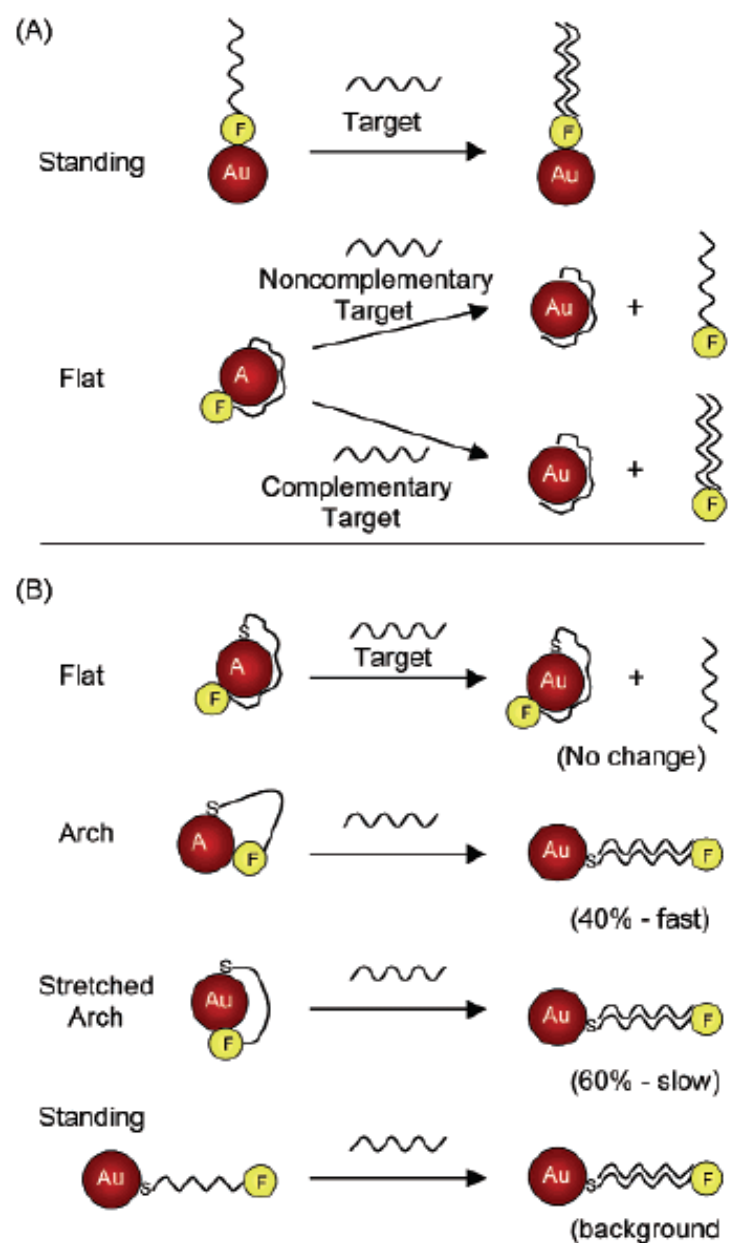
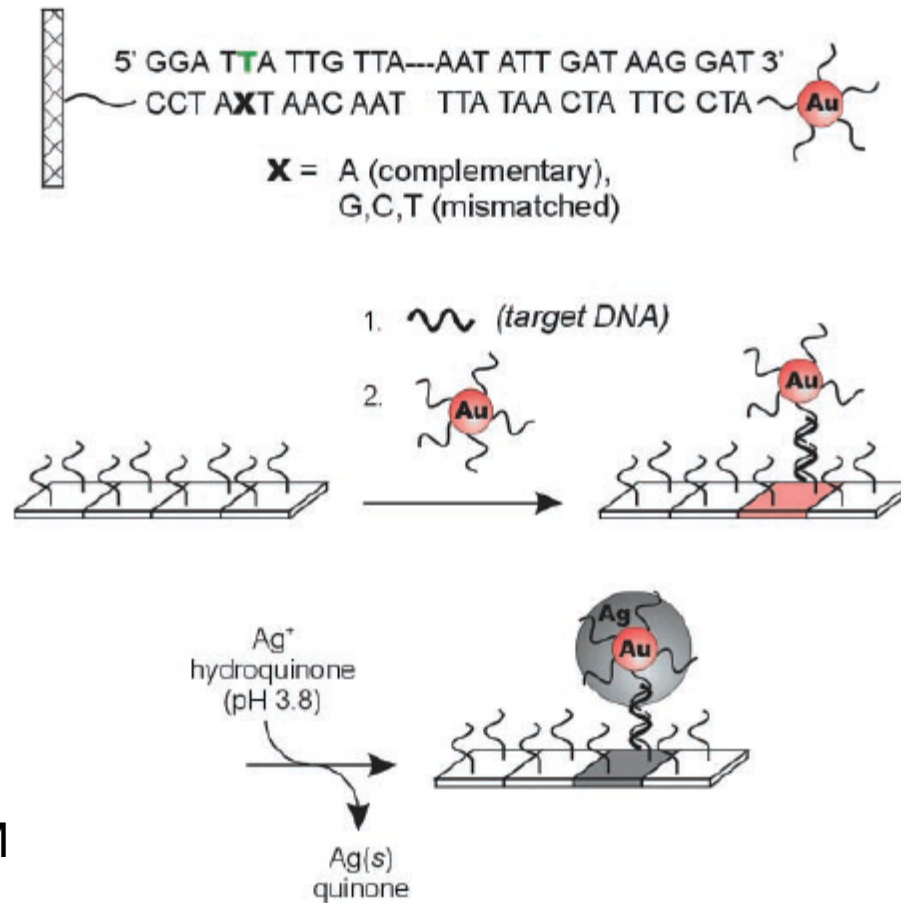


Figure 6. Schematic illustration of possible configurations for (a) nonthiolated and (b) thiolated oligonucleotides adsorbed on colloidal gold nanocrystals. Detailed discussion in text.

Scanometric DNA Array Detection with Nanoparticle Probes

SCIENCE VOL 289 8 SEPTEMBER 2000

T. Andrew Taton,^{1,2} Chad A. Mirkin,^{1,2*} Robert L. Letsinger^{1*}



50 fM => 0.2 fM

Fig. 1. Images of 7 mm by 13 mm, oligonucleotide-functionalized, float glass slides, obtained with a flatbed scanner. **(A)** Slide before hybridization of target and nanoparticle probe. **(B)** A slide identical to **(A)** after hybridization with oligonucleotide target (10 nM) and then nanoparticle probes (5 nM in particles). The pink color derives from the Au nanoparticle probes. **(C)** A slide identical to **(B)** after exposure to silver amplification solution for 5 min. **(D)** Slide before hybridization of target and nanoparticle probe. **(E)** A slide identical to **(D)** after hybridization with target (100 pM) and then nanoparticle probe (5 nM). The extinction of the submonolayer of nanoparticles is too low to be observed visually or with a flatbed scanner. **(F)** A slide identical to **(E)** after exposure to silver amplification solution for 5 min. Slide **(F)** is lighter than slide **(C)**, indicating a lower concentration of target. **(G)** A control slide exposed to 5 nM nanoparticle probe and then exposed to silver amplification solution for 5 min. No darkening of the slide is observed. **(H)** Graph of 8-bit gray scale values as a function of target concentration. The gray scale values were taken from flatbed scanner images of oligonucleotide-functionalized glass surfaces that had been exposed to varying concentrations of oligonucleotide target, labeled with 5 nM oligonucleotide probe and immersed in silver amplification solution. For any given amplification time, the grayscale range is limited by surface saturation at high grayscale values and the sensitivity of the scanner at low values. Therefore, the dynamic range of this system can be adjusted by means of hybridization and amplification conditions (that is, lower target concentrations require longer amplification periods). Squares: 18-base capture-target overlap (5), 8× PBS hybridization buffer [1.2 M NaCl and 10 mM NaH₂PO₄/Na₂HPO₄ buffer (pH 7)], 15 min amplification time. Circles: 12-base capture-target overlap, 8× PBS hybridization buffer, 10 min amplification time. Triangles: 12-base capture-target overlap, 2× PBS hybridization buffer [0.3 M NaCl, 10 mM NaH₂PO₄/Na₂HPO₄ buffer (pH 7)], 5 min amplification time. The lowest target concentration that can be effectively distinguished from the background baseline is 50 fM.

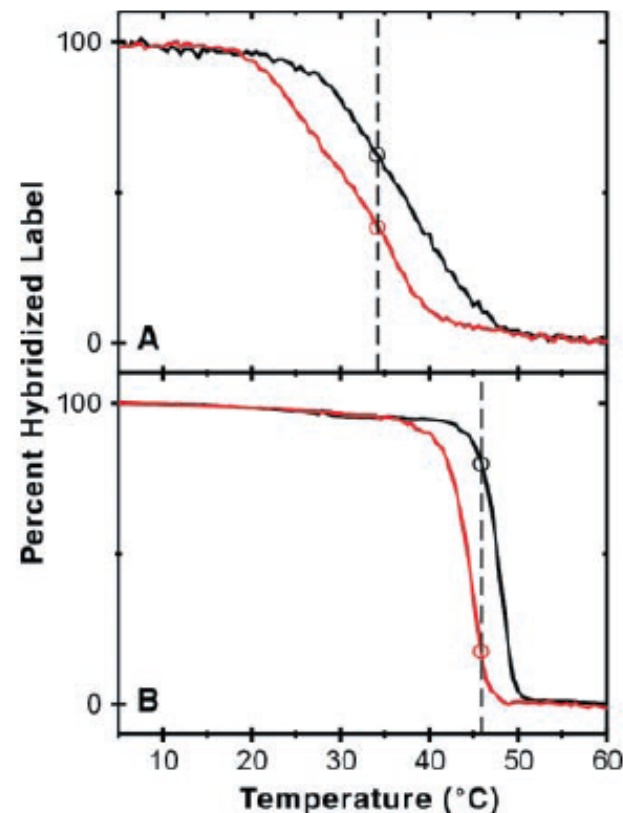
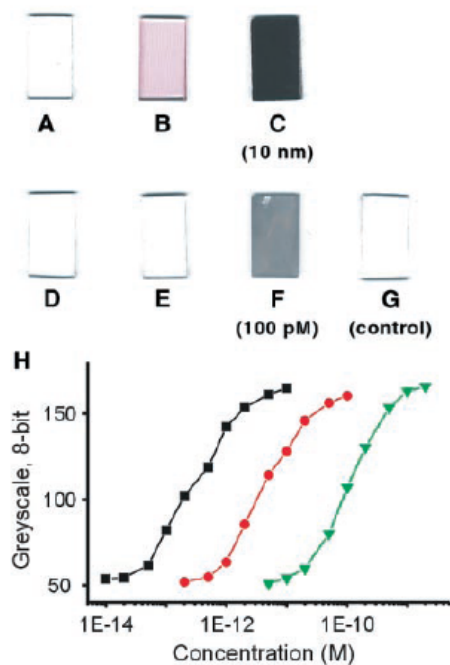
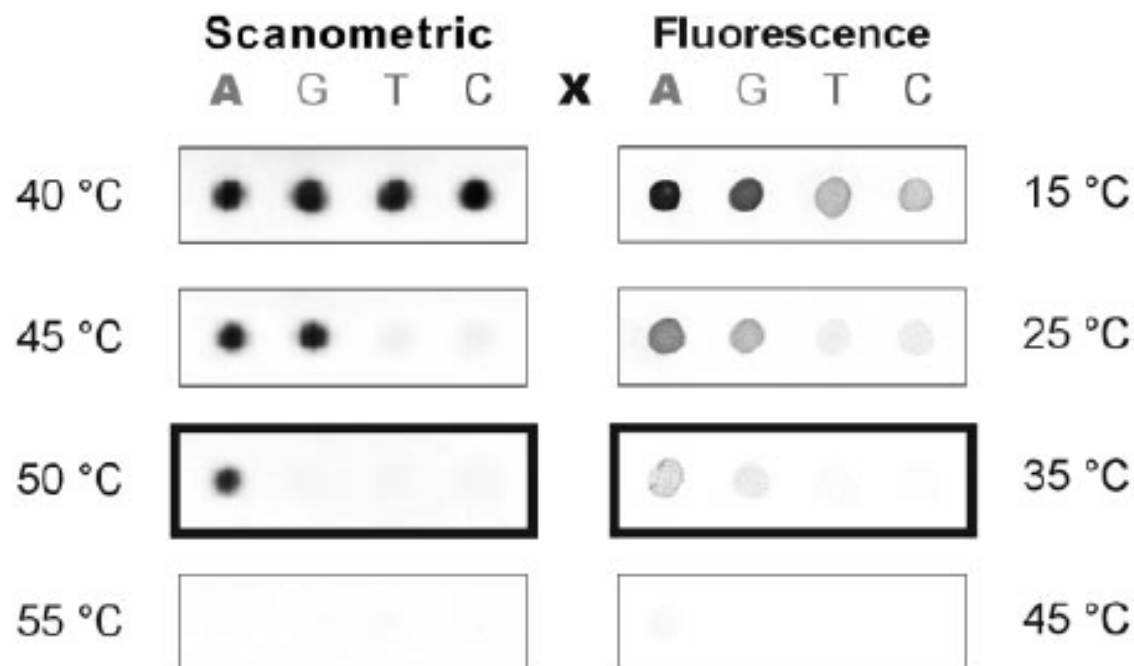


Fig. 3. (Left) Nanoparticle-labeled arrays developed at different stringency temperatures. Model oligonucleotide arrays (with the capture sequences shown in Scheme 1) were treated with oligonucleotide target and nanoparticle probes, followed by a 2-min buffer wash at the temperatures shown and subsequent silver amplification (13). Images were obtained

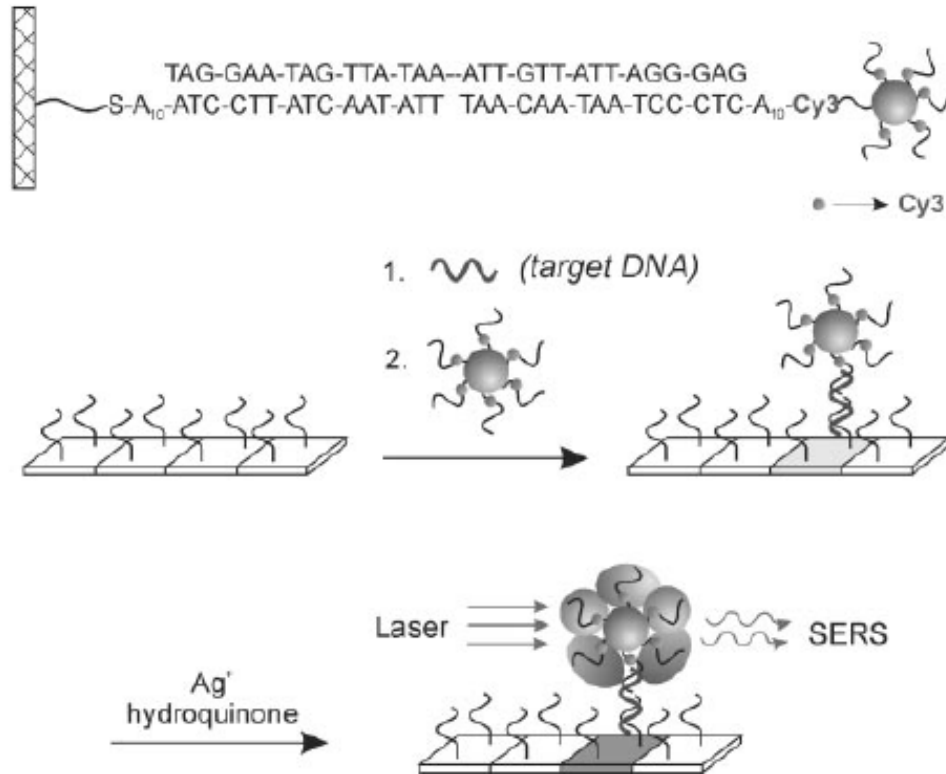


with an Epson Expression 636 (600 dots per inch) flatbed scanner (Epson America, Long Beach, California). The darkened border indicates the array that showed optimum selectivity for the perfectly complementary target; at this temperature, the ratio of background-subtracted, 8-bit gray scale values for elements A:G:T:C, obtained from histogram averages in Adobe Photoshop (Adobe Systems, San Jose, California), is 96:9:7:6. **(Right)** Fluorophore-labeled arrays washed at different stringency temperatures. Model oligonucleotide arrays identical to those shown at left were treated with oligonucleotide target and Cy3-labeled oligonucleotide probes, followed by a 2-min buffer wash at the temperatures shown. Images were obtained with a ScanArray Confocal Microarray Scanner (GSI Lumonics, Billerica, Massachusetts). The darkened border indicates the array that showed the highest selectivity for the perfectly complementary target, as calculated by the QuantArray Analysis software package (GSI Lumonics); at this temperature, the intensity ratio (in percent, with the intensity of the X = A element at 15°C set to 100%) for elements A:G:T:C is 18:7:1:1.

Nanoparticles with Raman Spectroscopic Fingerprints for DNA and RNA Detection

YunWei Charles Cao, Rongchao Jin, Chad A. Mirkin*

30 AUGUST 2002 VOL 297 SCIENCE



1 fM

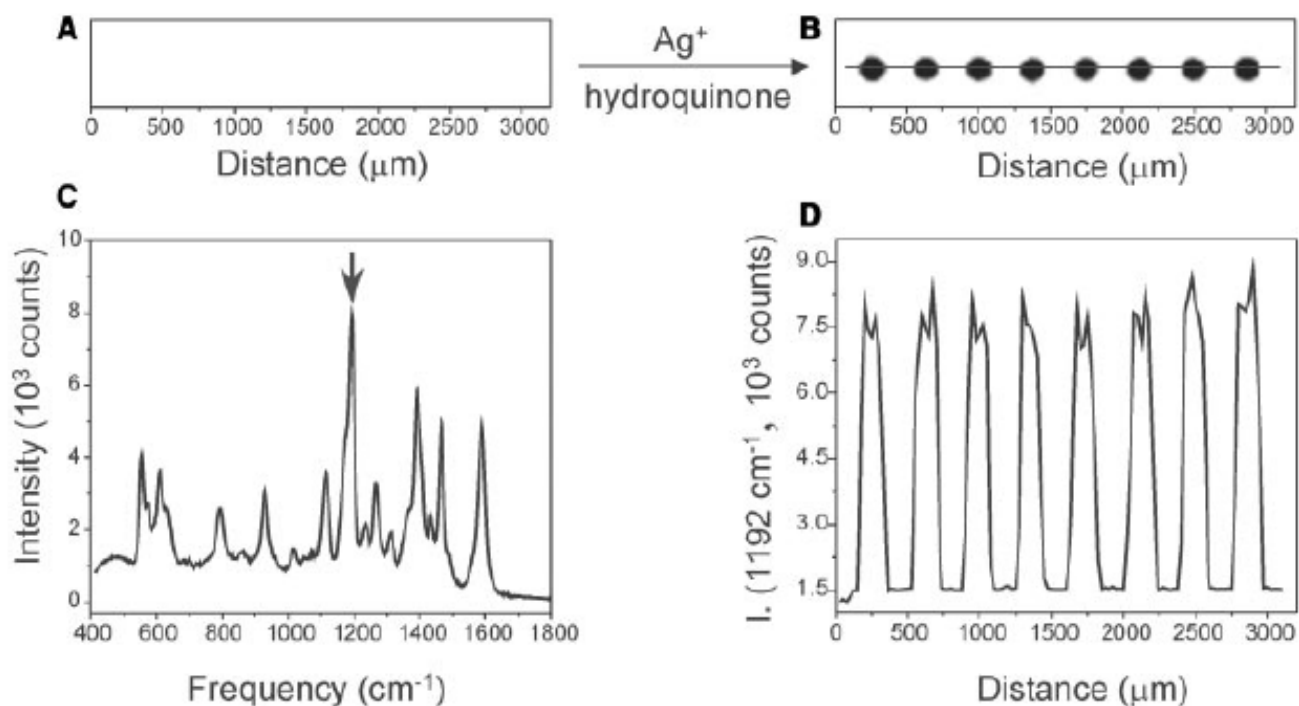


Fig. 1. Flatbed scanner images of microarrays hybridized with nanoparticles (A) before and (B) after Ag enhancement. (C) A typical Raman spectrum acquired from one of the Ag spots. (D) A profile of Raman intensity at 1192 cm⁻¹ as a function of position on the chip; the laser beam from the Raman instrument is moved over the chip from left to right as defined by the line in (B).

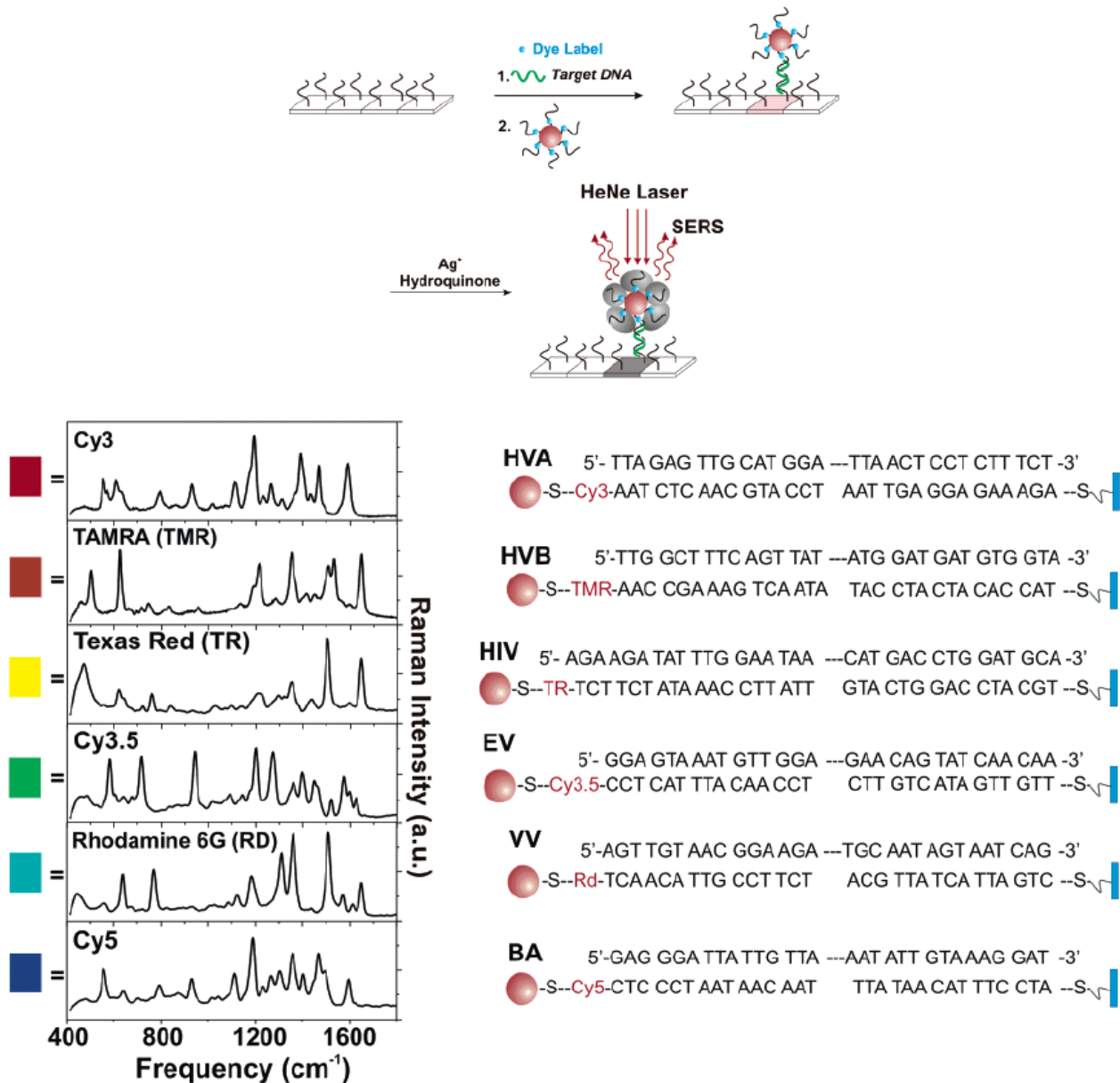


Figure 5. If Raman dyes (blue spheres) are attached to the labeling probe in the scanometric assay, the targets can be encoded and detected via the Raman signal of their labels. (Reprinted with permission from *Science* (<http://www.aaas.org>), ref 68. Copyright 2002 American Association for the Advancement of Science.)

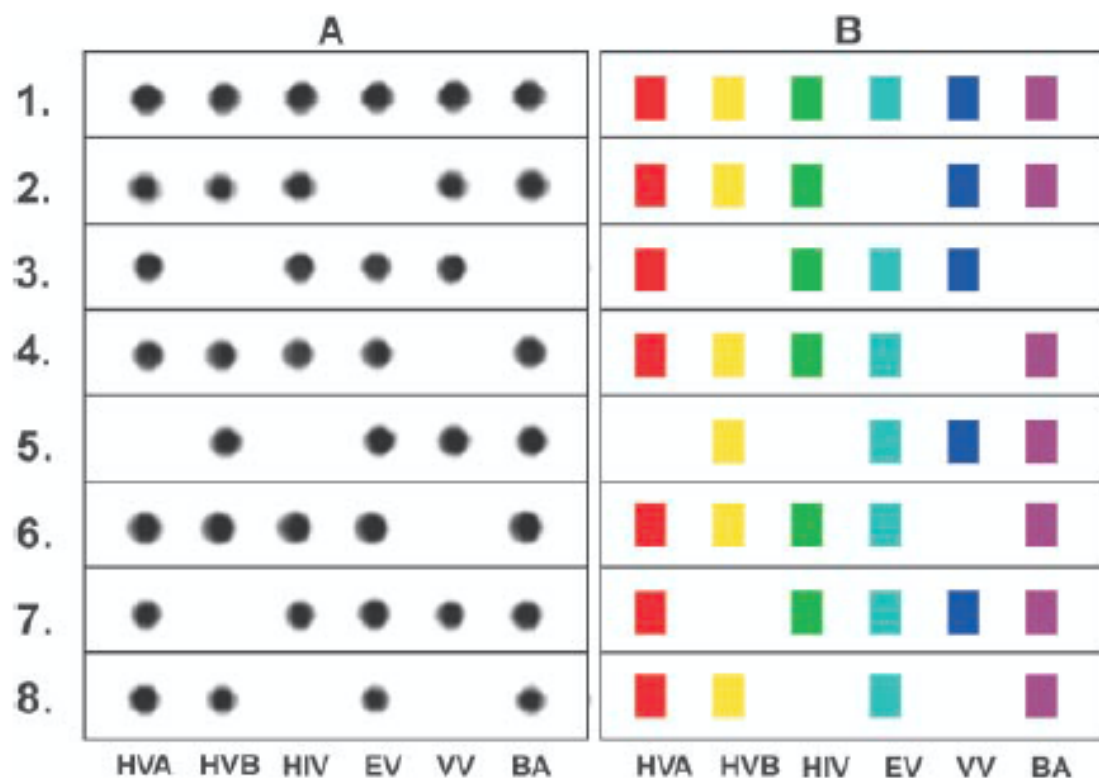


Fig. 3. (A) Flatbed scanner images of Ag-enhanced microarrays and (B) corresponding Raman spectra. The colored boxes correlate with the color-coded Raman spectra in Fig. 2. No false-positives or false-negatives were observed.

Bio-Bar-Code-Based DNA Detection with PCR-like Sensitivity

Jwa-Min Nam, Savka I. Stoeva, and Chad A. Mirkin*

J. AM. CHEM. SOC. 2004, 126, 5932–5933

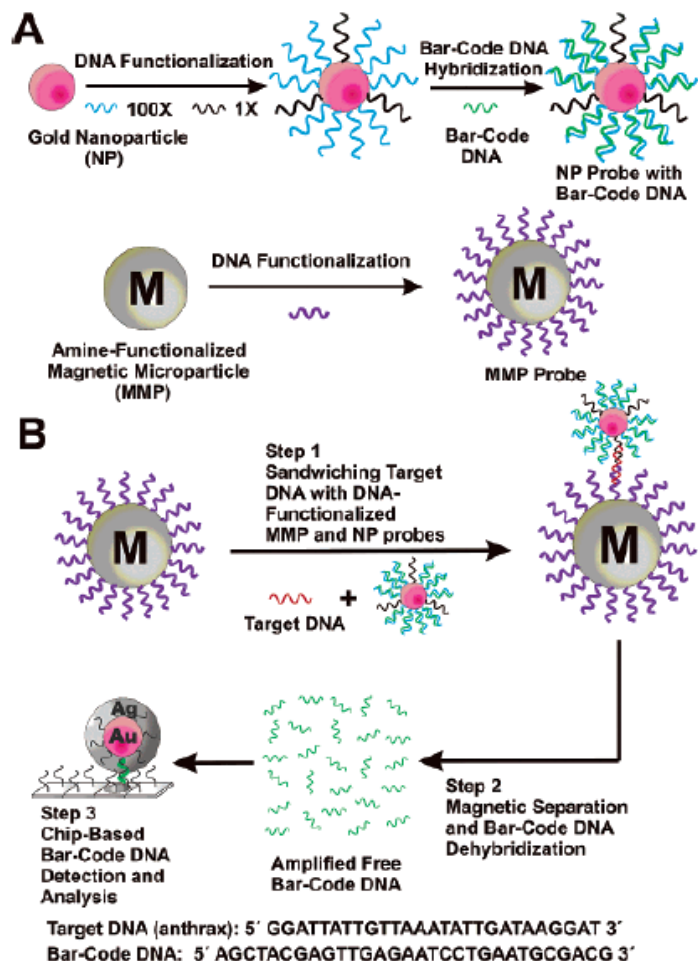


Figure 1. The DNA-BCA assay. (A) Nanoparticle and magnetic micro-particle probe preparation. (B) Nanoparticle-based PCR-less DNA amplification scheme.

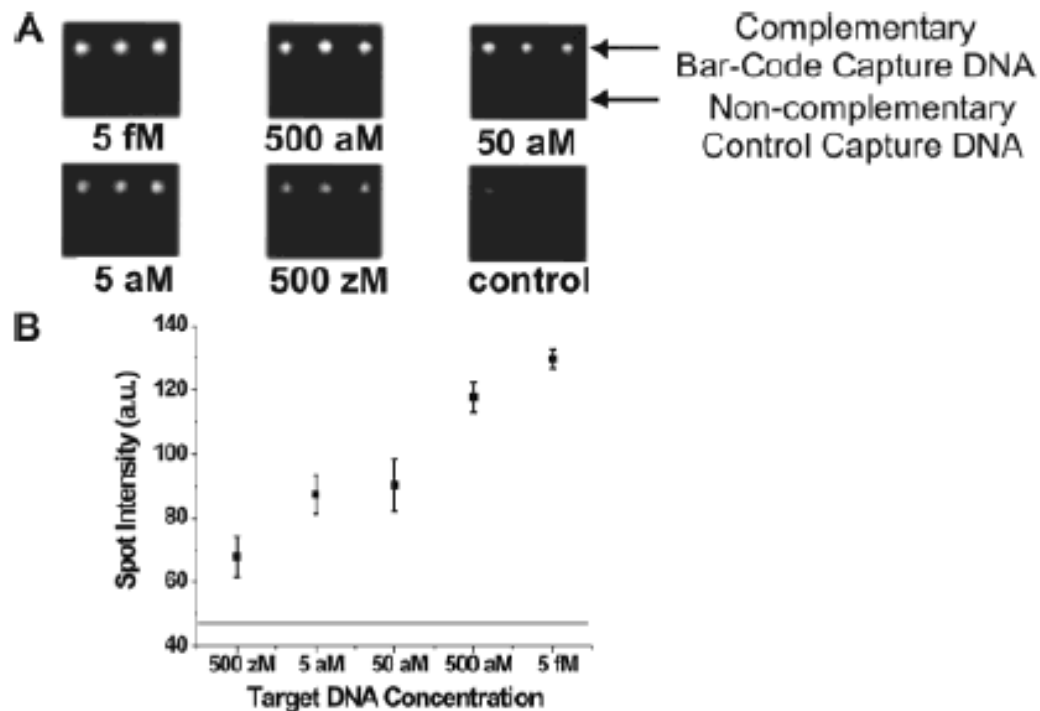


Figure 2. Amplified anthrax bar-code DNA detection with the Verigene ID system. (A) Anthrax bar-code DNA detection with 30 nm NP probes. (B) Quantitative data of spot intensities with 30 nm NP probes (Adobe Photoshop, Adobe Systems, Inc., San Jose, CA). The horizontal line represents control signal intensity (47 ± 2).



Figure 3. Single base mismatch experiment.

Nanoparticle-Based Bio-Bar Codes for the Ultrasensitive Detection of Proteins

26 SEPTEMBER 2003 VOL 301 SCIENCE

Jwa-Min Nam,* C. Shad Thaxton,* Chad A. Mirkin†

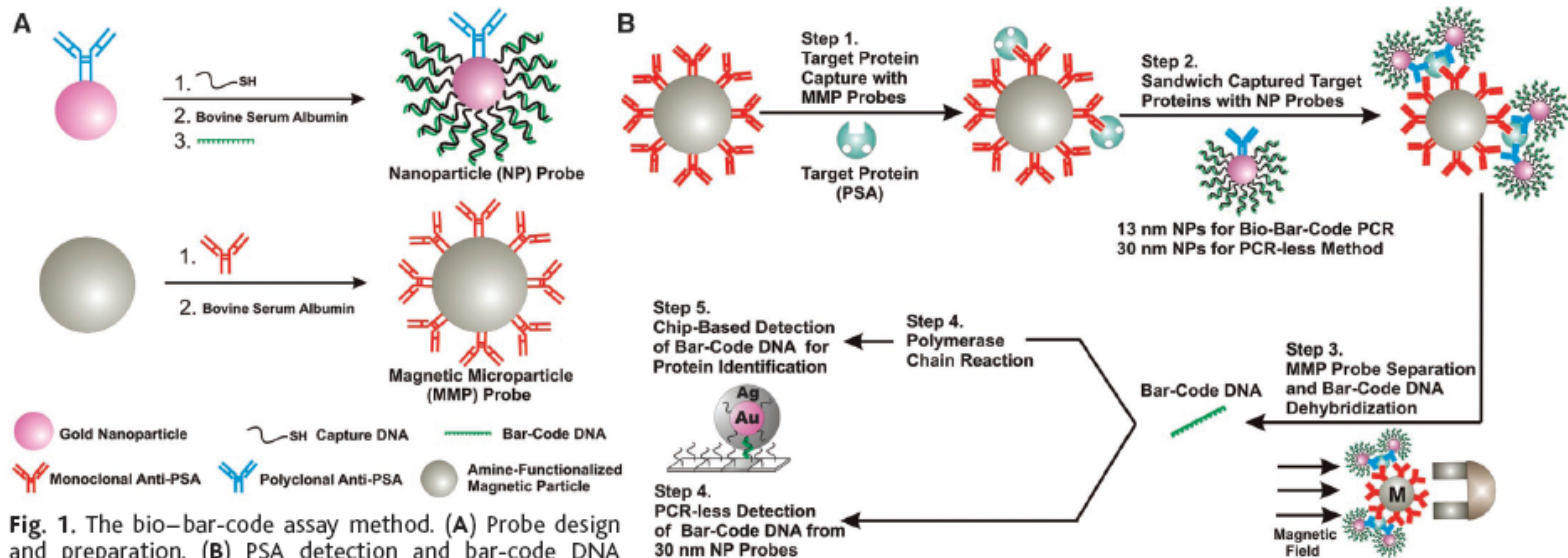


Fig. 1. The bio-bar-code assay method. (A) Probe design and preparation. (B) PSA detection and bar-code DNA amplification and identification. In a typical PSA-detection experiment, an aqueous dispersion of MMP probes functionalized with mAbs to PSA (50 μ l of 3 mg/ml magnetic probe solution) was mixed with an aqueous solution of free PSA (10 μ l of PSA) and stirred at 37°C for 30 min (Step 1). A 1.5-ml tube containing the assay solution was placed in a BioMag microcentrifuge tube separator (Polysciences, Incorporated, Warrington, PA) at room temperature. After 15 s, the MMP-PSA hybrids were concentrated on the wall of the tube. The supernatant (solution of unbound PSA molecules) was removed, and the MMPs were resuspended in 50 μ l of 0.1 M phosphate-buffered saline (PBS) (repeated twice). The NP probes (for 13-nm NP probes, 50 μ l at 1 nM; for 30-nm NP probes, 50 μ l at 200 pM), functionalized with polyclonal Abs to PSA and hybridized bar-code DNA strands, were then added to the assay solution. The NPs reacted with the PSA immobilized on the MMPs and provided DNA strands for signal amplification and protein identification (Step 2). This solution was vigorously stirred at 37°C for 30 min. The MMPs were then washed with 0.1 M PBS with the magnetic separator to isolate the mag-

netic particles. This step was repeated four times, each time for 1 min, to remove everything but the MMPs (along with the PSA-bound NP probes). After the final wash step, the MMP probes were resuspended in NANOpure water (50 μ l) for 2 min to dehybridize bar-code DNA strands from the nanoparticle probe surface. Dehybridized bar-code DNA was then easily separated and collected from the probes with the use of the magnetic separator (Step 3). For bar-code DNA amplification (Step 4), isolated bar-code DNA was added to a PCR reaction mixture (20- μ l final volume) containing the appropriate primers, and the solution was then thermally cycled (20). The bar-code DNA amplicon was stained with ethidium bromide and mixed with gel-loading dye (20). Gel electrophoresis or scanometric DNA detection (24) was then performed to determine whether amplification had taken place. Primer amplification was ruled out with appropriate control experiments (20). Notice that the number of bound NP probes for each PSA is unknown and will depend upon target protein concentration.

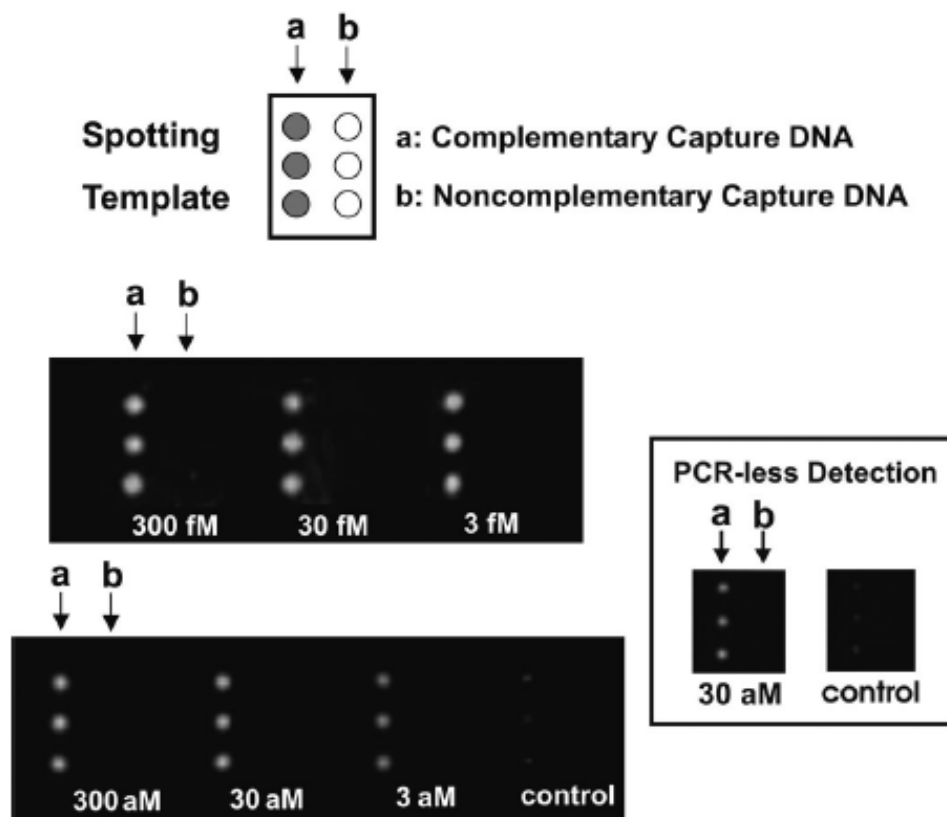


Fig. 2. Scanometric detection of PSA-specific bar-code DNA. PSA concentration (sample volume of 10 μ l) was varied from 300 fM to 3 aM and a negative control sample where no PSA was added (control) is shown. For all seven samples, 2 μ l of antidi-nitrophenyl (10 pM) and 2 μ l of β -galactosidase (10 pM) were added as background proteins. Also shown is PCR-less detection of PSA (30 aM and control) with 30 nm NP probes (inset). Chips were imaged with the Verigene ID system (20).

Table 1. Detection Limits of Nucleic Acid Assays^a

	assay	ss DNA	PCR products	genomic DNA
nanostructure-based methods	colorimetric ²⁹ (cross-linked Au nanoparticles)	~10 nM		
	colorimetric ³⁶ (non-cross-linked Au nanoparticles)	60 nM		
	magnetic relaxation ⁹⁷ (iron oxide nanoparticles)	20 pM		
	electrochemical ⁹⁶ (nanoparticles)	270 pM		
	scanometric ^{35,66,67} (Au nanoparticles with Ag amplification)	50 fM	100 aM ^b	200 fM
	Raman spectroscopy ⁶⁸ (Au nanoparticles with Ag amplification)	~1 fM		
	electrical ⁹³ (Au nanoparticles with Ag amplification)	500 fM		
	electrical ⁹⁹ (Si nanowire)	10 fM		
	electrical ¹⁰³ (carbon nanotube)	54 aM		
	resonant light-scattering ⁶¹⁻⁶⁶ (metal nanoparticles)	170 fM ^b		33 fM
	fluorescence ⁵⁶ (ZnS and CdSe quantum dots)	2 nM		
	surface plasmon resonance ⁴¹ (Au nanoparticles)	10 pM		
	quartz crystal microbalance ⁹⁴ (Au nanoparticles)	~1 fM		
	laser diffraction ⁴² (Au nanoparticles)	~50 fM		
	fluorescence ⁴⁵ (fluorescent nanoparticles)	~1 fM		
other non-enzymatic based methods	bio-bar-code amplification ⁷¹ (Au nanoparticles with Ag amplification)	500 zM		
	fluorescence ³⁵ (molecular fluorophores)		~600 fM ^b	
	fluorescence (dendrimer amplification) ¹³⁴		2.5 μ g	
	electrochemical amplification ¹³⁶ (electroactive reporter molecules)	100 aM		

^a Detection limits can vary based on target length and sequence; therefore, it is difficult to compare assays without testing them using identical targets and conditions. ^b Values taken from ref 34.

Table 2. Detection Limits of Protein Assays

	assay	target	protein in saline	protein in serum
nanostructure-based methods	optical ⁷² (Au nanoshells)	rabbit IgG	0.88 ng/mL (~4.4 pM) ^a	0.88 ng/mL (~4.4 pM) ^a
	optical ⁷⁴ (Au nanoparticles)	IgE and IgG1	~20 nM	
	magnetic relaxation ⁹⁸ (iron oxide nanoparticles)	adenovirus (ADV) and herpes simplex virus (HSV)	100 ADV/ 100 μ L	50 HSV/ 100 μ L
	scanometric ⁷⁹ (Au nanoparticles with Ag amplification)	mouse IgG	200 pM	
	Raman ⁸² (Au nanoparticles with Raman labels)	prostate-specific antigen		30 fM
	surface plasmon resonance ^{83,84} (triangular Ag particles on surfaces)	streptavidin(S A) and anti-biotin (AB)	~1 pM SA and ~700 pM AB	
	electrical ¹¹⁰ (single-walled carbon nanotubes)	10E3 antibody to U1A RNA splicing factor	~1 nM	
	electrical ²⁰ (Si nanowires)	streptavidin	10 pM	
molecular fluorophore methods	bio-bar-code amplification ⁷⁵ (Au nanoparticles with Ag amplification)	prostate-specific antigen	30 aM (3 aM) ^b	(30 aM) ^b
	enzyme-linked immunosorbent assay	various	pM range	pM range
electrochemical methods	electrochemical amplification ¹³⁷ (oligonucleotide reporter molecules)	IgG	13 fM	
enzyme-based amplification methods	immuno-PCR ⁷⁶	bovine serum albumin	2 fM	
	rolling circle amplification ⁷⁷	prostate-specific antigen	3 fM	

^a Reported in ng/mL; authors converted to molar concentration for ease of comparison. ^b These values are the lower limits when PCR is used to amplify the bar-code DNA prior to scanometric detection of bar codes.

Surface Plasmon

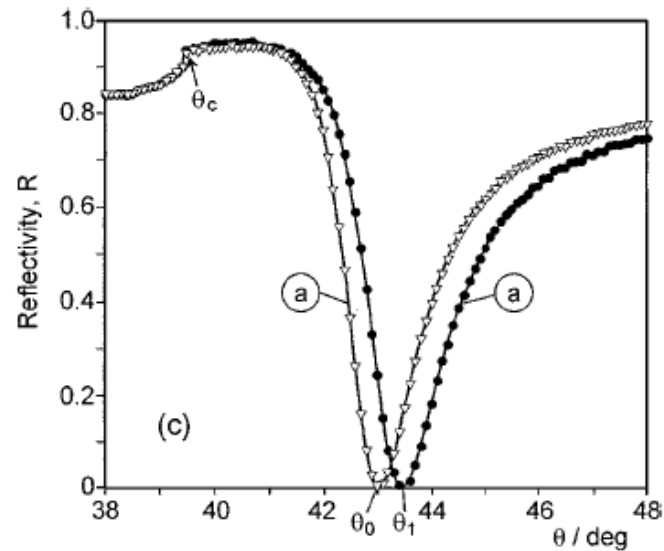
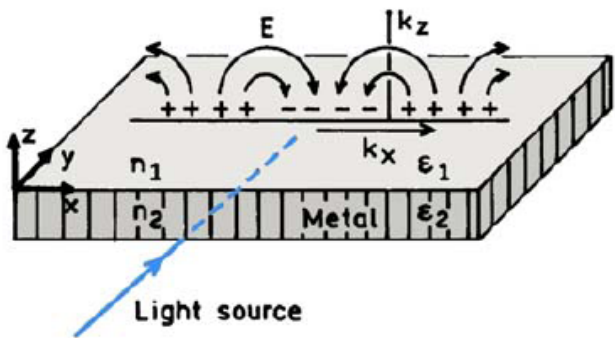
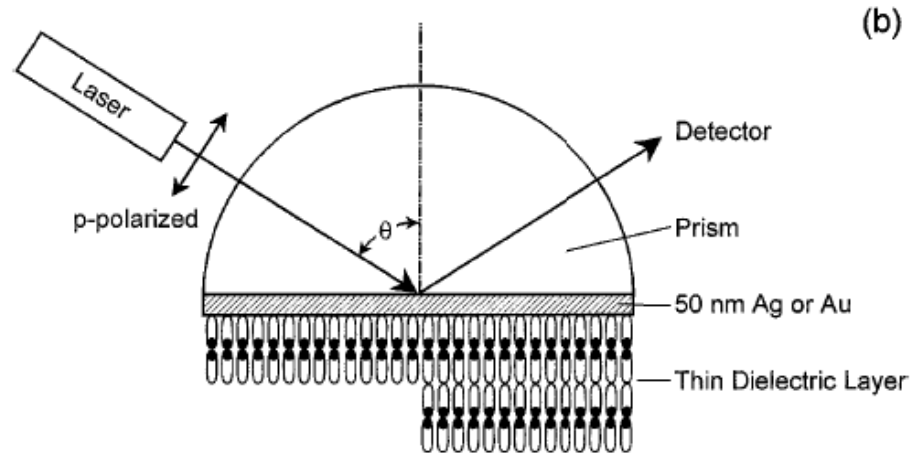
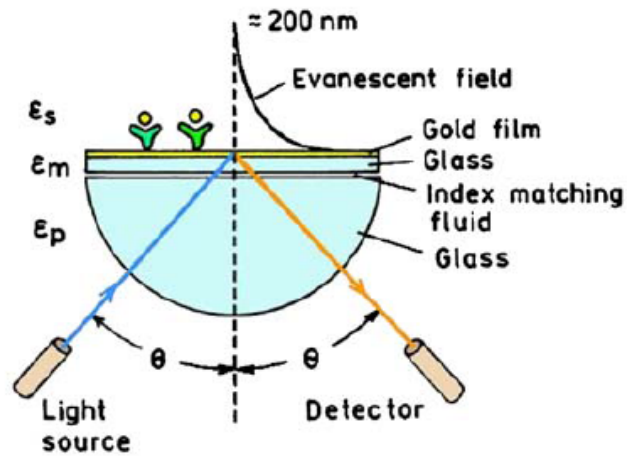
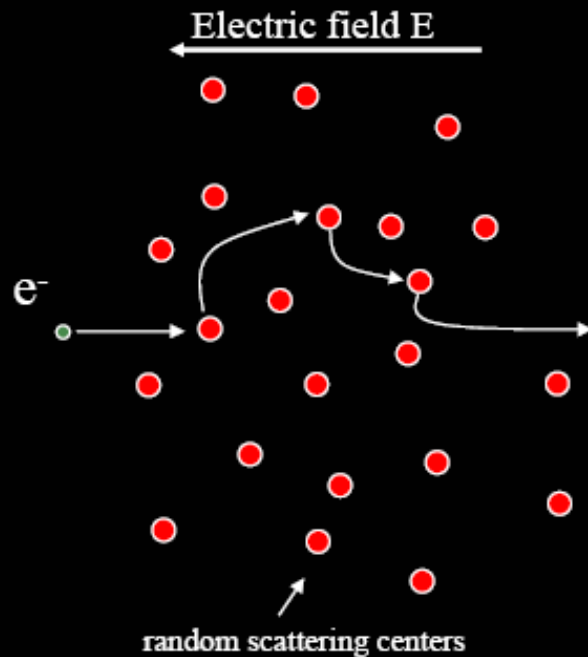


Figure 3. Schematics of an SPR experiment (top) and of the light-induced surface plasmons (bottom).

Drift: Drude model



$$F = ma$$

$$eE = m \frac{\partial v}{\partial t}$$

$$v_{avg} = \underbrace{\frac{e\tau}{m}}_{\mu} E$$

$$j = ne v_{avg} = \underbrace{\frac{ne^2\tau}{m}}_{\sigma} E$$

$$m \frac{\partial}{\partial t} \langle \vec{v} \rangle = q \vec{E} - \gamma \langle \vec{v} \rangle$$

$$\sigma(\omega) = \frac{\sigma_0}{1 + i\omega\tau}$$

AC Dielectric Response

$$\epsilon_m = 1 - \frac{\omega_p^2}{\omega^2} \quad \text{Plasma frequency}$$

polarizability of a small metal sphere with dielectric function $\epsilon(\lambda)$

$$\alpha = R^3 \frac{\epsilon - 1}{\epsilon + 2}.$$

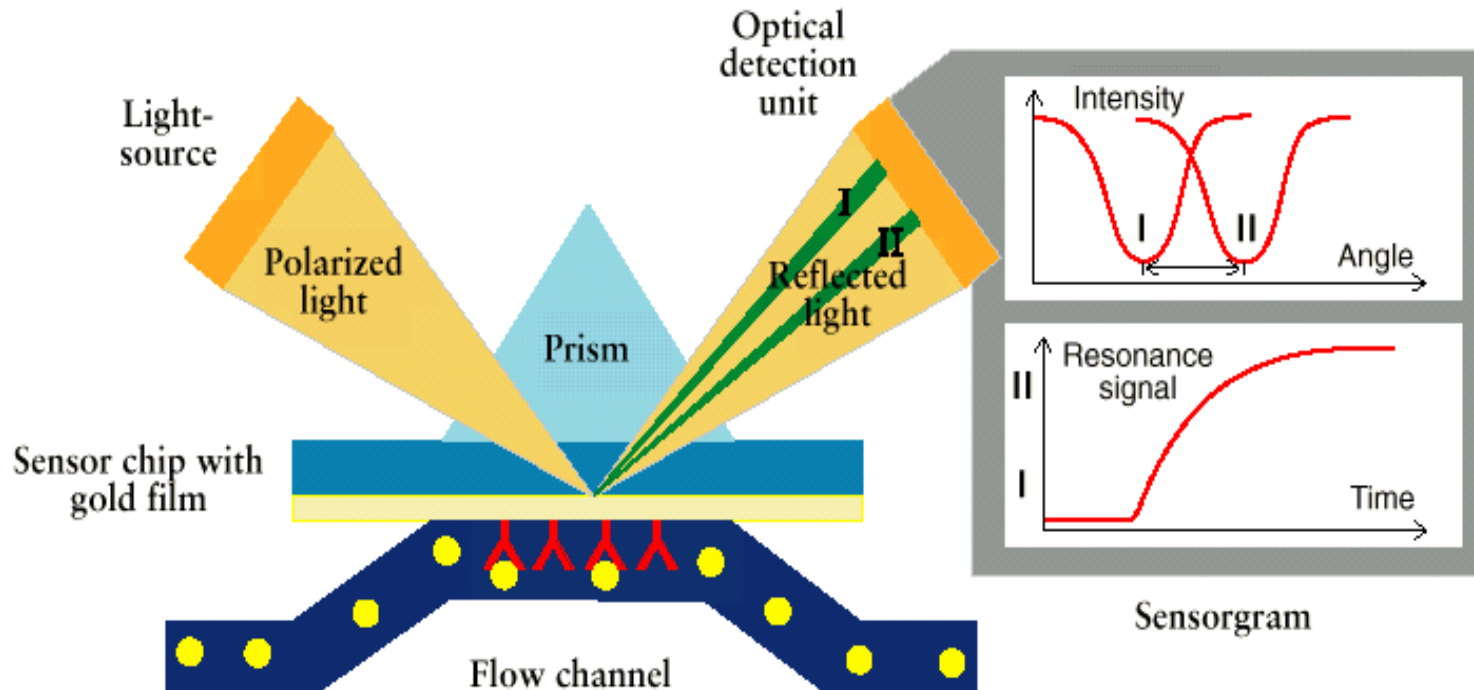
$$\epsilon = \epsilon_b + 1 - \frac{\omega_p^2}{\omega^2 + i\omega\gamma},$$

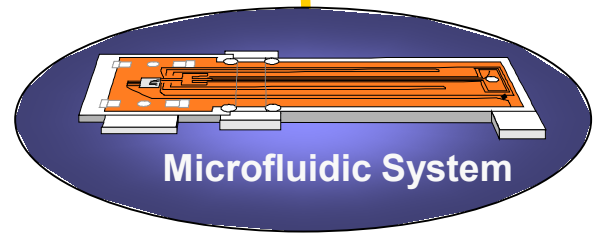
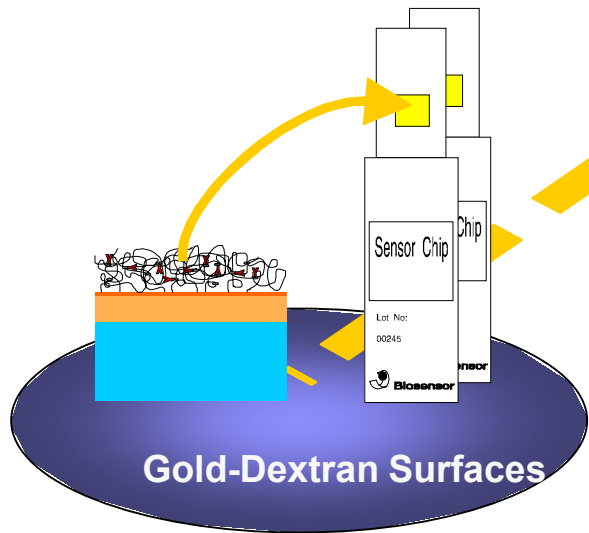
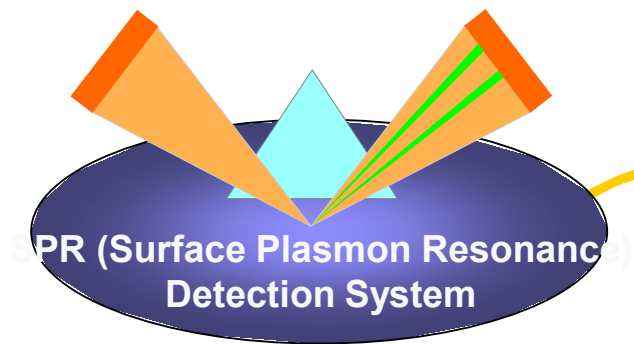
$$\alpha = \frac{R^3(\epsilon_b\omega^2 - \omega_p^2) + i\omega\gamma\epsilon_b}{[(\epsilon_b + 3)\omega^2 - \omega_p^2] + i\omega\gamma(\epsilon_b + 3)}.$$

$$\omega_R = \frac{\omega_p}{\sqrt{\epsilon_b + 3}} \quad \gamma(\epsilon_b + 3).$$

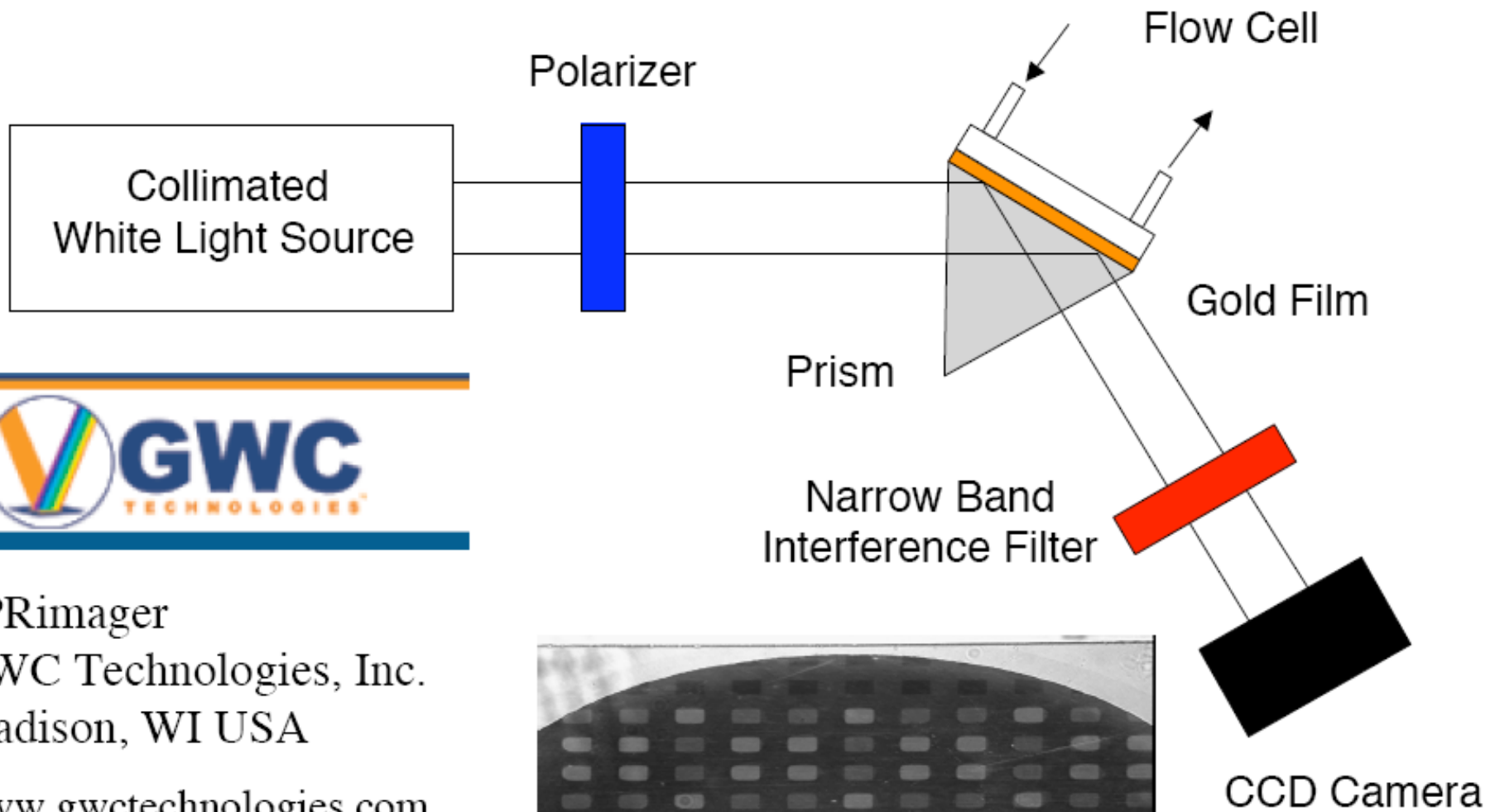
Biomolecular Binding in Real Time

Principle of Detection - SPR (Surface Plasmon Resonance)



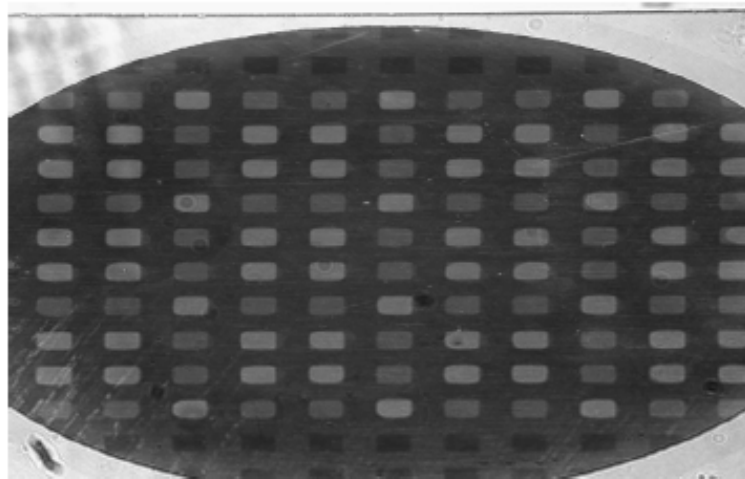


SPR Imaging Apparatus



SPRImager
GWC Technologies, Inc.
Madison, WI USA
www.gwctechnologies.com

Raw Image



Localized Plasmon

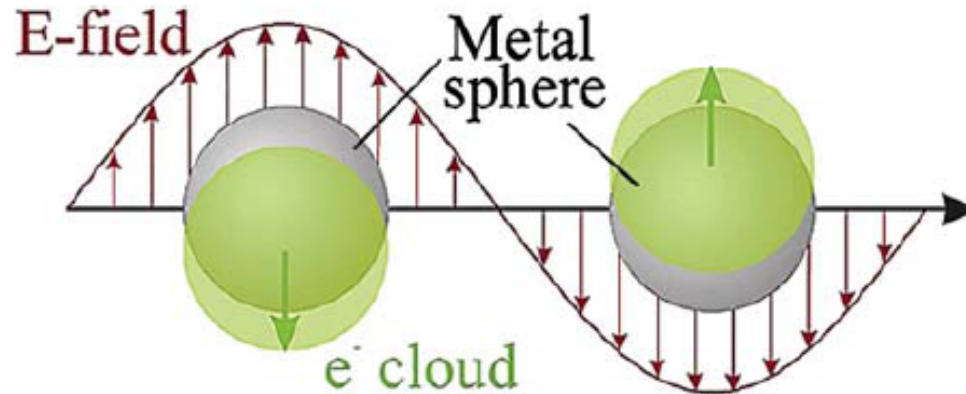
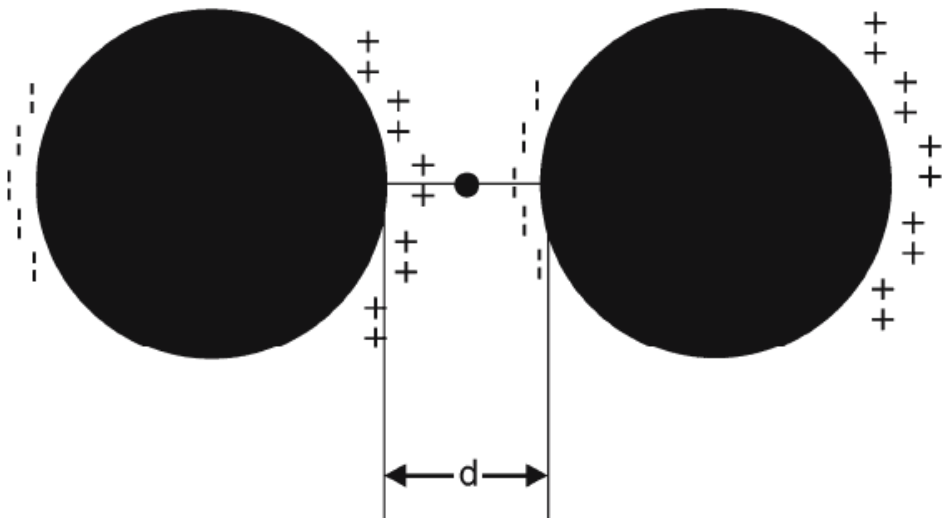
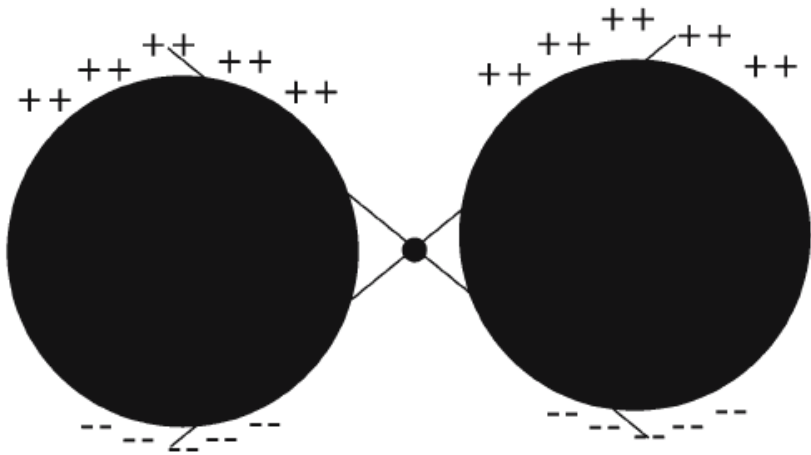


Figure 6. Schematic of plasmon oscillation for a sphere. From [39].



field enhancement

$E_s = gE_0$, where E_0 is the magnitude of the incident field

$$E_R \propto \alpha_R E_s \propto \alpha_R g E_0$$

$$E_{\text{SERS}} \propto \alpha_R g g' E_0$$

$$I_{\text{SERS}} \propto |\alpha_R|^2 |g g'|^2 I_0$$

$$g \cong g'$$

$$|E_L|^4 = |g|^4.$$

Probing Single Molecules and Single Nanoparticles by Surface-Enhanced Raman Scattering

SCIENCE • VOL. 275 • 21 FEBRUARY 1997

Shuming Nie* and Steven R. Emory

Fig. 1. Single Ag nanoparticles imaged with evanescent-wave excitation. Total internal reflection of the laser beam at the glass-liquid interface was used to reduce the laser scattering background. The instrument setup for evanescent-wave microscopy was adapted from Funatsu *et al.* (11). The images were directly recorded on color photographic film (ASA-1600) with a 30-s exposure by a Nikon 35-mm camera attached to the microscope. (A) Unfiltered photograph showing scattered laser light from all particles immobilized on a polylysine-coated surface. (B) Filtered photographs taken from a blank Ag colloid sample (incubated with 1 mM NaCl and no R6G analyte molecules). (C) and (D) Filtered photographs taken from a Ag colloid sample incubated with 2×10^{-11} M R6G. These images were selected to show at least one Raman scattering particle. Different areas of the cover slip were rapidly screened, and most fields of view did not contain visible particles. (E) Filtered photograph taken from Ag colloid incubated with 2×10^{-10} M R6G. (F) Filtered photograph taken from Ag colloid incubated with 2×10^{-9} M R6G. A high-performance bandpass filter was used to remove the scattered laser light and to pass Stokes-shifted Raman signals from 540 to 580 nm (920 to 2200 cm^{-1}). Continuous-wave excitation at 514.5 nm was provided by an Ar ion laser. The total laser power at the sample was 10 mW. Note the color differences between the scattered laser light in (A) and the red-shifted light in (C) through (F).

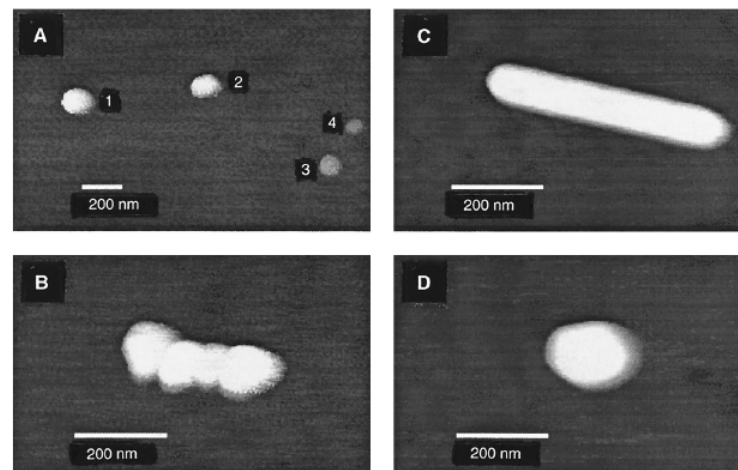
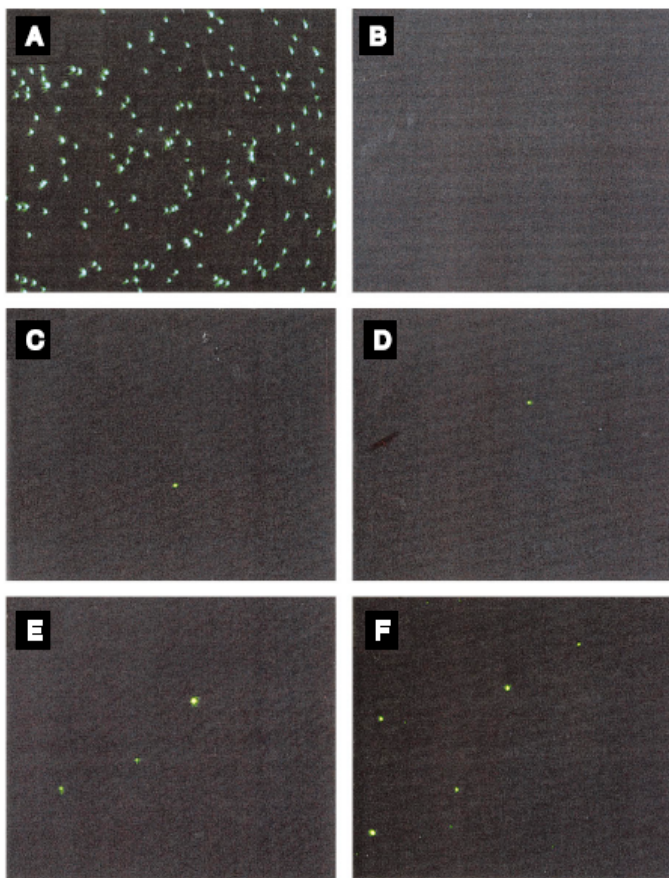
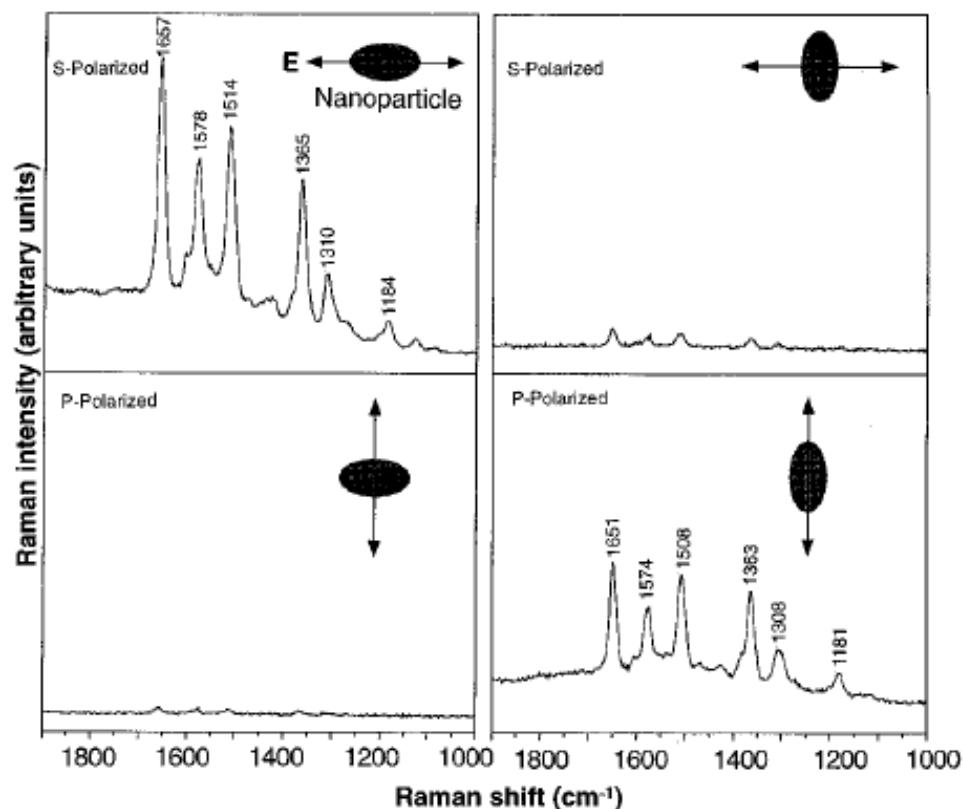


Fig. 2. Tapping-mode AFM images of screened Ag nanoparticles. (A) Large area survey image showing four single nanoparticles. Particles 1 and 2 were highly efficient for Raman enhancement, but particles 3 and 4 (smaller in size) were not. (B) Close-up image of a hot aggregate containing four linearly arranged particles. (C) Close-up image of a rod-shaped hot particle. (D) Close-up image of a faceted hot particle.

rapidly screened, and most fields of view did not contain visible particles. (E) Filtered photograph taken from Ag colloid incubated with 2×10^{-10} M R6G. (F) Filtered photograph taken from Ag colloid incubated with 2×10^{-9} M R6G. A high-performance bandpass filter was used to remove the scattered laser light and to pass Stokes-shifted Raman signals from 540 to 580 nm (920 to 2200 cm^{-1}). Continuous-wave excitation at 514.5 nm was provided by an Ar ion laser. The total laser power at the sample was 10 mW. Note the color differences between the scattered laser light in (A) and the red-shifted light in (C) through (F).

Fig. 3. Surface-enhanced Raman spectra of R6G obtained with a linearly polarized confocal laser beam from two Ag nanoparticles. The R6G concentration was 2×10^{-11} M, corresponding to an average of 0.1 analyte molecule per particle. The direction of laser polarization and the expected particle orientation are shown schematically for each spectrum. Laser wavelength, 514.5 nm; laser power, 250 nW; laser focal radius, ~ 250 nm; integration time, 30 s. All spectra were plotted on the same intensity scale in arbitrary units of the CCD detector readout signal.



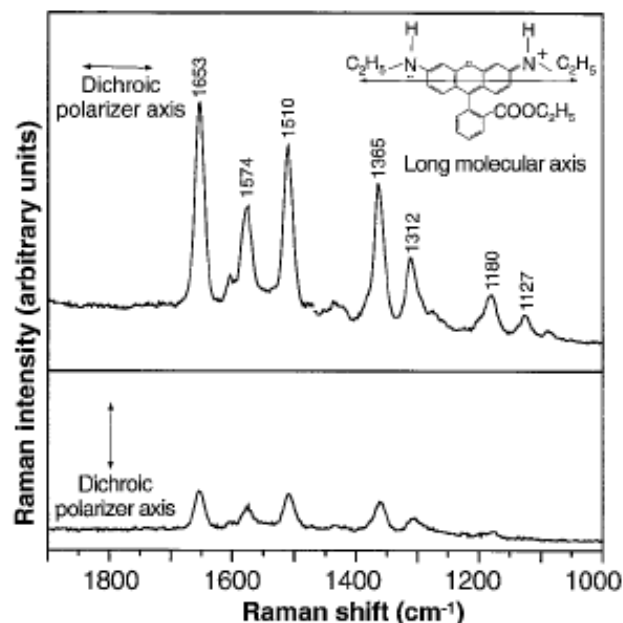
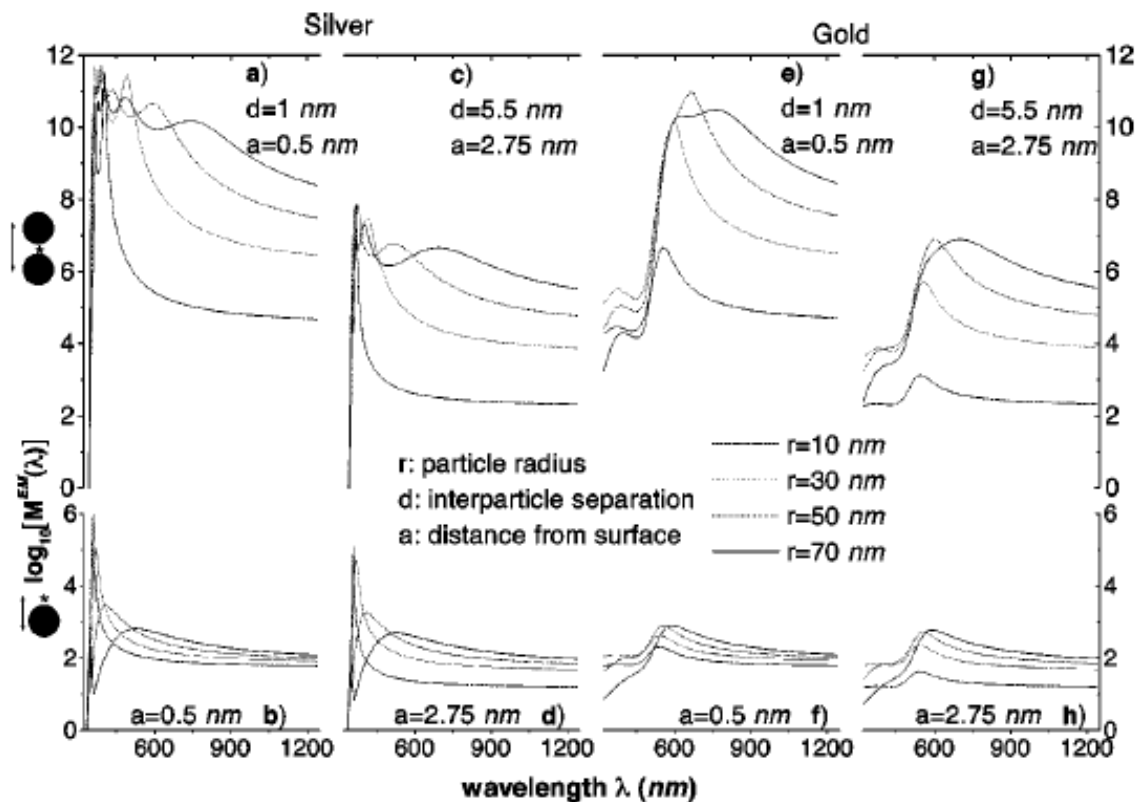


Fig. 4. Emission-polarized surface-enhanced Raman signals of R6G observed from a single Ag nanoparticle with a polarization-scrambled confocal laser beam. A dichroic sheet polarizer was rotated 90° to select Raman scattering signals polarized parallel (upper spectrum) or perpendicular (lower spectrum) to the long molecular axis of R6G. **(Inserts)** Structure of R6G, the electronic transition dipole (along the long axis when excited at 514.5 nm), and the dichroic polarizer orientations. Other conditions as in Fig. 3.

trosopic signatures of adsorbed molecules. For single rhodamine 6G molecules adsorbed on the selected nanoparticles, the intrinsic Raman enhancement factors were on the order of 10^{14} to 10^{15} , much larger than the ensemble-averaged values derived from conventional measurements. This enormous enhancement leads to vibrational Raman signals that are more intense and more stable than single-molecule fluorescence.

Electromagnetic contributions to single-molecule sensitivity in surface-enhanced Raman scattering

PRE 62 4318



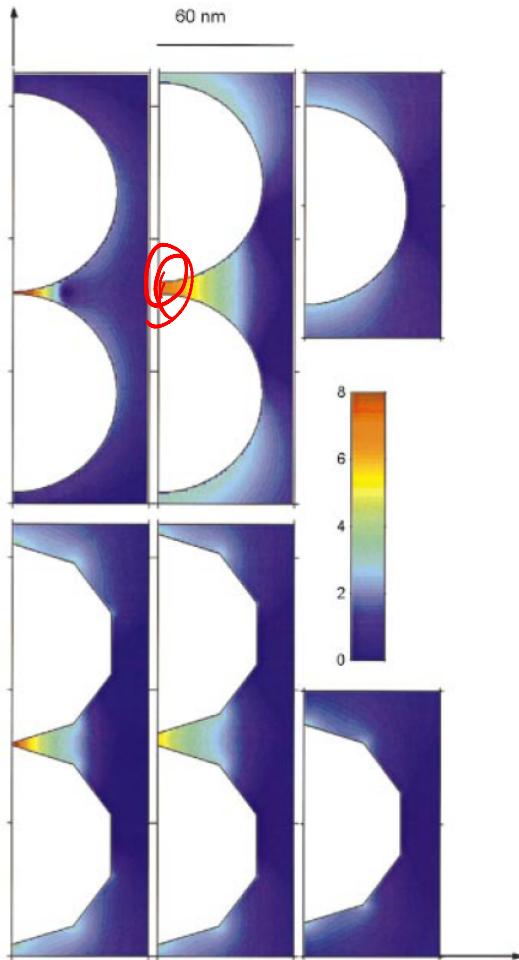


FIG. 3. (Color) EM-enhancement factor M^{EM} at a cross section through six different silver particle configurations. The wavelength of the incident field is $\lambda = 514.5$ nm with vertical polarization. The left-hand column illustrates the EM enhancement for dimer configurations of two spheres (top) and two polygons (bottom) with a separation of 1 nm. The middle column shows the same situation, but with a separation distance of 5.5 nm. The right-hand column shows the case of an isolated single particle. All particles share a common largest dimension of 90 nm. Note that the color scale from dark blue to dark red is logarithmic, covering the interval $10^0 < M^{EM} < 10^8$. Regions with enhancement outside this interval are shown in dark blue and dark red, respectively.

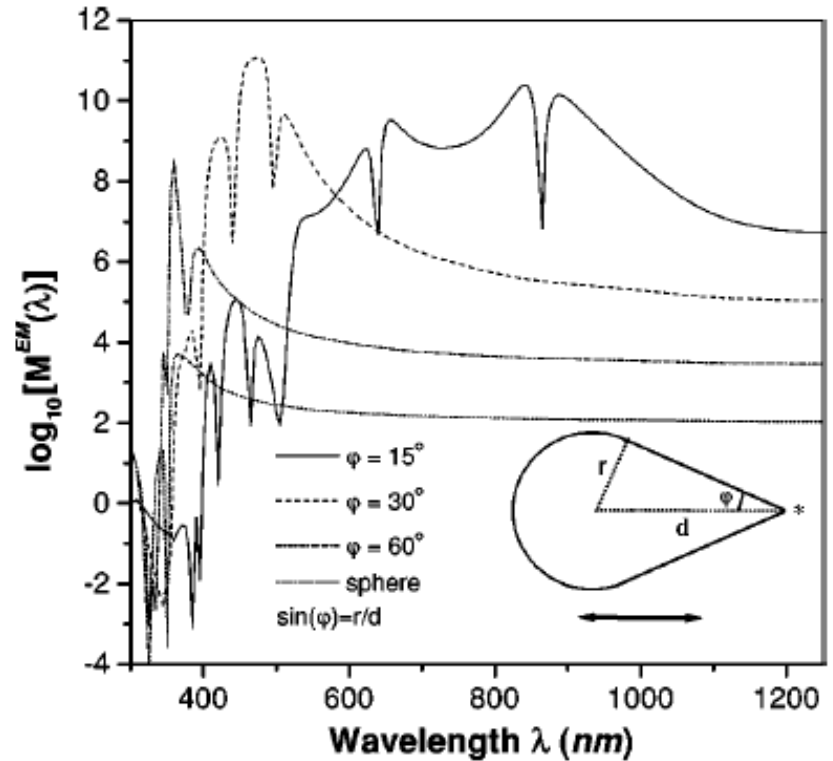


FIG. 5. EM-enhancement factor for a rotationally symmetric silver droplet as a function of the angle defining the opening edge ϕ . The field is polarized parallel to the axis of the droplet and the evaluation position (star) is located 0.5 nm outside the tip. As the droplet becomes sharper the enhancement increases several orders of magnitude.

Nanosphere Arrays with Controlled Sub-10-nm Gaps as Surface-Enhanced Raman Spectroscopy Substrates

J. AM. CHEM. SOC. 2005, 127, 14992–14993

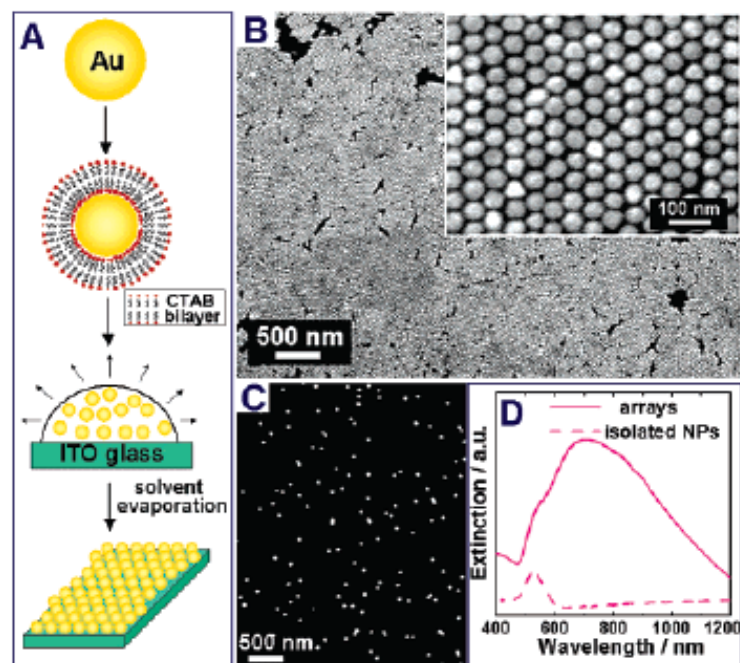


Figure 1. (A) Schematic illustration of the fabrication of sub-10-nm gap Au NP arrays. (B) SEM image of the arrays. (C) SEM image of monolayer of isolated Au NPs on ITO glass. (D) Vis-NIR extinction spectrum of the monolayer of isolated Au NPs and arrays.

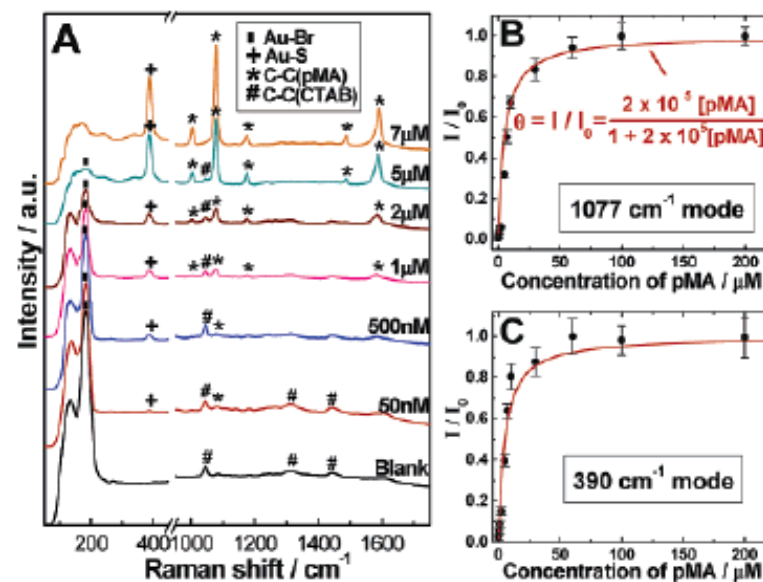
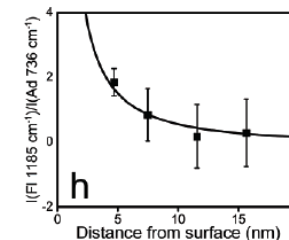
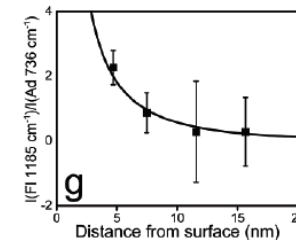
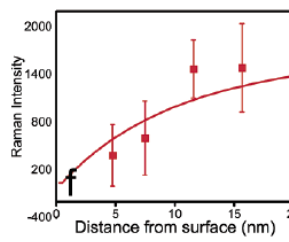
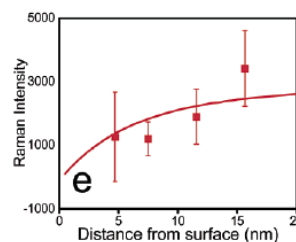
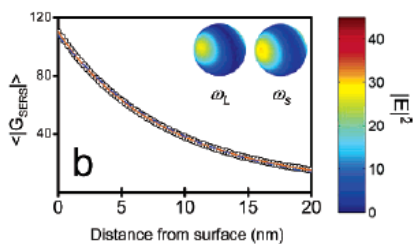
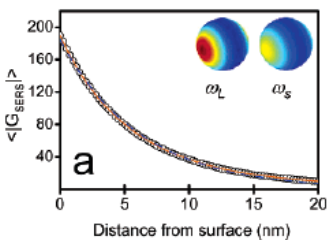
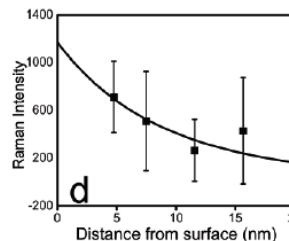
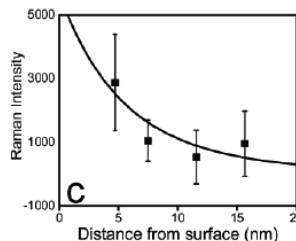
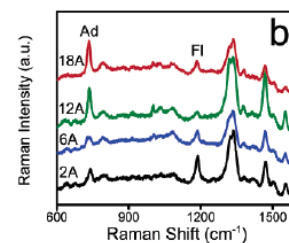
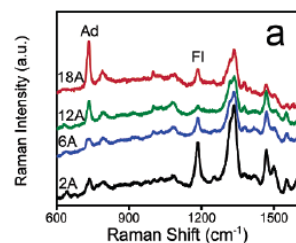
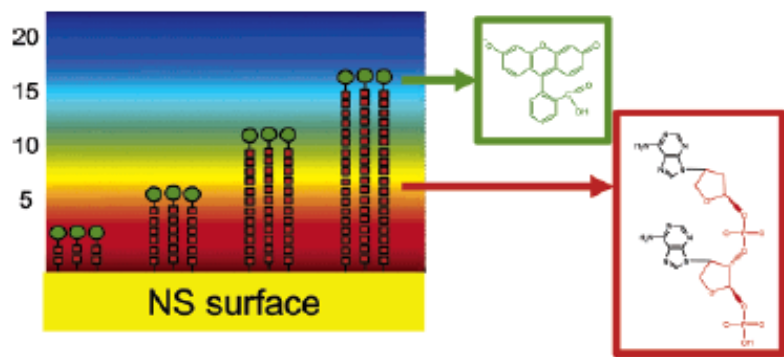


Figure 2. (A) SERS spectra of 5 μL of pMA with different concentrations deposited on the NP arrays. The excitation laser wavelength is 785 nm. Adsorption isotherm of pMA on the NP arrays obtained according to (B) 1077 and (C) 390 cm⁻¹ modes in the SERS spectra. I_0 is the peak intensity of a saturated pMA monolayer.

Profiling the Near Field of a Plasmonic Nanoparticle with Raman-Based Molecular Rulers

NANO
LETTERS

2006
Vol. 6, No. 10
2338–2343



•Eukaryotic cells are about 1000 times larger than bacteria cells and also have a membrane enclosed nucleus containing their DNA, and several other internal structures known as organelles.

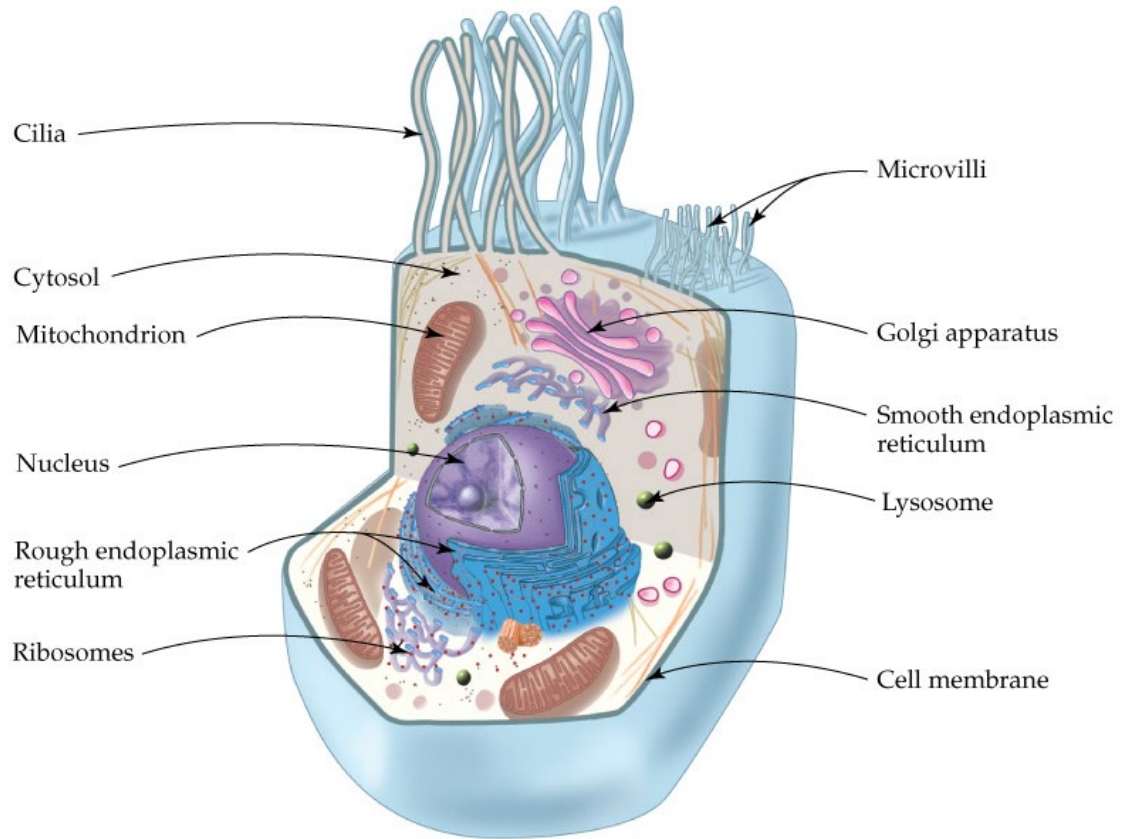
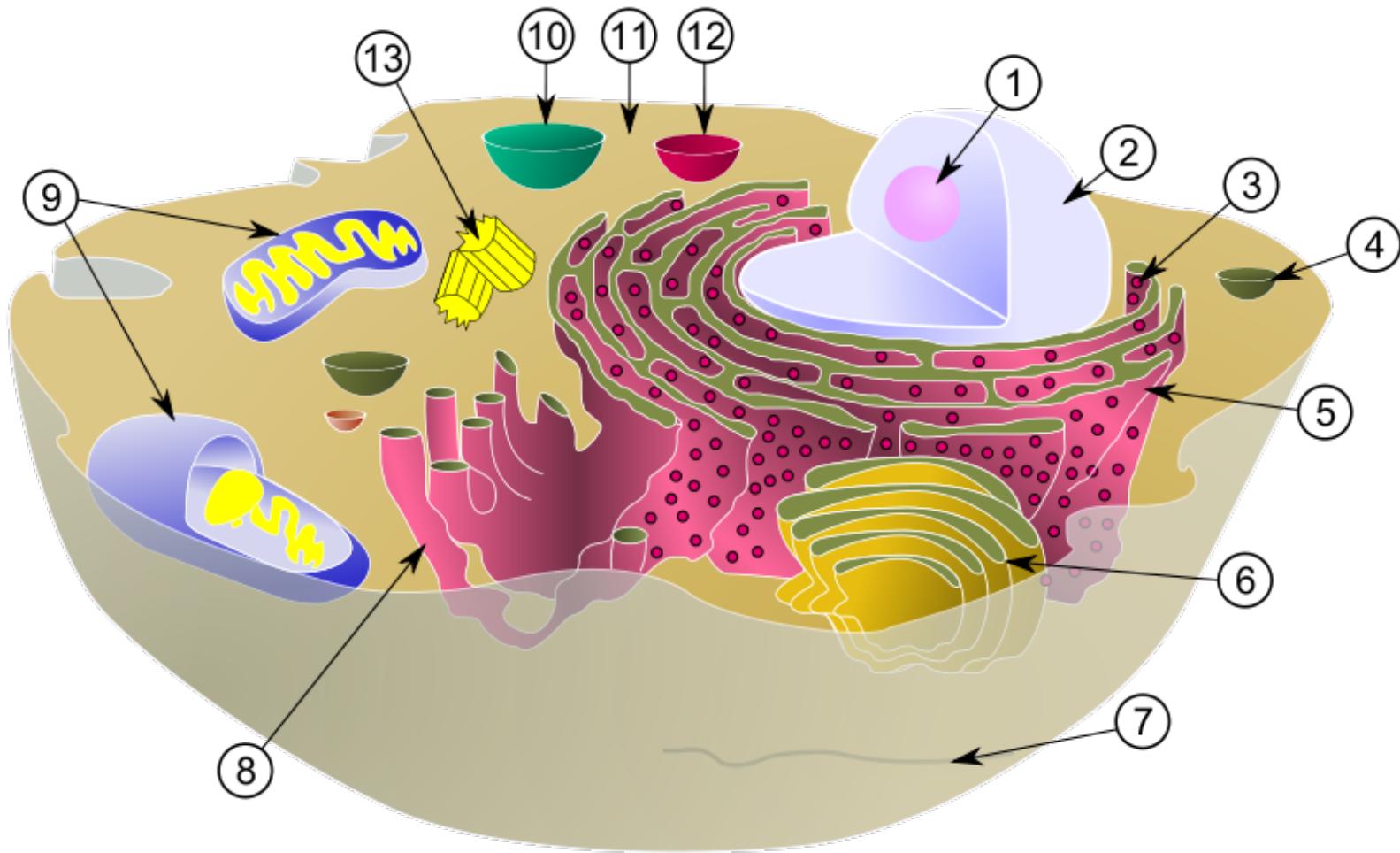


Fig 21.3 A generalized eukaryotic cell.



•Schematic showing the cytoplasm, with its components (or organelles), of a typical animal cell. Organelles: (1) nucleolus (2) nucleus (3) ribosome (4) vesicle (5) rough endoplasmic reticulum (6) Golgi apparatus (7) cytoskeleton (8) smooth endoplasmic reticulum (9) mitochondria (10) vacuole (11) cytosol (12) lysosome (13) centriole.

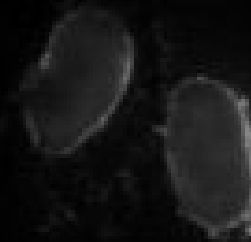
nucleus



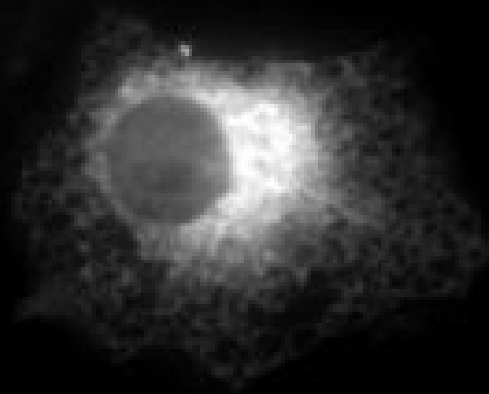
nucleolus



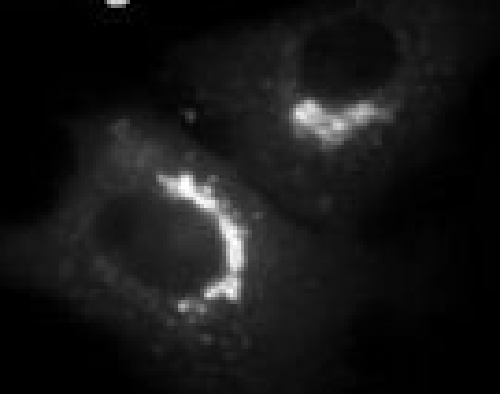
nuclear envelope



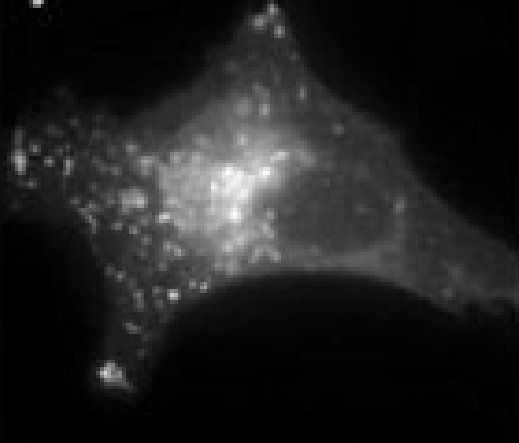
ER



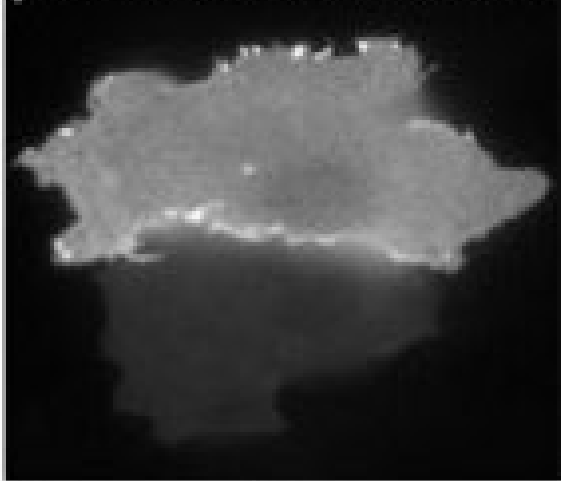
Golgi



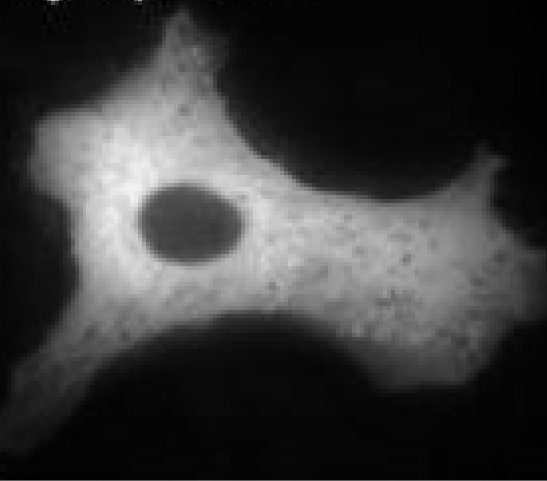
lysosomes



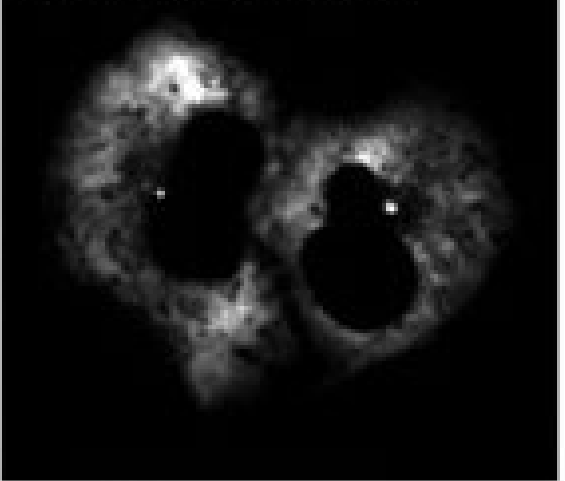
plasma membrane



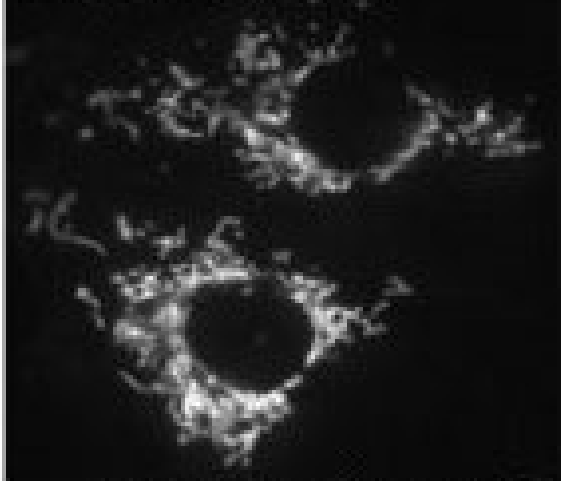
cytoplasm



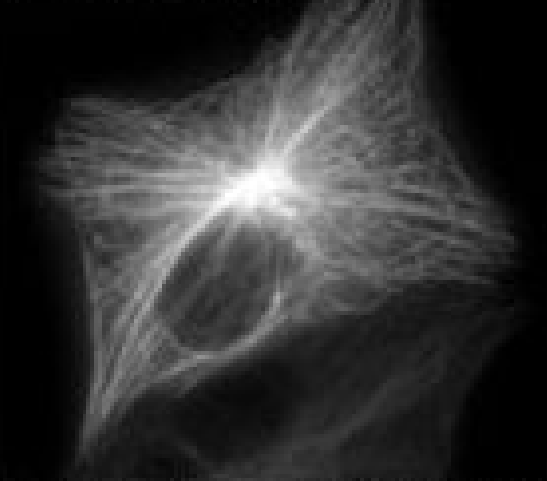
centrosomes



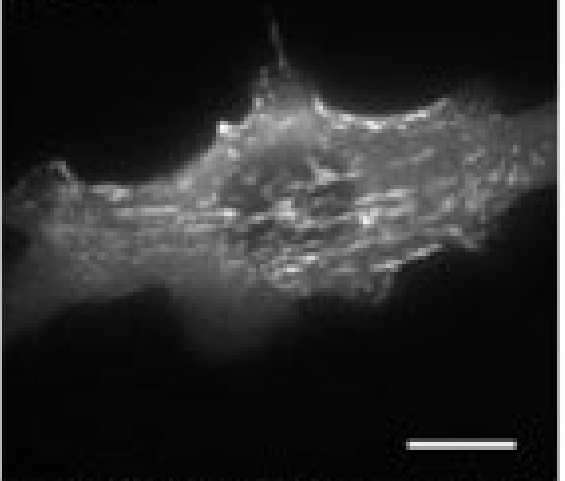
mitochondria



microtubules

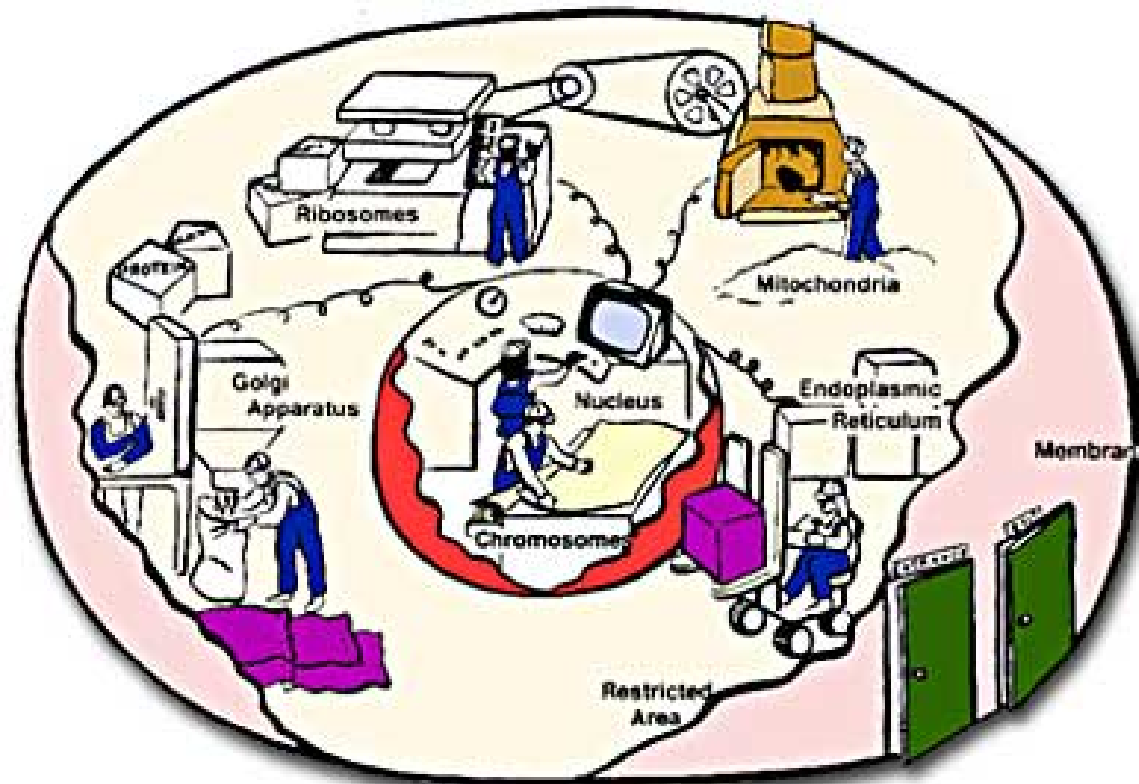


actin



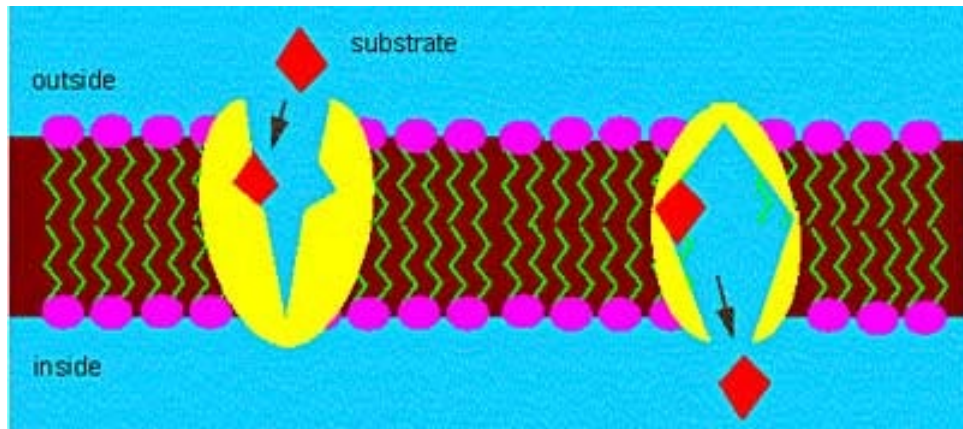
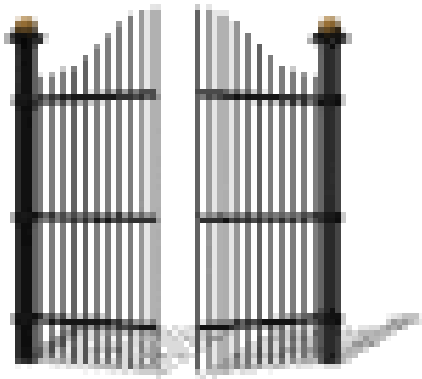
with friendly permission of Jeremy Simons and Rainer Pennerkirk

A Busy Factory

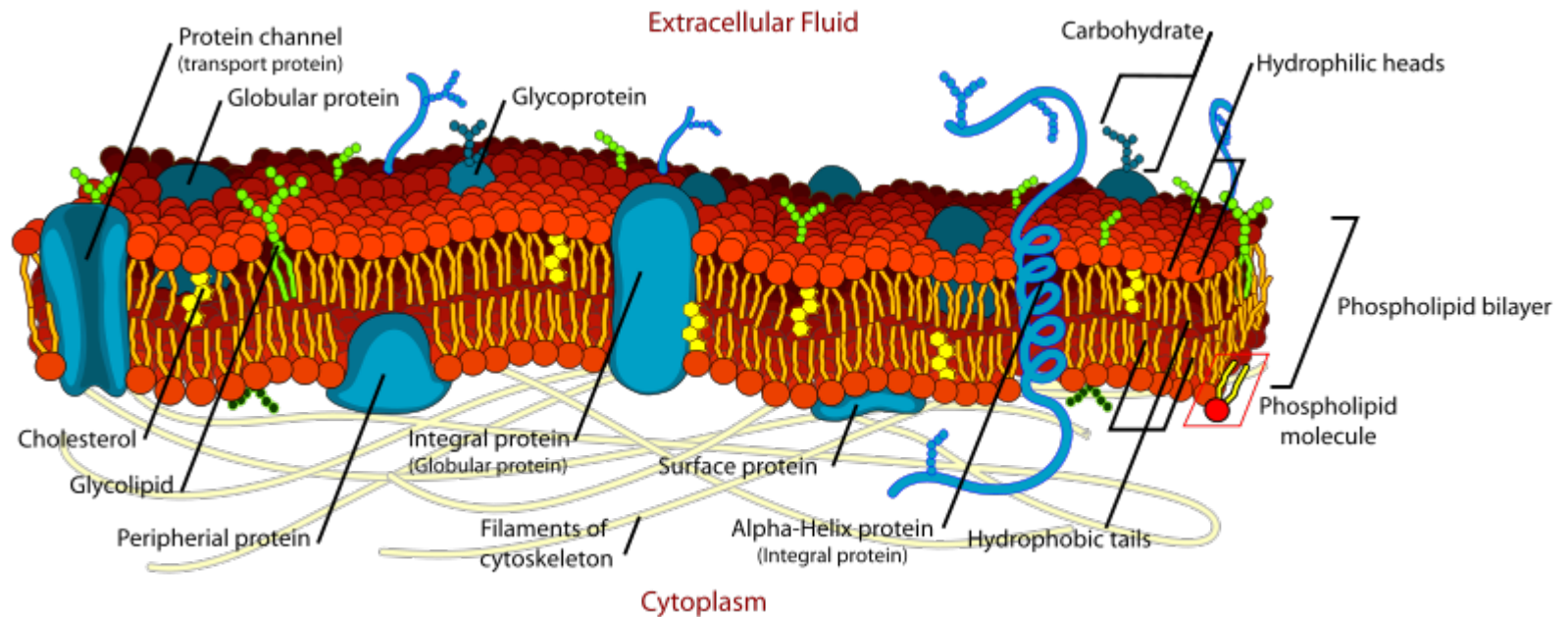


A cell can be thought of as a "factory," with different departments each performing specialized tasks.

The Plasma Membrane



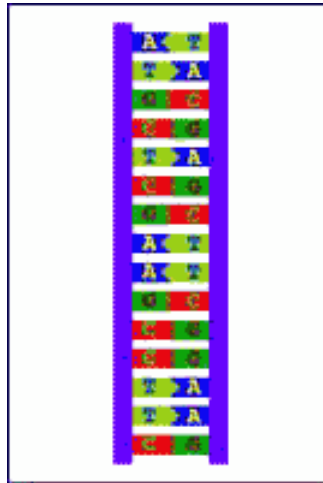
Cell Membrane



Characteristic diffusivities

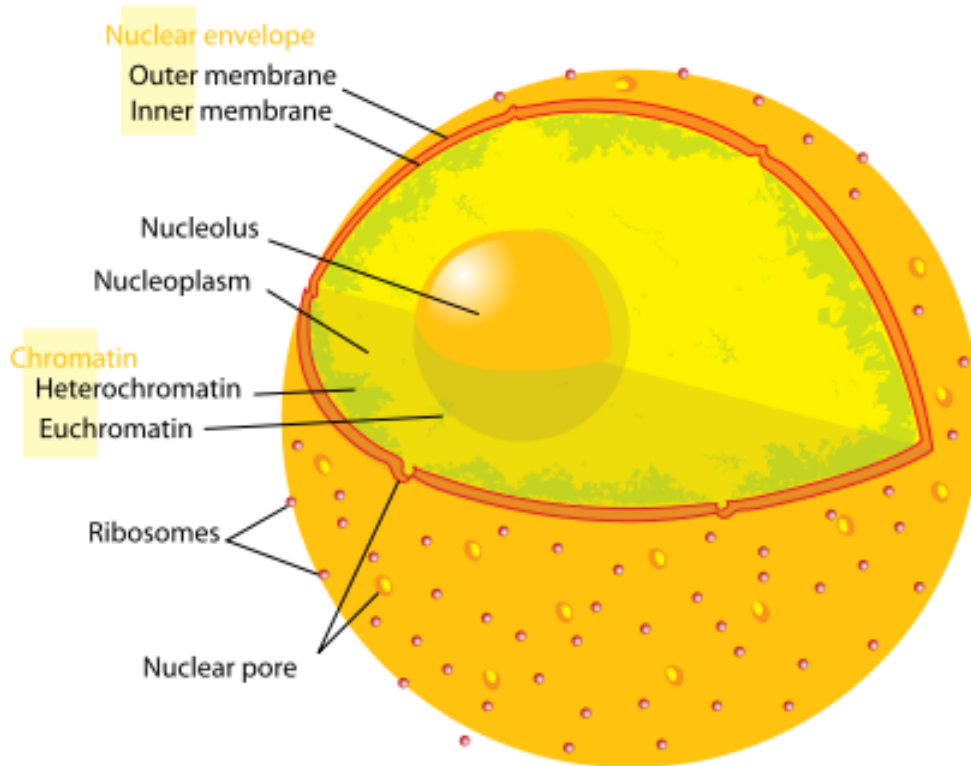
Particle	Typical size	Diffusion constant
Solute ion	10^{-1} nm	$2 \times 10^3 \mu\text{m}^2/\text{s}$
Small protein	5 nm	$40 \mu\text{m}^2/\text{s}$
Virus	100 nm	$2 \mu\text{m}^2/\text{s}$
Bacterium	$1 \mu\text{m}$	$0.2 \mu\text{m}^2/\text{s}$
Mammalian/human cell	$10 \mu\text{m}$	$0.02 \mu\text{m}^2/\text{s}$

The Nucleus



The cell factory contains a large inventory of blueprints dating all the way to its founding. Some of these blueprints are out of date, and some are for parts and products that are no longer made. Part of your job would entail sorting through everything, finding the correct blueprints, copying them, and sending the copies out to the assembly line at the correct time.

Nucleus

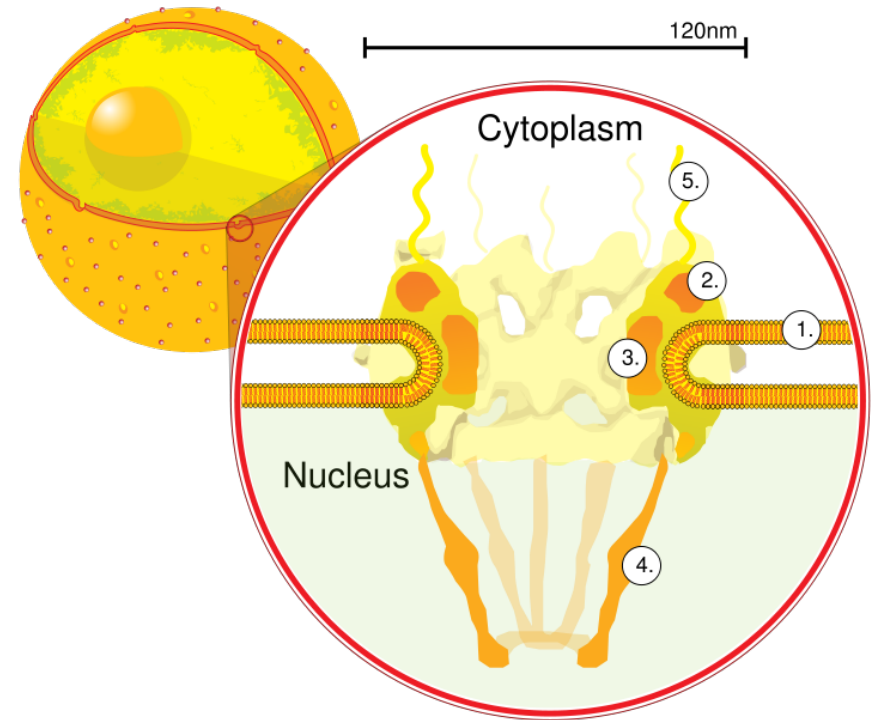


•In cell biology, the **nucleus** is a membrane-enclosed organelle found in most eukaryotic cells. It contains most of the cell's genetic material, organized as multiple long linear DNA molecules in complex with a large variety of proteins such as [histones](#) to form chromosomes. The genes within these chromosomes make up the cell's nuclear genome. The function of the nucleus is to maintain the integrity of these genes and to control the activities of the cell by regulating gene expression.

In cell biology, the **nucleolus** (plural *nucleoli*) is a "sub-organelle" of the cell nucleus, which itself is an organelle. A main function of the nucleolus is the production and assembly of ribosome components

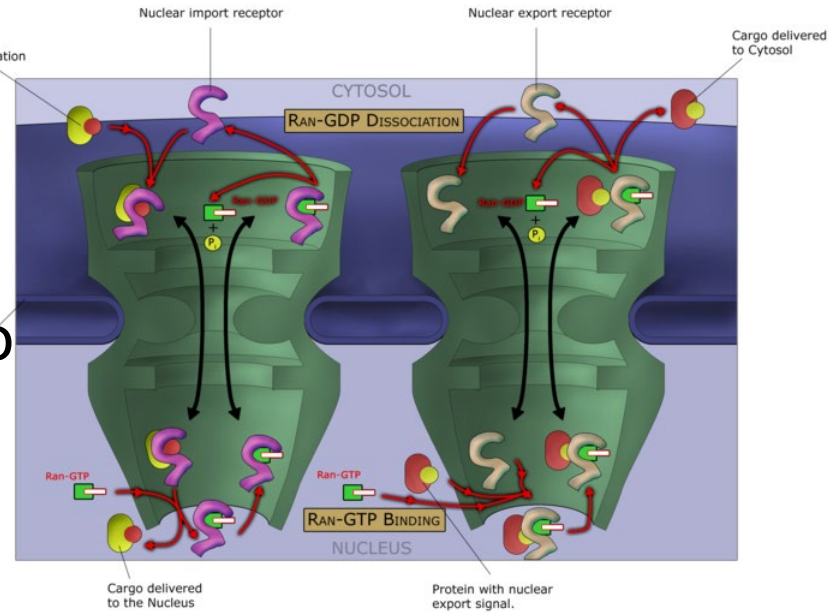
Nuclear pores

Nuclear pores, which provide aqueous channels through the envelope, are composed of multiple proteins, collectively referred to as nucleoporins. The pores are 100 nm in total diameter; however, the gap through which molecules freely diffuse is only about 9 nm wide, due to the presence of regulatory systems within the center of the pore. This size allows the free passage of small water-soluble molecules while preventing larger molecules, such as nucleic acids and proteins, from inappropriately entering or exiting the nucleus. These large molecules must be actively transported into the nucleus instead. The nucleus of a typical mammalian cell will have about 3000 to 4000 pores throughout its envelope

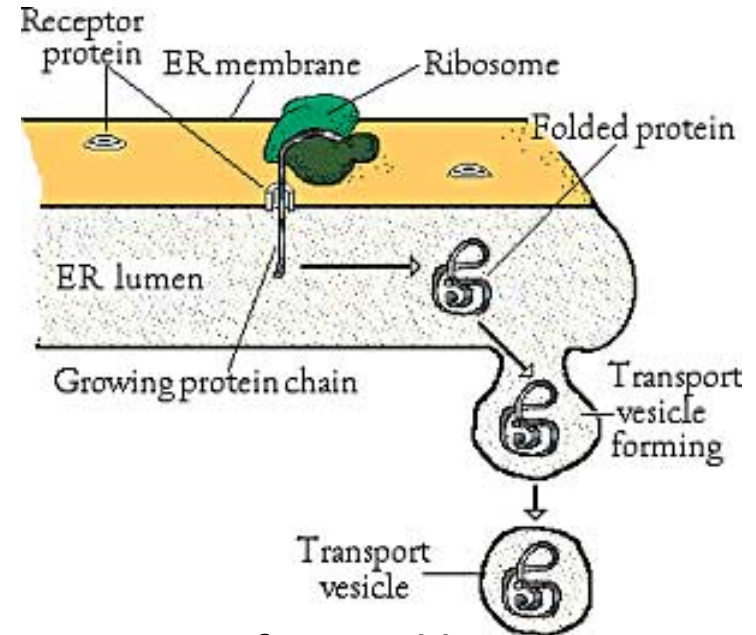
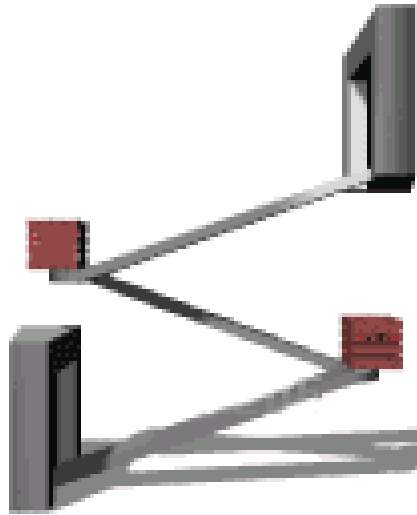


Nuclear localizing sequence (NLS)

- A **nuclear localizing sequence (NLS)** is an amino acid sequence which acts like a 'tag' on the exposed surface of a protein. This sequence is used to confine the protein to the cell nucleus through the **Nuclear Pore Complex** and to direct a newly synthesized protein into the nucleus via its recognition by cytosolic nuclear transport receptors. Typically, this signal consists of a few short sequences of positively charged lysines or arginines. Typically the NLS will have a sequence (NH₂)-Pro-Pro-Lys-Lys-Lys-Arg-Lys-Val-(COOH).



The Ribosomes and the ER

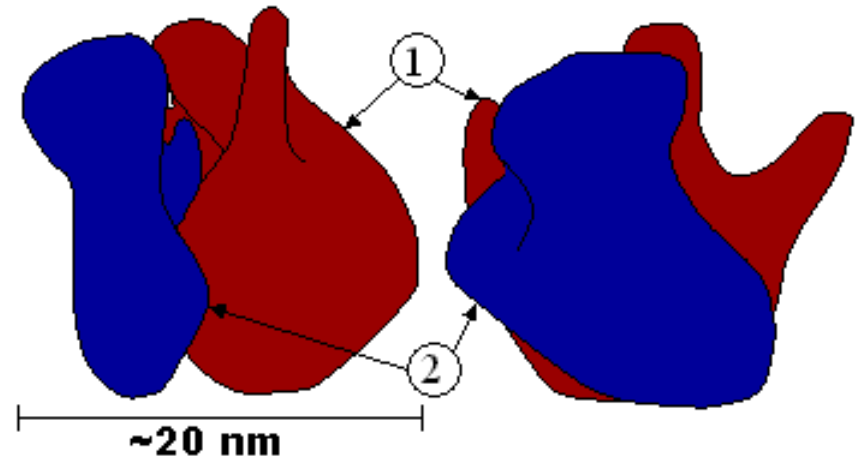


Ribosomes, the workers that build proteins, are manufactured by the nucleolus. They consist of two separate subunits: a large, lower subunit and a small, upper subunit. Ribosomes attach to the rough ER. Now let's take a look at how final processing occurs

The cell has its own assembly line and workers. Within the cytoplasm is a series of large, flattened membranes that fold back and forth on each other and have a very large surface area. This collection of membranes is called the **ENDOPLASMIC RETICULUM**, or **ER**.

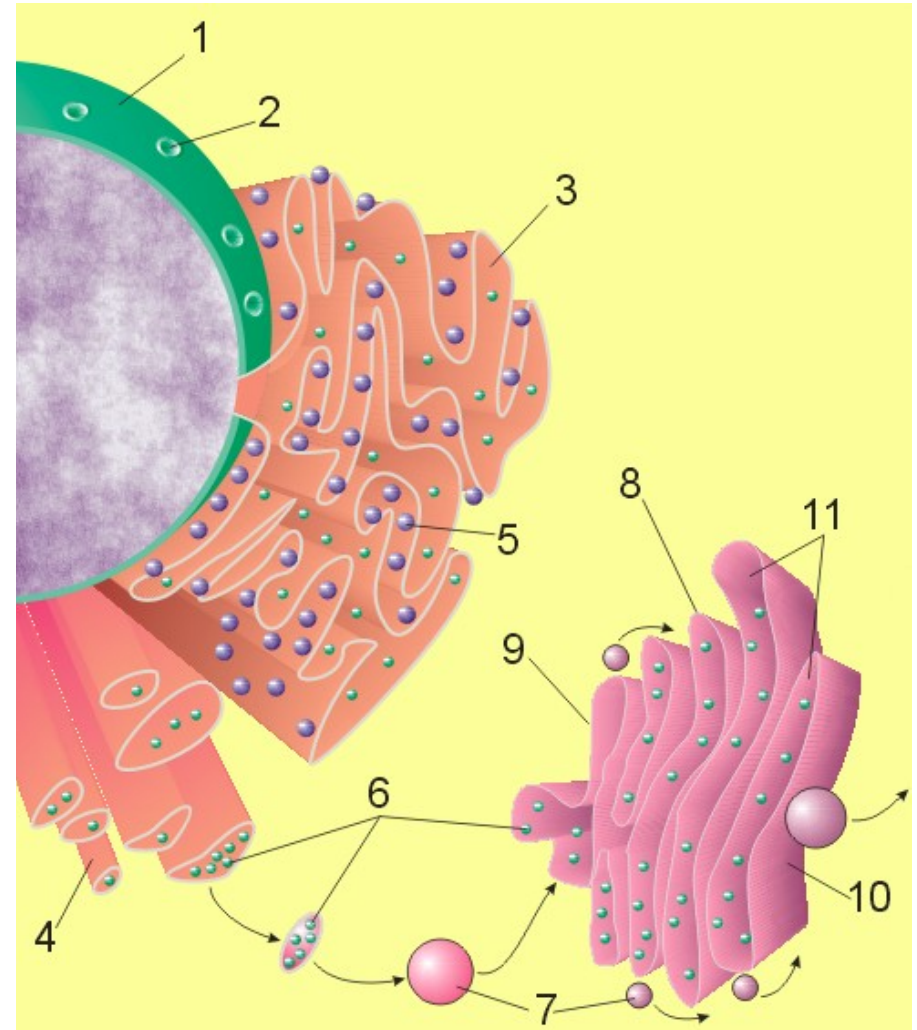
Ribosome

A **ribosome** is a small, dense organelle in cells that assembles proteins. Ribosomes are about 20nm in diameter and are composed of 65% ribosomal RNA and 35% ribosomal proteins (known as a [Ribonucleoprotein](#) or RNP). It translates messenger RNA (mRNA) to build a polypeptide chain (e.g., a protein) using amino acids delivered by Transfer RNA (tRNA). It can be thought of as a giant enzyme that builds a protein from a set of genetic instructions. Ribosomes can float freely in the cytoplasm (the internal fluid of the cell) or bound to the endoplasmic reticulum, or to the nuclear envelope.



Endoplasmic Reticulum

The **endoplasmic reticulum** or **ER** is an organelle found in all eukaryotic cells that is an interconnected network of tubules, vesicles and cisternae that is responsible for several specialized functions: Protein translation, folding, and transport of proteins to be used in the cell membrane (e.g., transmembrane receptors and other integral membrane proteins), or to be secreted (exocytosed) from the cell (e.g., digestive enzymes); sequestration of calcium; and production and storage of glycogen, steroids, and other macromolecules.^[1] The endoplasmic reticulum is part of the endomembrane system. The basic structure and composition of the ER membrane is similar to the plasma membrane.



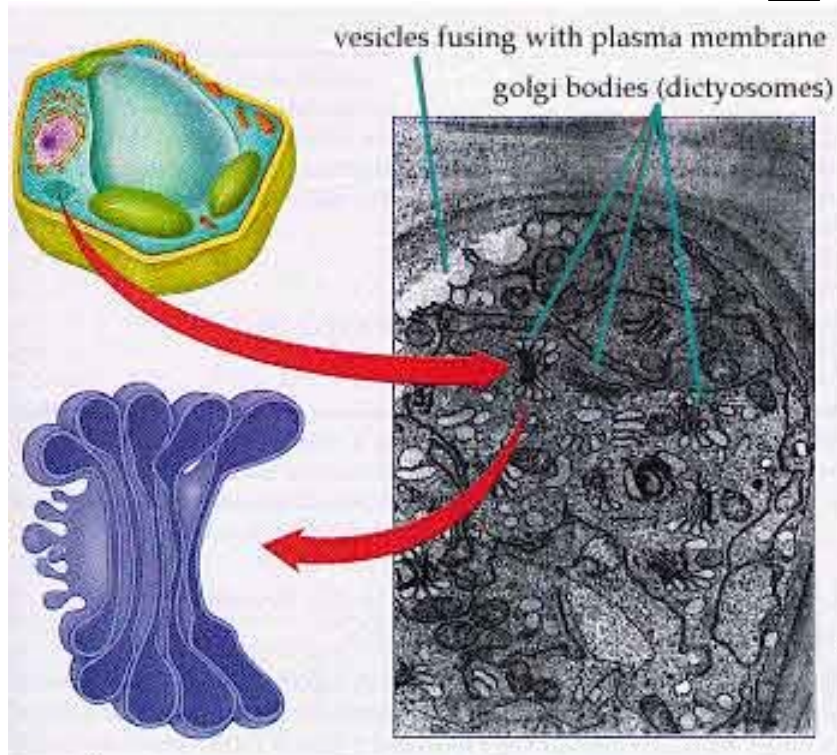
Rough endoplasmic reticulum

- The surface of the rough endoplasmic reticulum is studded with protein-manufacturing [ribosomes](#) giving it a "rough" appearance. But it should be noted that these ribosomes are not resident of the endoplasmic reticulum incessantly. The ribosomes only bind to the ER once it begins to synthesize a protein destined for sorting. The membrane of the rough endoplasmic reticulum is continuous with the outer layer of the nuclear envelope. Although there is no continuous membrane between the rough ER and the Golgi apparatus, membrane bound vesicles shuttle proteins between these two compartments. The rough endoplasmic reticulum works in concert with the Golgi complex to target new proteins to their proper destinations


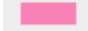




Smooth endoplasmic reticulum

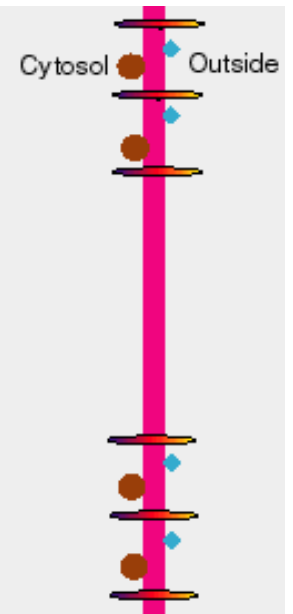
- The smooth endoplasmic reticulum has functions in several metabolic processes, including synthesis of lipids, metabolism of carbohydrates and calcium concentration, and attachment of receptors on cell membrane proteins. It is connected to the nuclear envelope. Smooth endoplasmic reticulum is found in a variety of cell types (both animal and plant) and it serves different functions in each. It consists of tubules and vesicles that branch forming a network. In some cells there are dilated areas like the sacs of rough endoplasmic reticulum. The network of smooth endoplasmic reticulum allows increased surface area for the action or storage of key enzymes and the products of these enzymes. The smooth endoplasmic reticulum is known for its storage of calcium ions in muscle cells.

The Golgi Apparatus



This animation illustrates how secretion vesicles, arising from the Golgi, fuse with the PM and dump the contents of their lumen outside of the cell. Note that the membrane of the SV turns insideout and becomes new PM.

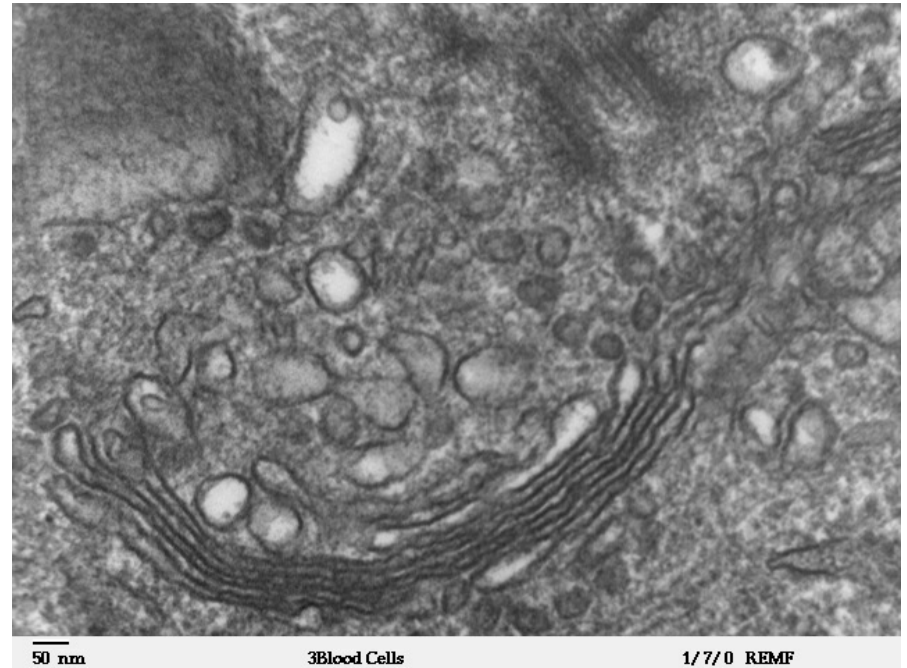
-  Lipid Bilayer (SV)
-  Lipid Bilayer (PM)
-  Transmembrane Protein
-  Peripheral Protein (inside)
-  Peripheral Protein (outside)
-  Soluble Proteins



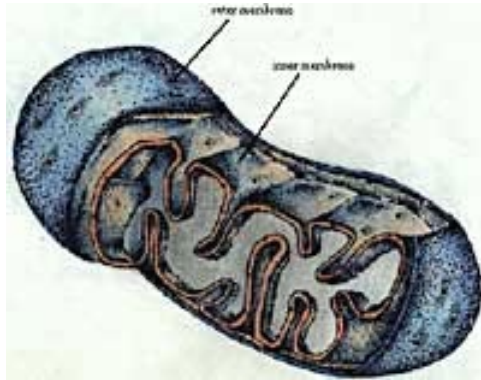
The Golgi apparatus is analogous to the finishing and packing room in a factory. Once the ribosome finishes manufacturing a protein in the rough ER, the protein needs to be prepared for use or export. Special enzymes will trim off any extra amino acids, and then the unfinished protein moves through channels in the smooth ER.

Golgi apparatus

The **Golgi apparatus** (also called the **Golgi body**, **Golgi complex**, or **dictyosome**) is an organelle found in typical eukaryotic cells. It was identified in 1898 by the Italian physician Camillo Golgi and was named after him. The primary function of the Golgi apparatus is to process and package macromolecules synthesised by the cell, primarily proteins and lipids. The Golgi apparatus forms a part of the endomembrane system present in eukaryotic cells.



Mitochondria

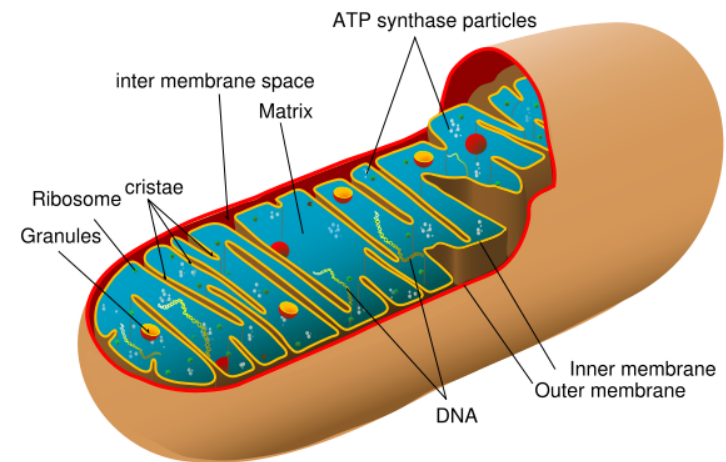


***- ATP -
a Source of
ENERGY***

Like our factory's power plant, mitochondria and chloroplasts transform one form of energy to another. Remember that nearly all the energy used by living things on Earth comes from the Sun. This section discusses how energy is made available for cell processes.

Mitochondrion

- In cell biology, a **mitochondrion** is a membrane-enclosed organelle, found in most eukaryotic cells. Mitochondria are sometimes described as "cellular power plants," because they convert NADH and NADPH into energy in the form of ATP via the process of oxidative phosphorylation. A typical eukaryotic cell contains about 2,000 mitochondria, which occupy roughly one fifth of its total volume. Mitochondria contain DNA that is independent of the DNA located in the cell nucleus. According to the endosymbiotic theory, mitochondria are descended from free-living prokaryotes.



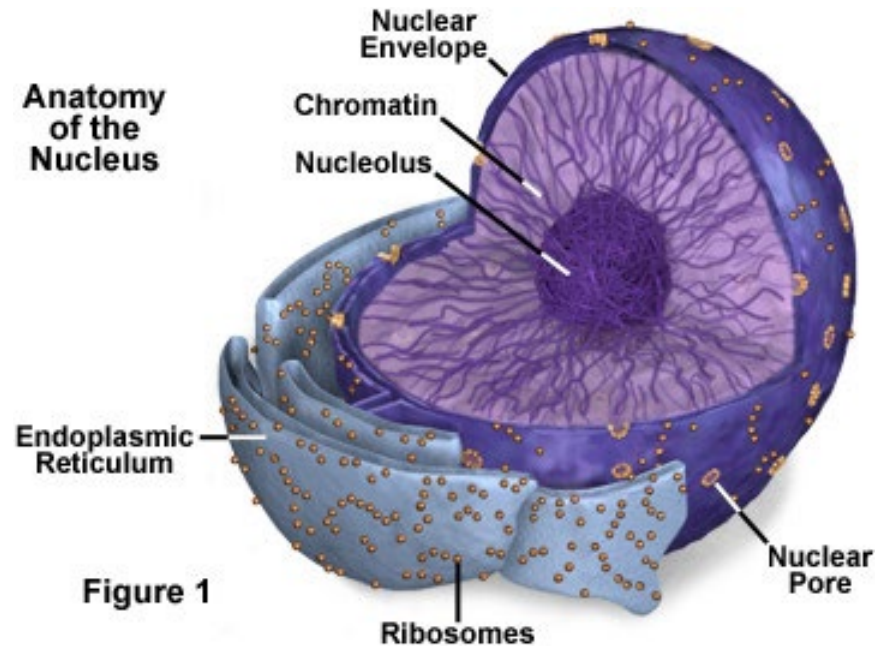
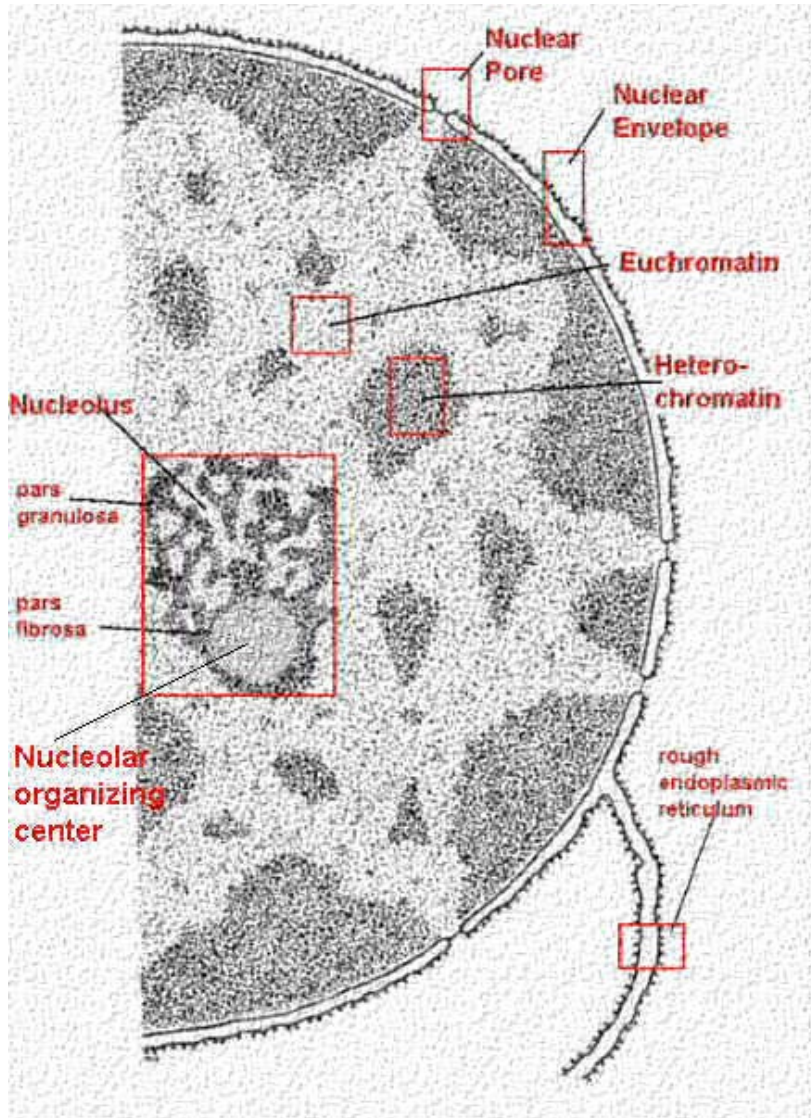


Figure 1

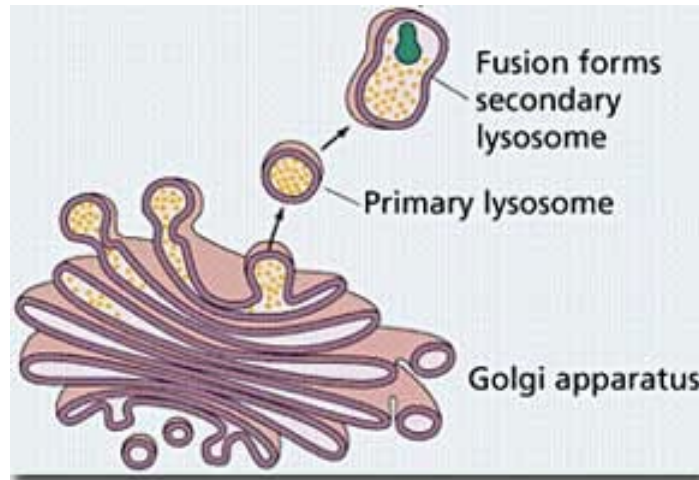
The main roles of the nucleolus are to synthesize rRNA and assemble ribosomes

The main function of the cell nucleus is to control gene expression and mediate the replication of DNA during the cell cycle

Lysosomes

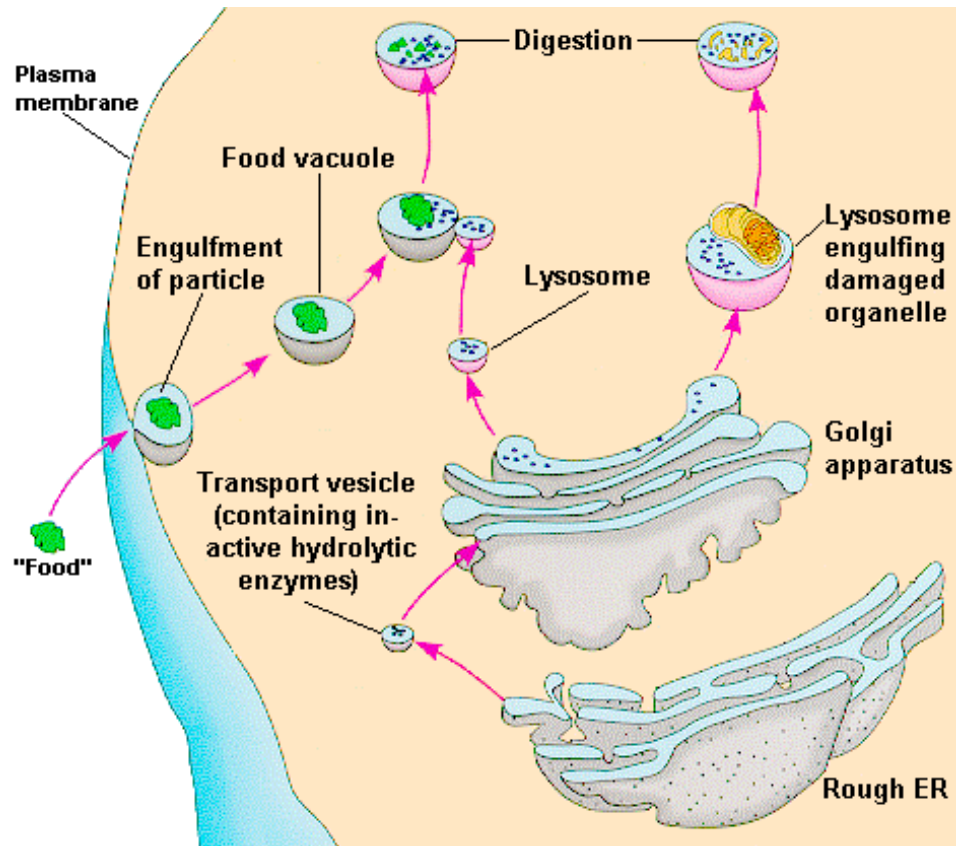
- **Lysosomes** are organelles that contain digestive enzymes (acid [hydrolases](#)). They digest excess or worn out organelles, food particles, and engulfed viruses or bacteria. The membrane surrounding a lysosome prevents the digestive enzymes inside from destroying the cell. Lysosomes fuse with vacuoles and dispense their enzymes into the vacuoles, digesting their contents. They are built in the Golgi apparatus. The name *lysosome* derives from the [Greek](#) words *lysis*, which means dissolution or destruction, and *soma*, which means body. They are frequently nicknamed "suicide-bags" or "suicide-sacs" by cell biologists due to their role in autolysis.

Lysosomes



Lysosomes are responsible for the breakdown and absorption of materials taken in by the cell. Often, a cell engulfs a foreign substance through **ENDOCYTOSIS**, another form of active transport. During endocytosis, the cell membrane puckers up, forms a pouch around materials outside the cell, and pinches off to become a vesicle. If the contents need to be destroyed, lysosomes combine with the vesicle and release their enzymes.

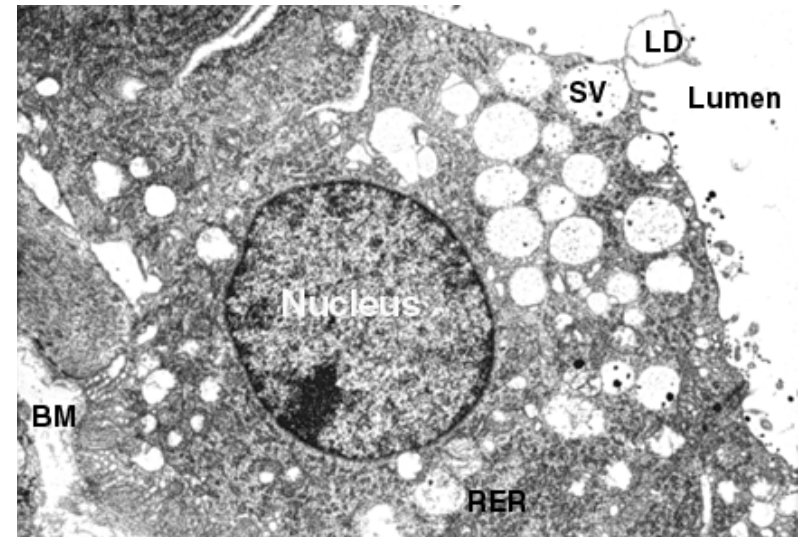
Lysosome



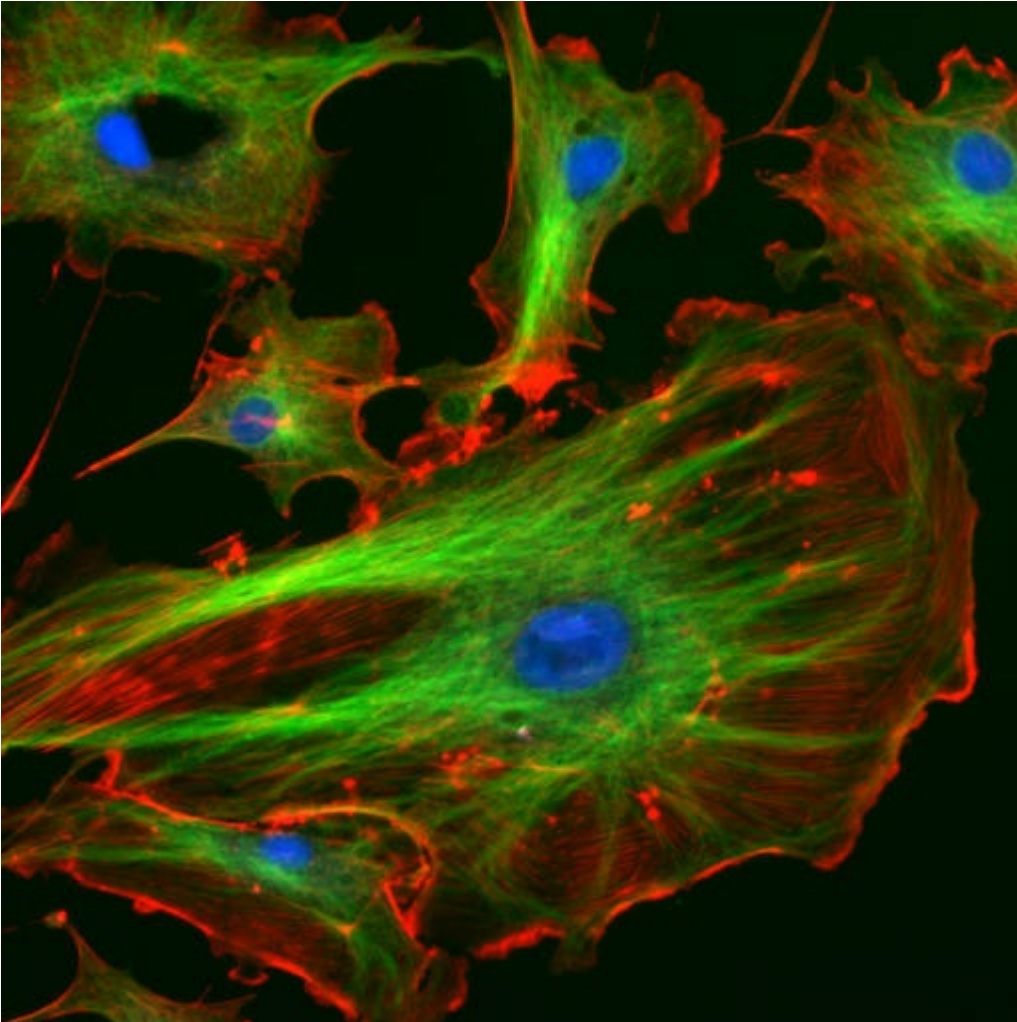
Vesicle

In cell biology, a **vesicle** is a relatively small and enclosed compartment, separated from the **cytosol** by at least one lipid bilayer. If there is only one lipid bilayer, they are called *unilamellar* vesicles; otherwise they are called *multilamellar*. Vesicles store, transport, or digest cellular products and waste.

This biomembrane enclosing the vesicle is similar to that of the plasma membrane. Because it is separated from the cytosol, the intravesicular environment can be made to be different from the cytosolic environment. Vesicles are a basic tool of the cell for organizing metabolism, transport, enzyme storage, as well as being chemical reaction chambers. Many vesicles are made in the Golgi apparatus, but also in the endoplasmic reticulum, or are made from parts of the plasma membrane.

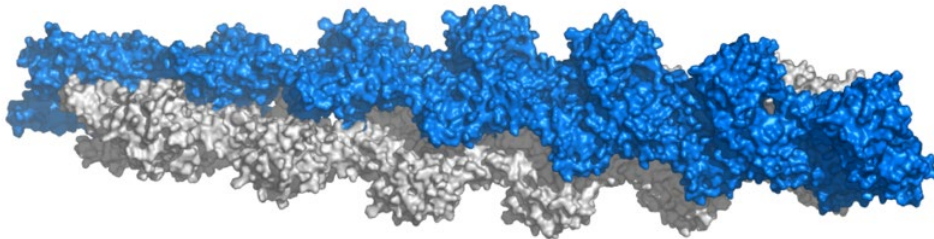


Cytoskeleton



The eukaryotic cytoskeleton. Actin filaments are shown in red, microtubules in green, and the nuclei are in blue.

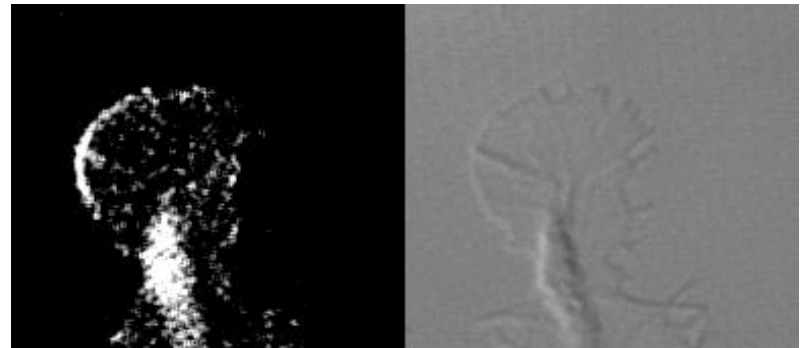
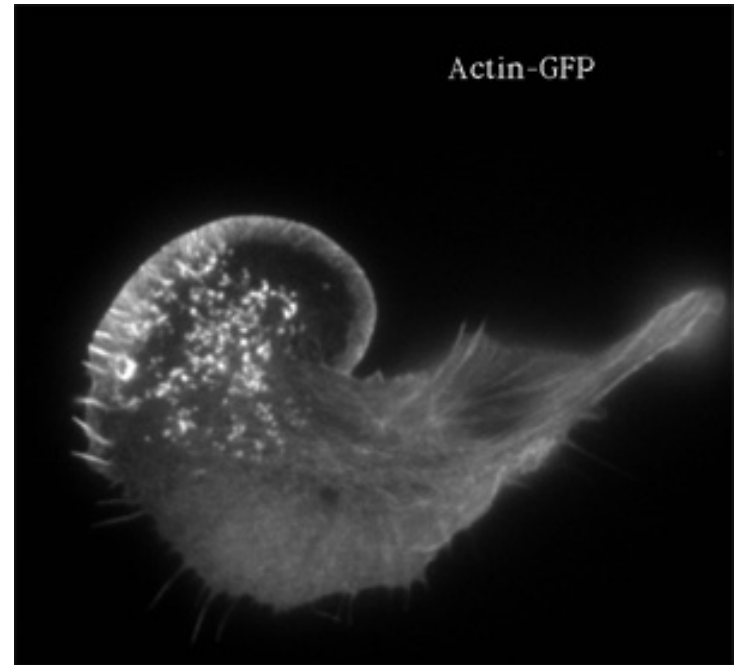
Actin



- **Actin** is a globular structural, 42 kDa, [protein](#) that polymerizes in a helical fashion to form **actin filaments** (or **microfilaments**). These form the cytoskeleton, a three-dimensional network inside the eukaryotic cell. Actin filaments provide mechanical support for the cell, determine its shape, and enable movement of the cell through [lamellipodia](#), [filopodia](#), or [pseudopodia](#). Actin filaments, along with myosin, have an essential role in muscular contraction. In the [cytosol](#), actin is predominantly bound to ATP, but can also bind to ADP. An ATP-actin complex polymerizes faster and dissociates slower than an ADP-actin complex.

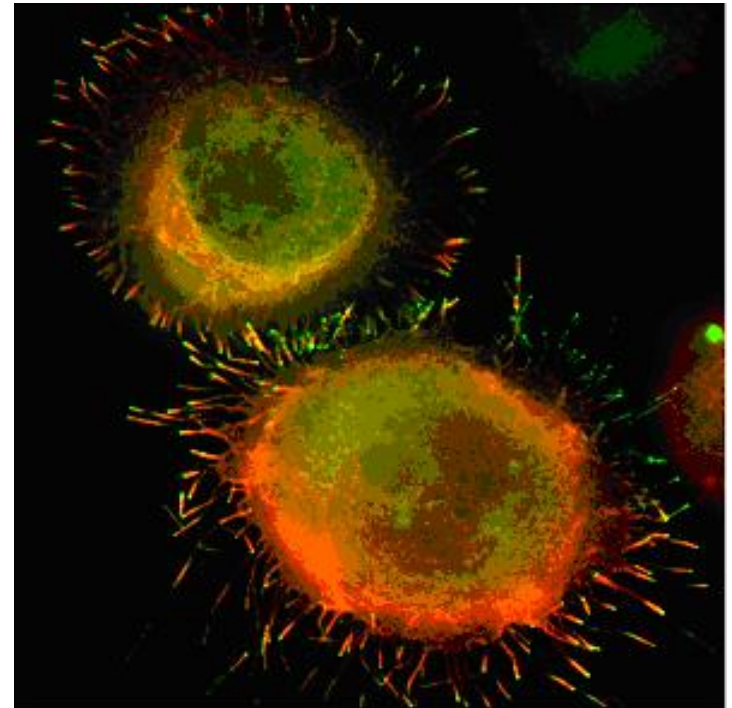
Lamellipodia

- The **lamellipodium** is a cytoskeletal actin projection on the mobile edge of the cell. It contains a two-dimensional actin mesh; the whole structure pulls the cell across a substrate. Within the lamellipodia are ribs of actin called microspikes, which, when they spread beyond the lamellipodium frontier, are called filopodia (Small, et al, 2002). The lamellipodium is born of actin nucleation in the plasma membrane of the cell (Alberts, et al, 2002) and is the primary area of actin incorporation or microfilament formation of the cell. Lamellipodia range from $1\mu\text{m}$ to $5\mu\text{m}$ in breadth and are approximately $0.2\mu\text{m}$ thick. Lamellipodia are found primarily in very mobile cells, crawling at a speeds of $10\text{-}20\mu\text{m}/\text{minute}$ over epithelial surfaces..
- The tip of the lamellipodium is the site where exocytosis occurs in migrating mammalian cells as part of their clathrin-mediated endocytic cycle.



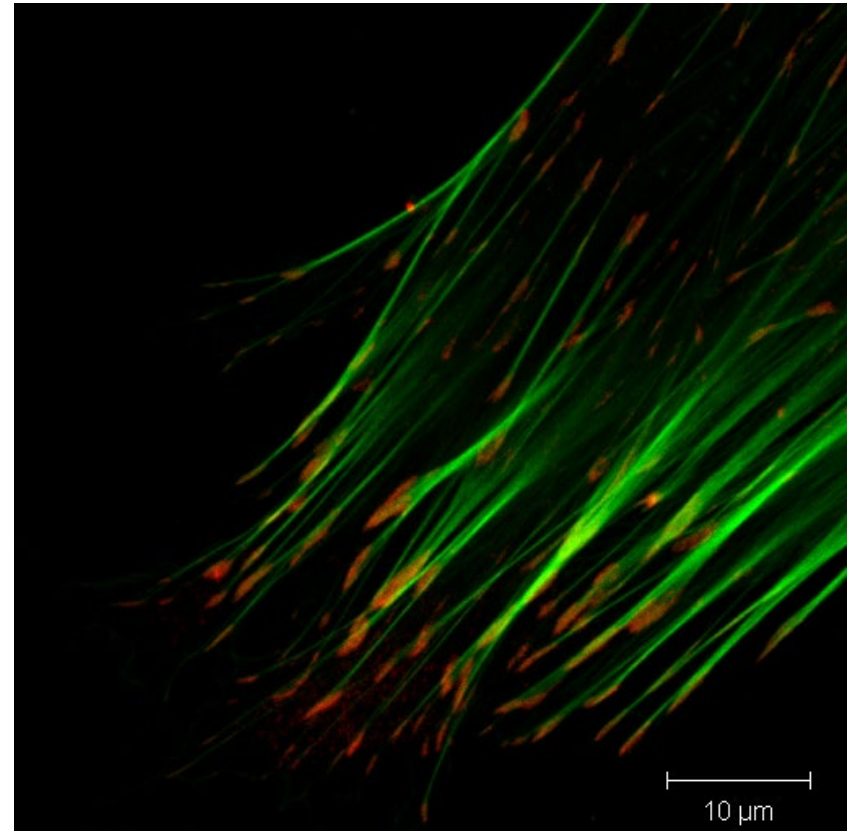
Filopodia

The **filopodia** are slender cytoplasmic projections, similar to [lamellipodia](#), which extend from the leading edge of migrating cells. They contain actin filaments cross-linked into bundles by actin-binding proteins, e.g. fimbrin. Filopodia form focal adhesions with the substratum, linking it to the cell surface. A cell migrates along a surface by extending filopodia at the leading edge. The filopodia attach to the substratum further down the migratory pathway, then contraction of stress fibres retracts the rear of the cell to move the cell forwards.



Focal adhesion

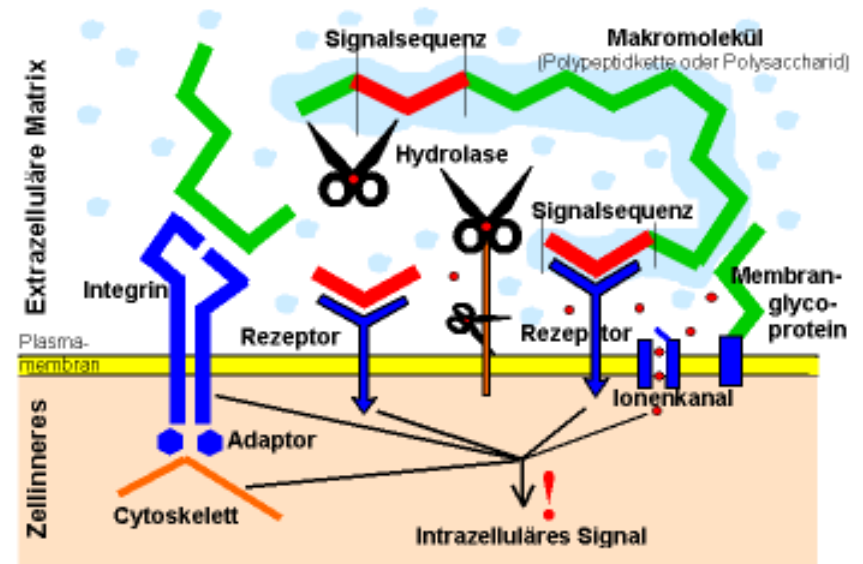
- In cell biology, '**Focal Adhesions**' are specific types of large macromolecular assemblies through which both mechanical force and regulatory signals are transmitted. More precisely, **FAs** can be considered as sub-cellular macromolecules that mediate the regulatory effects (e.g. cell anchorage) of extracellular matrix (ECM) adhesion on cell behavior.



Extra Cellular Matrix

The ECM's main components are various [glycoproteins](#), [proteoglycans](#) and [hyaluronic acid](#). In most animals, the most abundant glycoproteins in the ECM are collagens.

ECM also contains many other components: proteins such as fibrin, [elastin](#), [fibronectins](#), [laminins](#), and [nidogens](#), and minerals such as [hydroxylapatite](#), or fluids such as blood plasma or serum with secreted free flowing [antigens](#).

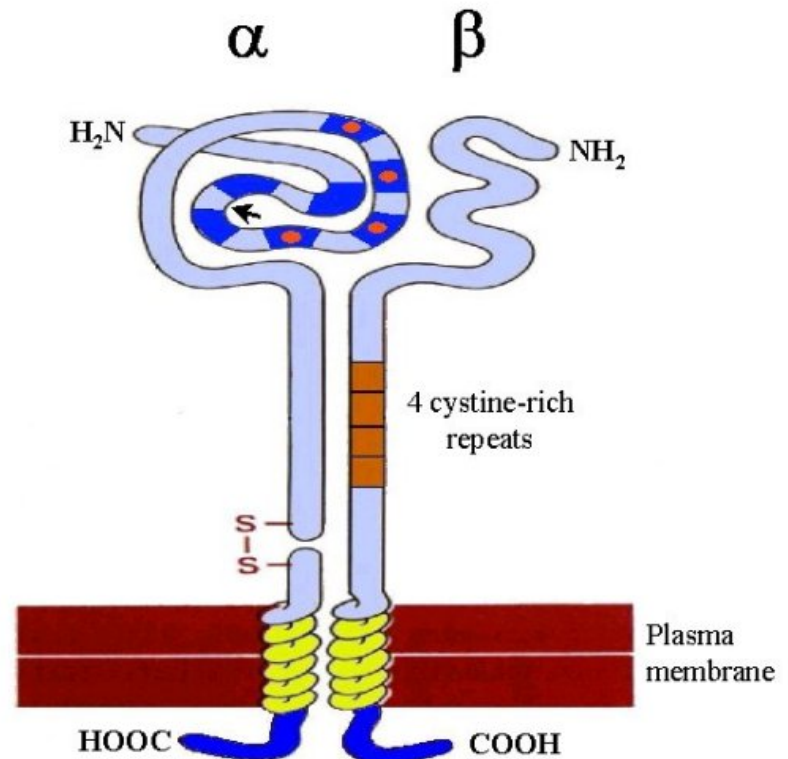


Integrin

An **integrin**, or **integrin receptor**, is an integral membrane protein in the plasma membrane of cells. It plays a role in the attachment of a cell to the [extracellular matrix](#) (ECM) and to other cells, and in signal transduction from the ECM to the cell. There are many types of integrin, and many cells have multiple types on their surface. Integrins are of vital importance to all [metazoans](#), from humans to sponges.

Schematic drawing of a typical integrin dimer

Arrow shows the region where an I domain is inserted in some α subunits. Not all α subunits are posttranslationally cleaved. Internal disulphide bonds within subunits are not shown. Dark blue regions in the head segment of the α subunit represent homologous repeats. Those with the EF-hand consensus sequence are marked with red circles to denote binding sites for divalent metal ion.



Endocytosis

